NASA
TP
2128
c.1

NASA
Technical
Paper
2128

December 1983

Flight Test of the Glide-Slope Track and Flare-Control Laws for an Automatic Landing System for a Powered-Lift STOL Airplane

DeLamar M. Watson,
Gordon H. Hardy, and
David N. Warner, Jr.

LOAN COPY: RETURN TO
AFWL TECHNICAL LIBRARY
KIRTLAND AFB, N.M. 87117

NASA

25th Anniversary
1958-1983

TECH LIBRARY KAFB, NM
0134985

NASA
Technical
Paper
2128

1983

Flight Test of the Glide-Slope Track and Flare-Control Laws for an Automatic Landing System for a Powered-Lift STOL Airplane

DeLamar M. Watson,
Gordon H. Hardy, and
David N. Warner, Jr.

Ames Research Center
Moffett Field, California

NASA
National Aeronautics
and Space Administration

**Scientific and Technical
Information Branch**

1983

TABLE OF CONTENTS

Page

SUMMARY 1

INTRODUCTION 1

CURRENT AUTOLAND PRACTICE 2
- Glide-Slope Tracking Performance 2
- Autoland Touchdown Limits 2

EXPERIMENTAL EQUIPMENT AND SYSTEMS 3
- Flight-Test Facility 4
- Navigation System 5

GLIDE-SLOPE TRACK AND FLARE-CONTROL LAWS 6
- Controls 6
- Operation on the Backside of the Power Curve 7
- Control-Law Configurations 7
- Predict Terms 7
- Complementary Filters 9
- Pitch Inner Loop 10
- Nozzle Inner Loop 12
- Autothrottle-Choke Inner Loop 13
- Glide-Slope Track 15
- Speed Control 16
- Flare 16
- Three-Control and Two-Control Systems 18

FLIGHT-TEST RESULTS 18
- Wind Conditions 20
- Glide-Slope Track Performance 21
- Statistical Flare-Entry Conditions 38
- Flare Performance 42
- Statistical Flare Summaries 50

CONCLUDING REMARKS 59

APPENDIX A – OPERATING LIMITS AND NOMINAL SPEED, RPM, AND NOZZLE SETTINGS 64

APPENDIX B – CLOSED-LOOP ENGINE-TRANSFER FUNCTION 66

APPENDIX C – DERIVATION OF THE GLIDE-SLOPE CAPTURE CONTROL LAW 67

APPENDIX D – MEASURED WIND DATA 69

APPENDIX E – STATISTICAL SUMMARIES OF GLIDE-SLOPE TRACK FLIGHT DATA 74

REFERENCES 84

SUMMARY

An automatic landing system was developed for the Augmentor Wing Jet STOL Research Airplane to establish the feasibility and examine the operating characteristics of a powered-lift STOL transport flying a steep, microwave-landing system (MLS) glide slope to automatically land on a STOL port. The flight test results in this report address the longitudinal aspects of automatic powered-lift STOL airplane operation including glide-slope tracking on the backside of the power curve, flare, and touchdown. Three different autoland control laws were evaluated to demonstrate the tradeoff between control complexity and the resulting performance. The flight test and simulation methodology used in developing conventional jet-transport systems was applied to the powered-lift STOL airplane. The results obtained from this research program suggest that an automatic landing system for a powered-lift STOL airplane operating into an MLS-equipped STOL port is feasible. However, the airplane must be provided with a means of rapidly regulating lift to satisfactorily provide the glide-slope tracking and control of touchdown sink rate needed for automatic landings.

INTRODUCTION

In recent years, the short takeoff and landing (STOL) airplane has been under development for use as an element in a high-speed transportation system capable of linking metropolitan centers, major hub airports, and outlying communities. The aircraft manufacturers, the airlines, and the FAA have indicated considerable interest in the application of STOL technology to short-haul transportation systems. American Airlines and McDonnell Douglas reports, references 1 and 2, describe the planning and results of the flight evaluation of the Breguet 941S four-engine turboprop, deflected-slipstream STOL transport operating on a short-haul route structure. The FAA developed a STOL port planning guide (ref. 3), and STOL airplane certification requirements (refs. 4 and 5). The FAA conducted a flight evaluation of a light wing-loading STOL airplane, a de Havilland DHC-6 Twin Otter, operated into a simulated, ground-level STOL runway (ref. 6). The Canadian Department of Transportation (DOT) undertook an extensive evaluation of the use of specially equipped de Havilland DHC-6 Twin Otter airplanes, operating along an off-airways, area-navigation-route structure between Ottawa and Montreal, to establish the feasibility and the techniques for short-haul transport operations (ref. 7). Commuter airlines in the United States have begun using area navigation routes between the less conjested, short runway segments at major airports (ref. 8). The transports listed above are all propeller-driven STOL airplanes with relatively light wing loading and low cruise speeds.

Another type of STOL airplane, is the powered-lift STOL category, which has been developed in several different forms in the past decade. Powered-lift STOL airplanes are capable of jet-transport cruise speeds and of making steep, slow approaches to short runways. The YC-15 used the externally blown flap concept; exhaust flow from underwing podded engines passes through the flap system to provide high lift. The YC-14 and the Quiet Short-Haul Research Airplane (QSRA) (ref. 9), employ the upper-surface blowing concept; exhaust from engines mounted above the wing passes over large flaps to provide high-lift coefficients. The Augmentor Wing concept uses engine fan air that is ducted through a bisurface flap system to obtain high lift and drag coefficients. Powered-lift aircraft may have an extra control which either directly regulates the vector direction of the exhaust thrust or influences the downwash angle of the wing airflow. This extra control can be useful for establishing flightpath trim conditions and can, in some cases, be used effectively for speed control.

Powered-lift aircraft have several unusual operating characteristics. Typically, powered-lift STOL aircraft approach at speeds that cause them to operate on the backside of the power curve with the thrust vector nearly perpendicular to the flightpath. Because of the high wing loading and low airspeeds, the aircraft glidepath tracking response to changes in pitch attitude can be sluggish. These characteristics generally make thrust the most effective path controller and the elevator the most effective speed controller. Powered-lift STOL aircraft generally fly steep approach angles from 6° to 7.5° for terrain avoidance or noise abatement. Although these approach paths are twice as steep as are flown by conventional takeoff and landing (CTOL) transports, the approach speed of the STOL airplane is roughly half of the CTOL transport approach speed. The net result is that the vertical speeds experienced by STOL and CTOL aircraft are approximately equal. Wind-disturbance effects may be different for STOL airplanes than for CTOL airplanes. A

30-knot gust, which is only 23% of the 130-knot approach speed of a CTOL airplane, is 43% of the approach speed of the 70-knot STOL airplane. On the other hand, the rate of onset of the gust may be lower for the 70-knot STOL airplane than for the 130-knot CTOL airplane.

An essential feature of any commercial air-transportation system, from the passenger's point of view, is the capability of that system to meet schedules regardless of weather conditions. The economic benefit of maintaining schedules in all-weather conditions has led to the development of automatic landing systems (ALS) for current CTOL jet transports. The STOL transports presently in use are not equipped with automatic approach aids for Category II operations nor with ALS and, consequently, are not yet capable of operation into very low visibility conditions. A successful STOL transport will eventually have to operate in all-weather conditions for economic reasons and this requirement will ultimately lead to the development of ALS for the STOL transport.

The Ames Research Center has undertaken a program for the development and testing of an ALS for a powered-lift STOL airplane, the Augmentor Wing Jet STOL Airplane (AWJSRA). The specific objectives of the autoland studies conducted on the AWJSRA were (1) to develop ALS navigation, guidance, and control laws for powered-lift STOL airplanes making steep microwave landing system (MLS) approaches and (2) to provide a data base for use in establishing ALS design and certification criteria for powered-lift STOL airplanes. The program began with the installation of a digital research system in the AWJSRA (ref. 10). The research system included a complete set of sensors and navigation systems as well as an electronic attitude-director indicator (EADI) and a multifunction map display (MFD), thereby providing a reliable and flexible research tool to investigate a variety of operating system concepts. The AWJSRA was equipped with parallel and series servos to provide three-axes attitude control and with servos to drive all of the other control devices on the airplane. A comprehensive terminal area operating systems program was conducted with the use of the digital research system. The program included development and evaluation of a flight director (ref. 11), design and evaluation of an advanced full-flight envelope autopilot (ref. 12), a time-constrained area navigation system study (ref. 13), a minimum-fuel autopilot system developed using optimization concepts (ref. 14), and the ALS study which is the subject of this report. The flight tests of the ALS depended on two simulation studies (refs. 15 and 16).

The control laws that were used for the AWJSRA ALS were derived from the technology used in CTOL transport autoland systems (refs. 17-19) and a growing understanding of the characteristics of powered-lift aircraft (refs. 20 and 21).

This report describes the navigation, guidance, and control laws for three ALS concepts for the AWJSRA; a two-control system that used only throttle and elevator, a three-control system that had a direct-lift-control (DLC) device to supplement the throttle, and a four-control system that employed the throttle and DLC device as well as vectored nozzles for speed control. The report begins with a review of current autoland practice as applied to CTOL transports. The airplane, the flight-test facility, the navigation system, the glide-slope track, the flare laws, and the wind disturbances encountered in flight are described. In terms of selected time histories and statistical summaries, the report shows that flight-test results alone did not expose the differences in the control laws tested; to establish the merits of the three control systems, a large number of high-speed simulation approaches and landings were used to supplement the flight-test results.

CURRENT AUTOLAND PRACTICE

Current autoland practice provides an indication of the kind of data needed to quantify performance of a STOL airplane autoland system. Autoland practice has been directed toward the conventional jet transport operating with the instrument landing system (ILS). Although the time-reference-scanning-beam (TRSB) MLS is emerging, all present autoland performance requirements are written with specific reference to the ILS even to the extent that glide-slope and localizer deviations are specified in microamperes.

A review of the FAA advisory circulars pertaining to ALS, AC 20-57A (ref. 22), and to minima for Category IIIa operations, AC 120-28B (ref. 23) indicates the following performance requirements for CTOL autoland systems.

Glide-Slope Tracking Performance

Advisory Circular AC 120-28B (ref. 23) sets forth the following glide-slope tracking-performance requirements for the Category IIIa operations.

1. The airplane is to be stabilized on the glide-slope prior to descending through 213 m (700 ft) above field level.

2. From 213-m (700-ft) altitude to flare-engage height, the airplane should track within ±35 μA, approximately ±0.16° (2 σ), or ±3.7 m (12 ft), whichever is larger, without sustained oscillations. For a 3° glide-slope, the 3.7 m (12 ft) limit applies from an altitude of 67 m (220 ft) to the flare-engage height. The ±35 μA limit translates to ±8.3 m (27 ft) at an altitude of 152 m (500 ft) and ±11.6 m (38 ft) at an altitude of 213 m (700 ft).

Autoland Touchdown Limits

AC 20-57A (ref. 22) requires that the autoland performance be demonstrated through flight evaluation supplemented with approach-simulation computer analysis. The

wind model to be used for the computer analysis includes 25-knot headwinds, 10-knot tailwinds, 15-knot crosswinds, moderate turbulence, and a wind shear of 8 knots/30 m (100 ft) from 61 m (200 ft) to touchdown. Appendix I of AC 20-57A (ref. 22) contains the wind model required by the FAA for approach simulations.

Touchdown limits are specified in terms of the 2-σ boundary and an improbable-event boundary. AC 20-57A (ref. 22) does not assign a probability number to the term "improbable event" but as a matter of practice, the FAA has accepted a probability of 10^{-6} for a recent autoland certification. The British Civil Aeronautics Authority has required 10^{-7} for the improbable event boundary. Reference 22 states that the specific requirements are: (1) The longitudinal dispersion about the nominal point of the main-landing-gear touchdown should not exceed 457 m (1500 ft) total, but need not be symmetrical about the nominal point. (2) A main landing gear touchdown must be between a point at least 61 m (200 ft) beyond the runway threshold and that point down the runway where the pilot is in a position to see at least four bars (on 30 m (100 ft) centers) of the 914 m (3000 ft) touchdown zone lights. For a recent wide-body transport, the second requirement stipulated that the improbable-event touchdown limits were 61 m (200 ft) and 792 m (2600 ft).

No further requirements on performance of the airplane or its subsystems are stated except for maintenance and training requirements. In particular, there is no requirement on control activity or on ride quality.

Clearly, the touchdown-zone requirements established for CTOL transport autoland systems will be excessive for the STOL transport because of the low-approach speeds. However, other CTOL transport guidelines, with only minor modifications, may be applicable in STOL transports. These include guidelines on the glide-slope tracking performance, the simulation wind models, and the touchdown limit probability levels. The glide-slope tracking performance may be applicable because, as noted in the introduction, the rate of descent of a low-speed STOL airplane on a steep glide slope will be nearly the same as the rate of descent of the higher speed CTOL airplane on a 3° glide slope. The simulation wind models are not aircraft dependent. Although the touchdown distance performance numbers depend on the type of airplane, the 2-σ and improbable-event probability levels for which the performance must be demonstrated do not.

EXPERIMENTAL EQUIPMENT AND SYSTEMS

The airplane used for ALS flight tests was the AWJSRA (fig. 1). This airplane had the capability of making steep approaches (7.5°) at airspeeds of about 70 knots into short runways. This airplane was developed as a cooperative effort between the NASA Ames Research Center and the Canadian Department of Industry, Trade, and Commerce. The airplane

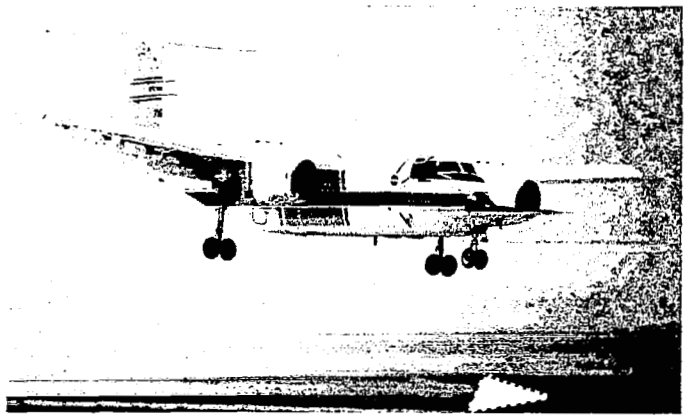

Figure 1.– Augmentor Wing Jet STOL Research Airplane.

was modified from a DHC-5 Buffalo built by de Havilland of Canada by replacing the original turboprop engines with two Rolls Royce Spey 801-SF split-flow turbofan engines and making extensive wing modifications that included installation of an augmentor flap and leading-edge slats. Other modifications consisted of reduction of the wingspan from 29.3 m (96 ft) to 23.9 m (78.5 ft) to increase wing loading, replacement of the original spring-tab elevator with a faster-responding, hydraulic-powered elevator, and installation of the spanwise augmentor ducts, nozzles, and bisurface flap system on the aft portion of the wing (figs. 2 and 3). The aft portion of the lower flap surface, labeled chokes in figure 3, was hinged so flow through the flaps could be partially

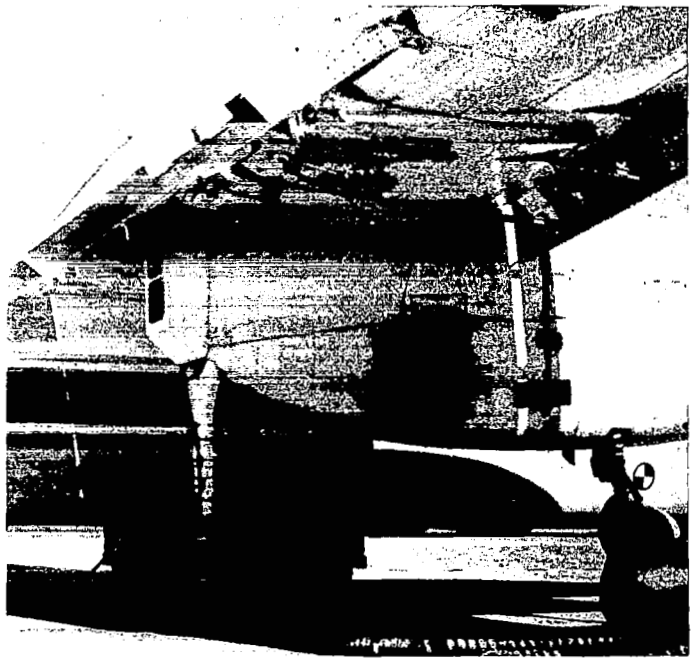

Figure 2.– Augmentor wing flap and nozzle arrangement.

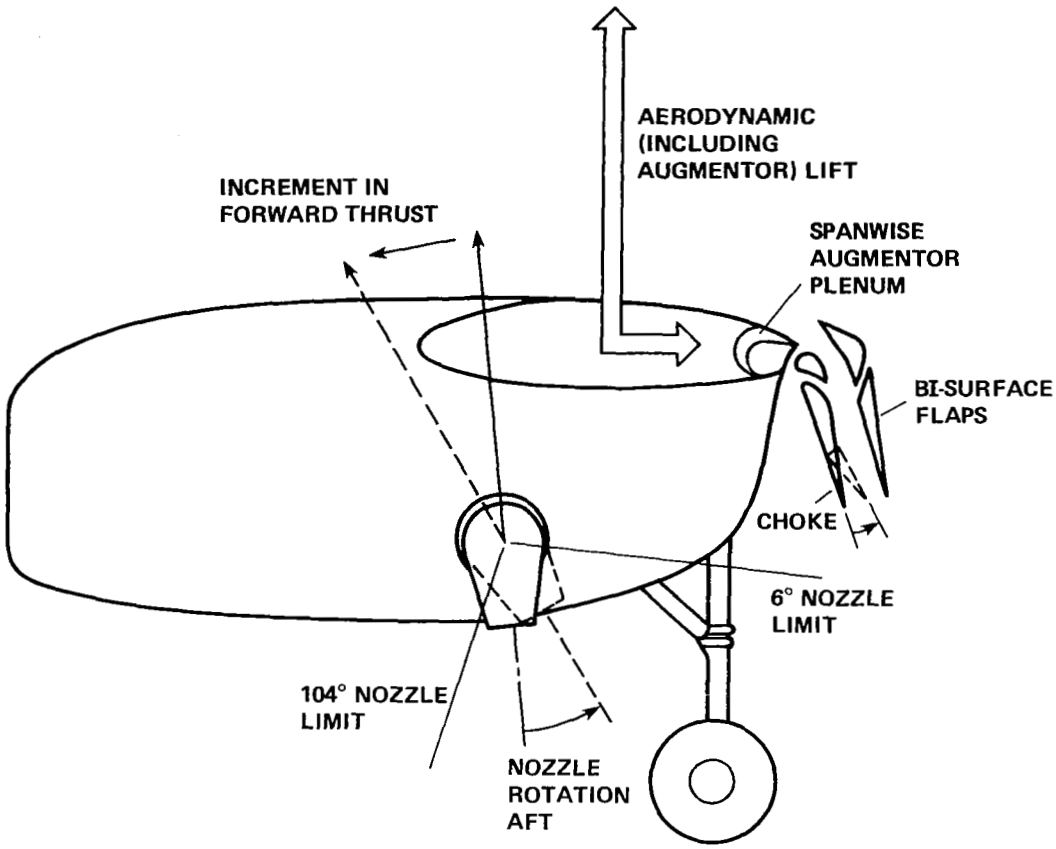

Figure 3.– Augmentor wing cross section and nozzle arrangement.

blocked. Blocking the flow decreased lift. Chokes were installed on the inboard and outboard flap segments. The outboard chokes were used differentially to supplement the ailerons and spoilers for roll control. The inboard chokes were employed for direct lift control. The longitudinal flight controls will be described in more detail later in conjunction with the control laws. Reference 24 provides a more complete description of the modifications to the airplane.

The thrust output from the engine was split into two parts – the hot thrust that was exhausted through the conical nozzles, and the cold thrust that was generated by the low-pressure turbofan air, ducted into the spanwise plenum and nozzle systems, and then ejected through the bisurface flaps to increase the aerodynamic lift and drag forces induced by airspeed. Roll upset following an engine failure was avoided by cross-ducting 65% of the fan air from each engine to the opposite wing augmentor duct. The remaining 35% of the flow was routed to the augmentor duct directly behind the engine.

Flight-Test Facility

The ALS flight-tests were conducted at the NASA Flight Systems Research Facility located at the NAVY Auxilliary Landing Field (NALF), Crows Landing, California. A simulated ground-level STOL port was located on the northern half of runway 35/17 as shown in figure 4. This STOL port was equipped with a narrow-beam MLS which had azimuth, elevation, and DME transmitters located as shown in figure 5. The dimensions of the STOL port and the location of the MLS transmitters were based on the recommendations on STOL port design contained in FAA Advisory Circular 150/5300-8 (ref. 3). The TACAN transmitter located near the intersection of the Crows Landing runways provided a navigation source when the aircraft was not in MLS coverage.

Tracking facilities– The flight-test facility provided for aircraft tracking, acquisition of on-board data through telemetry, processing and display of these data to the experimenters in real time, recording of these data for nonreal-time processing, and acquisition of weather information. Aircraft-position tracking was provided by two modified Nike-Hercules Air Defence System Radar units. Reference 25 contains a description of navigation aid and radar-tracking accuracy at the Crows Landing research facility. When radar was compared with a laser tracker, the rms range error was determined to be 1.9 m (6 ft) when the airplane was on the final approach track within 4 n. mi. of the radar antenna. Automatic azimuth and elevation tracking was employed

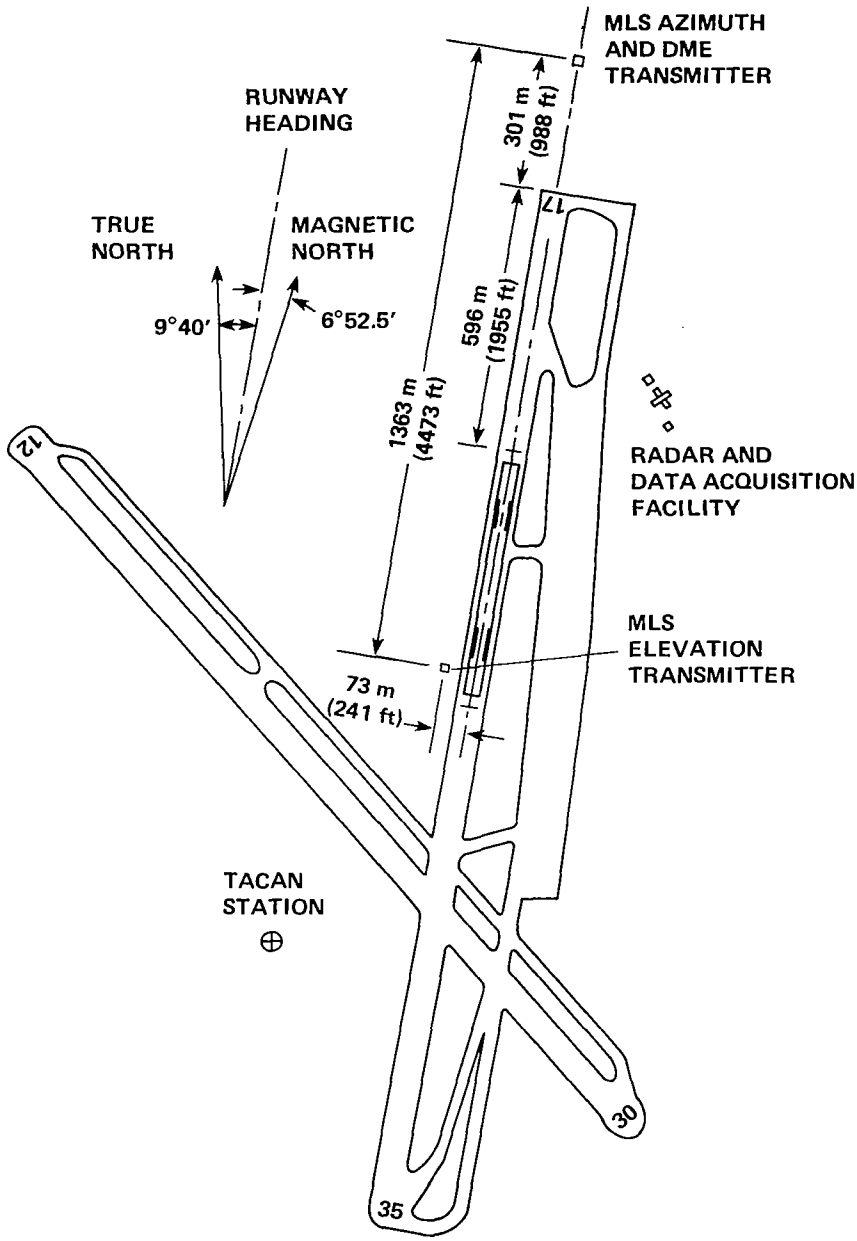

Figure 4.– STOL port location and MLS installation at the Navy auxiliary landing field, Crows Landing, California.

until the airplane was near the ground where multipath effects deteriorated elevation tracking. To overcome this multipath problem, the radar operator used a rate-control knob and a video picture from a camera mounted on the radar pedestal to manually track the airplane in elevation. The switchover to manual tracking accounts for some of the transients seen in wind-data sources discussed in appendix D.

Navigation System

All automatic landing systems in commercial use today are based on the instrument landing system (ILS). This system, described in the Airman's Information Manual (ref. 26), provides guidance to the runway centerline along a preset glide slope, typically 2.5° to 3°

Navigation facilities– A basic narrow MLS located at the Crows Landing Facility was used for the flight tests. The specification for this system is contained in reference 27. The MLS, considered an eventual replacement for ILS, provides the capability to establish optional paths in space leading to a final precision approach. The MLS azimuth, elevation, and DME signals are computer-processed to locate the airplane in any desired coordinate system. The reference approach

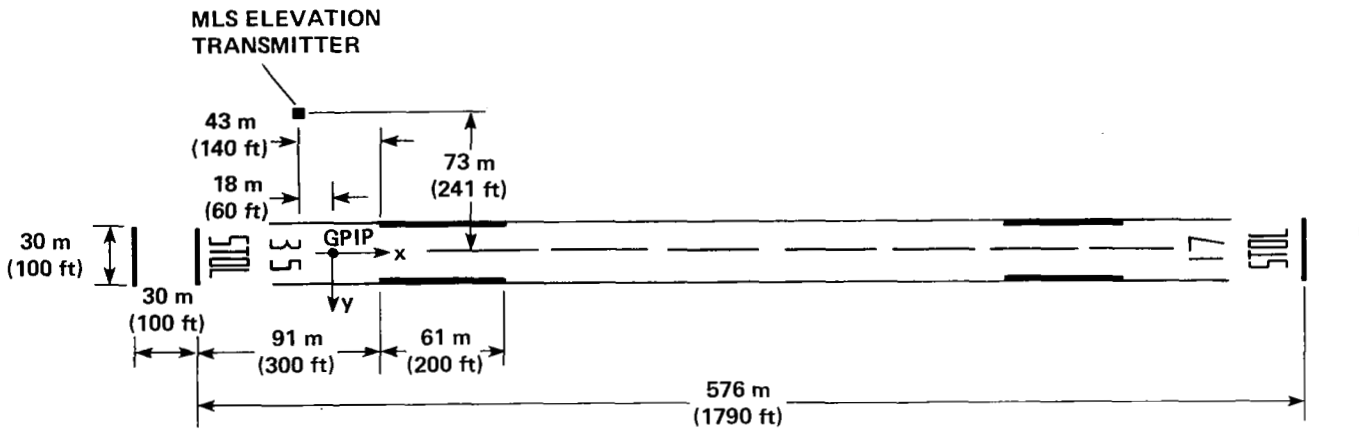

Figure 5.– STOL port layout at the Navy auxiliary landing field, Crows Landing, California.

path glide slope, based on operating requirements such as obstruction clearance, noise abatement, or airplane characteristics, is selected by the pilot.

For the AWJSRA autoland flight tests, the azimuth reference was an extension of the runway centerline and the elevation reference was a 7.5° glide-slope angle. Approaches were initiated by first capturing the extended runway centerline at a mean-sea-level altitude between 366 m and 457 m (1200 ft to 1500 ft) and then capturing the glide slope.

An onboard digital research system, which incorporated algorithms for a general-purpose navigation system, provided the aircraft position relative to the STOL port touchdown zone. The origin of the navigation coordinate system (fig. 5) was on the runway centerline abeam the glide-slope transmitter. The 7.5° glidepath-intercept point (GPIP) is 18 m (60 ft) beyond the origin. The x axis was in the airplane direction of travel for takeoff and landing, the y axis was to the right, and the z axis was down. Complementary filters blended raw-position information to produce a smooth estimate of aircraft position. The x and y complementary filters were scaled to provide a resolution of 1.2 m (4 ft) that permitted the same filters to be used over a square region with 80 n. mi. sides, encompassing NALF Crows Landing and Moffett Field, the home base of the AWJSRA. A complete description of the general-purpose navigation system appears in reference 28.

The 1.2 m (4 ft) resolution was not sufficiently accurate for the final precision autoland approach. Therefore, special purpose complementary filters were developed as part of the autoland program to provide precision glide slope, centerline, sink rate, and airspeed references. These special-purpose filters are described later.

GLIDE-SLOPE TRACK AND FLARE-CONTROL LAWS

A number of unique, longitudinal control laws were needed to accomplish automatic landings with the AWJSRA. These included the primary laws that provided commands to the throttle, choke, nozzle and elevator servos, and the complementary filters that smoothed the position, velocity, and acceleration signals. Other control laws such as those for the centerline track, runway alignment, and glide slope were needed before the glide-slope track and flare laws could be properly evaluated. The laws for centerline track and runway alignment are defined in reference 16.

The methodology used to design CTOL transport autoland systems was adopted for developing the AWJSRA autoland system. Preliminary control laws were devised and tested on a high-speed simulation to establish an estimate of glide-slope track, flare, and touchdown performance. This high-speed simulation was capable of producing 600 approaches per hour. The preliminary control laws (ref. 16) were coded into the AWJSRA airborne computer and validated for flight with a real-time simulation that incorporated the actual airborne computer, signal conditioners, and cockpit displays tied to a detailed simulation of the AWJSRA, navaids, sensors, and actuators. Flight-test results were used to refine the control laws. Final high-speed simulation data using the FAA simulation wind model (ref. 22) were generated to (1) extrapolate flight results to low-probability levels and (2) examine the sensitivity of the control laws to navigation errors and wind disturbances. The final high-speed simulation study is reported in reference 16.

Controls

The controls of interest for glide-slope track and flare were the elevator, which regulated pitch attitude; and the throttle, nozzle, and chokes, which regulated the longitudinal and vertical accelerations. The latter three controls were redundant. The specific use of the redundant controls is described in this report in the section on Control Law Configurations.

The primary powered-lift control was the power lever, generally referred to as the throttle, which regulated engine

thrust through the fuel control. The fuel control influenced the hot and cold thrust magnitude by regulating rpm. The rate of change of lift caused by the throttle can be attributed primarily to the time constant built into the engine fuel control rather than to a transport lag in the augmentor duct pressure. The fuel control was adjusted so the rpm time constant for a throttle increase was about 0.8 sec and for a throttle decrease was about 1.3 sec (ref. 29). The power decrease time constant was chosen to prevent engine compressor stall because of back pressure in the augmentor plenum following a sudden throttle decrease.

The secondary powered-lift control device was the inboard choke (fig. 3), which was electromechanically driven at rates up to 50% of total closure per second. The chokes could block flow through the bisurface flaps and thereby decrease the augmented lift. The lift change caused by the choke deflection was effectively instantaneous for the control frequencies encountered in an automatic landing system. When used for direct lift control, the chokes were first moved to a nominal position of 30% of total closure and then were regulated ±30% about the nominal position to produce a maximum incremental airplane normal acceleration of ±0.1 g. The augmentor lift that was lost when the chokes were moved from fully open to the 30% nominal position was replaced by either increased rpm or, if rpm-increase authority had to be preserved, by increased airspeed.

The hot-thrust exhaust nozzles could be rotated from the nearly directly aft position of 5° below the airplane waterline to a fully down position of 104°. For a nominal zero-wind STOL approach, the nominal nozzle rotation was about 80° below the waterline. Figure 3 indicates that rotation of the nozzle about a nominal value of 80° would cause significant change in the forward and aft component of hot thrust with little change in the vertical component. This feature suggests that nozzles could be used effectively as a longitudinal-force device for speed control.

Consideration must be given, in any control-system design, to control limits. Excessive authority can jeopardize the safety of the aircraft should a hardover actuator failure occur. Inadequate authority can lead to loss of control in the presence of severe disturbances. The nominal control settings are also of importance in a control system design. The operating limits and nominal control settings for the AWJSRA autoland system are outlined in appendix A.

Operation on the Backside of the Power Curve

During the glide-slope track along a 7.5° MLS glide slope, the AWJSRA operated on the backside of the power required curve (long term reversal of flightpath response to pitch inputs, e.g., nose up, results in a long term decrease in flightpath angle) at an approach airspeed near 70 knots with a thrust vector nearly perpendicular to the path; therefore, it exhibited unusual operating characteristics when compared with CTOL transports. The path control was effectively accomplished with the throttle, and speed control was accomplished with the elevator. This is opposite to the primary control usage for a CTOL transport. In addition, because of the inclined thrust vector angle on the AWJSRA, significant adverse coupling existed between path and speed such that a throttle increase resulted in a speed decrease. This coupling problem was resolved by developing tight tracking laws for path and speed. Further discussion of these characteristics can be found in references 20 and 21.

Control-Law Configurations

Three autoland control-law configurations were flight tested on the AWJSRA. The first of these configurations (fig. 6(a)) was designated the two-control system: the throttle provided path control and the elevator provided speed control. The second configuration (fig. 6(b)) was designated the three-control system: throttle provided long-term path control, the DLC chokes provided short-term path control, and the elevator provided the speed control. The third configuration (fig. 6(c)) was designated the four-control system: throttle and the DLC chokes provided the path control as in the three-control system, nozzle vectoring provided short-term speed control, and elevator provided long-term speed control. In each control system, the nozzle was normally positioned to maintain rpm in a favorable operating range.

A number of control-law features were developed for the four-control system. These include the glide-slope track complementary filter, the flare-law, sink-rate filter, the throttle-choke complement, and the nozzle for speed command structure. Some of these features were retained for the two-control and three-control systems primarily to minimize software development. Because all of the features were needed for the four-control system, its control laws are described first. Figure 6(c) provides an overview of the four-control system and cross references other more detailed subsystem figures.

Predict Terms

The entire control-law structure incorporated in the AWJSRA software consisted of the sum of the predict and feedback terms. The predict terms command the controls to positions for equilibrium flight conditions. The predict terms come from a map of trim conditions, called a trim table, which was derived from the AWJSRA simulation computer program described in references 30 and 31. Inputs to the trim table included calibrated and true airspeed, groundspeed, flap setting, and the reference flightpath angle. The outputs consisted of the corresponding trim settings for the throttle, elevator, DLC chokes, and nozzles.

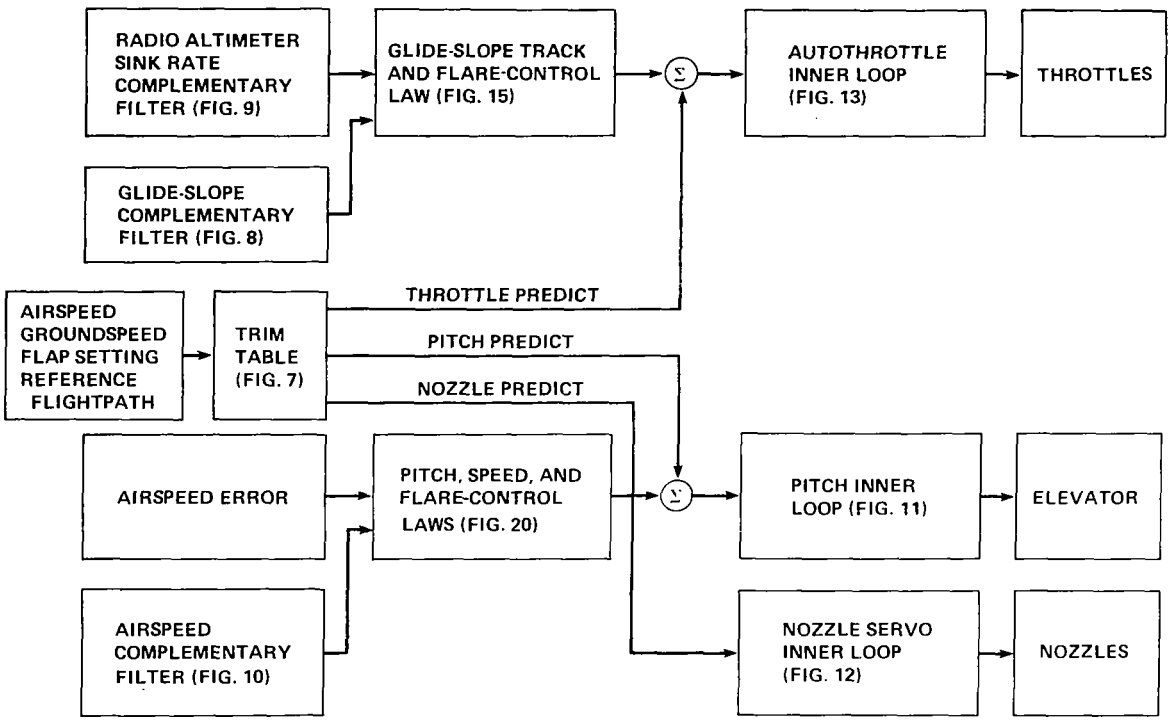

(a) Two-control system.

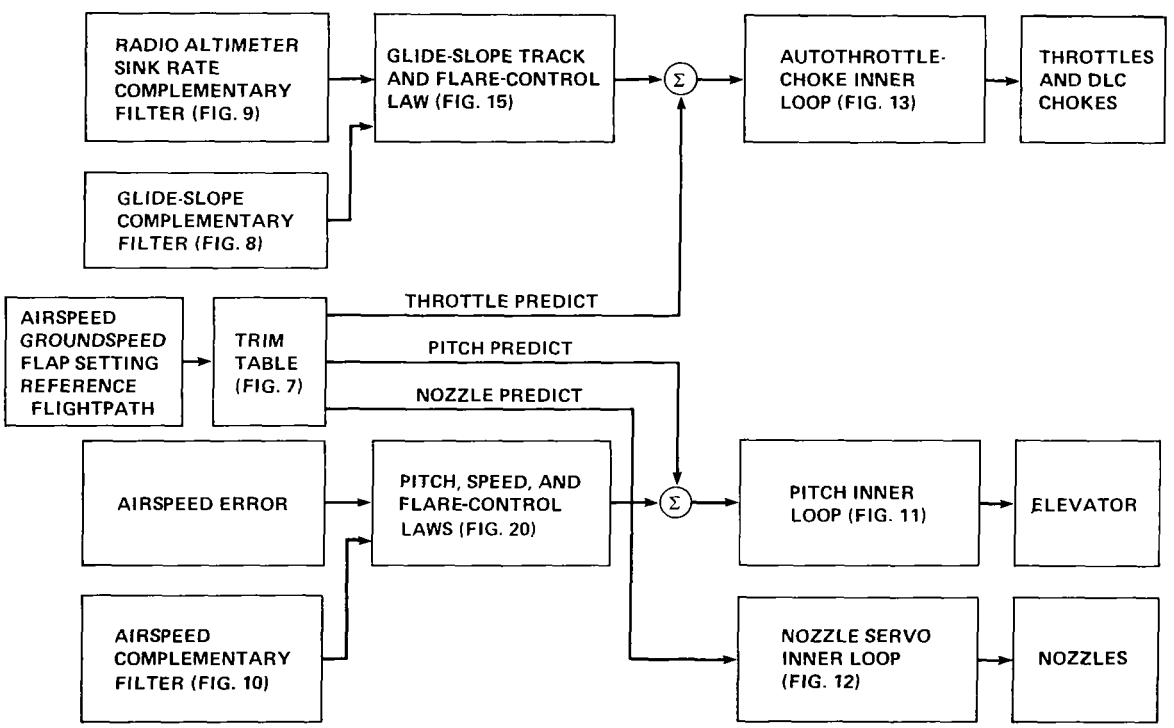

(b) Three-control system.

Figure 6.– Glide-slope track and flare-control laws.

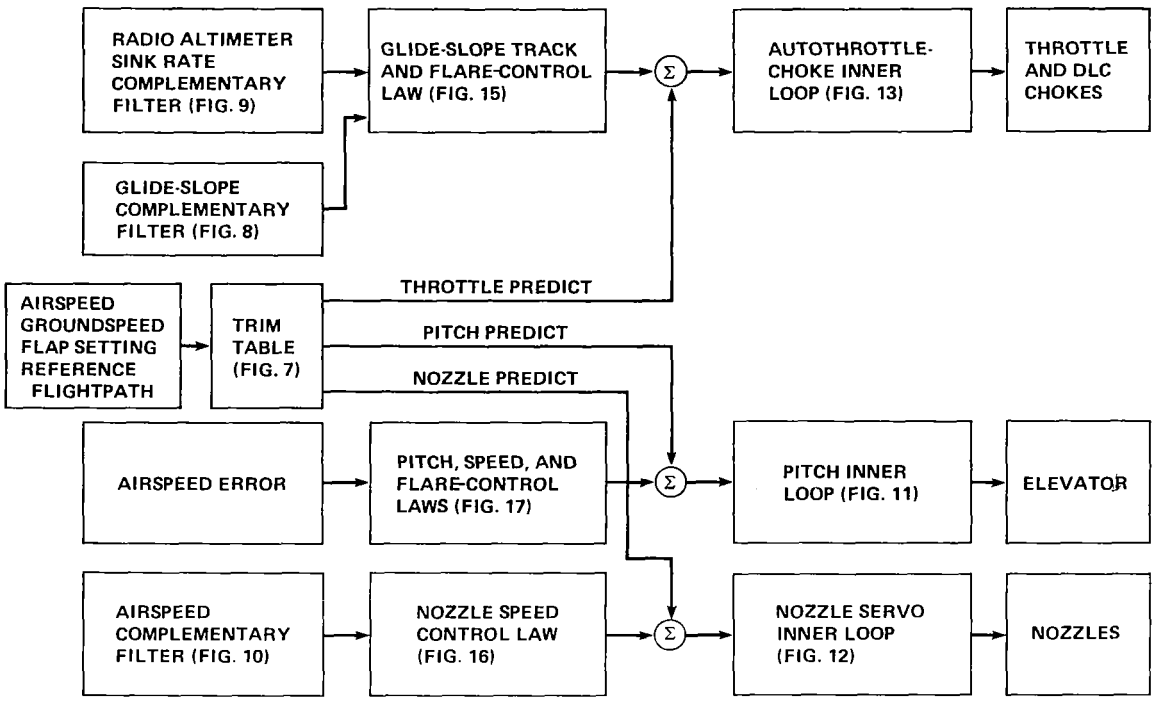

(c) Four-control system.

Figure 6.– Concluded.

The trim table was prepared by assigning values of weight, flap setting, temperature, altitude, airspeed, and flightpath angle and then using a convergence algorithm to establish the equilibrium flight condition by iterating on throttle position, pitch attitude, and nozzle position. The trim table, which was coded into the flight digital computer, is depicted in figure 7.

The predict terms were most effective when a steady-state change in flightpath angle or airspeed was required such as during a configuration change associated with a transition from level flight to glide-slope tracking. Once the airplane was established on the glideslope, the trim table output values were nearly constant unless a wind shear occurred. The lag with a 3-sec time constant, shown in figure 7, was adopted to attenuate high-frequency noise from the pitot-static airspeed sensor. Further disturbances in the pitch- and throttle-predict output values of the trim tables were avoided late in the approach by freezing these predict terms as the airplane descended through 94 m (307 ft).

The nozzle trim signal was active throughout the glide-slope track and on into the flare. As demonstrated in appendix A, the nozzle was programmed as a function of aerodynamic flightpath angle and temperature to maintain the engine rpm in an operating range which provided capability for upward- and downward-path corrections. The aerodynamic flightpath angle needed to maintain the inertial glide slope varied as a function of wind. The schedule of nozzle angle as a function of aerodynamic flightpath angle, shown in appendix A, automatically adjusted the nozzle angle to compensate for wind. The pilots used the keyboard to bias the nozzle angle to compensate for high temperature.

In theory, the entire task of controlling the airplane could be accomplished with the predict terms. However, as a result of an imperfect airplane mathematical model, disturbances, imperfect sensors, and imperfect actuators, the feedback terms were essential for successful control.

Complementary Filters

Three complementary filters provided estimates of glide-slope deviation, sink rate, and airspeed. The first, the glide-slope complementary filter, is shown in figure 8. This filter provided the smooth signal needed to drive the highly responsive DLC chokes and also provided good estimates of glide-slope deviation and glide-slope deviation rate. The principal input to the third-order glide-slope complementary filter was the glide-slope deviation signal which was the product of the glide-slope deviation angle and the slant range to a

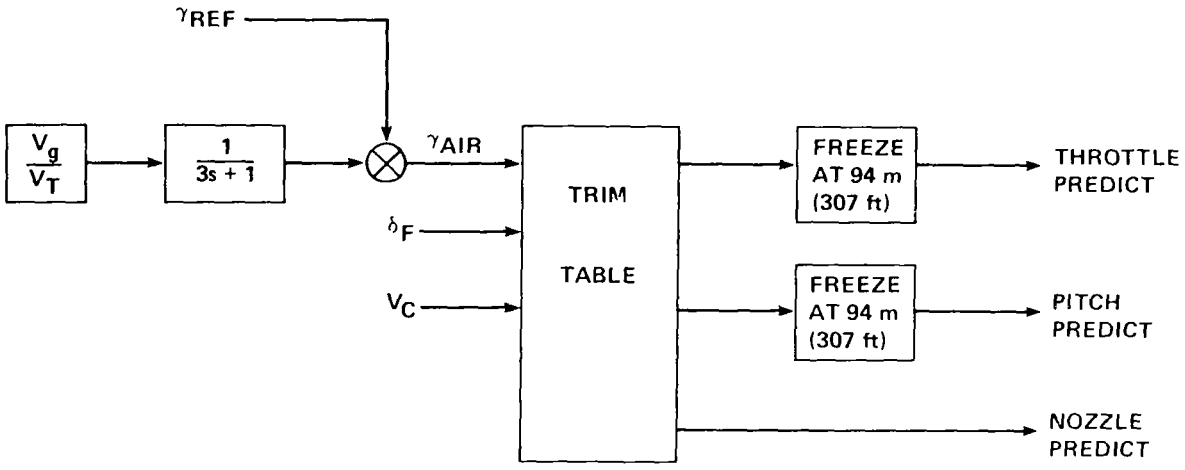

γ_{REF} – GLIDE-SLOPE ANGLE REFERENCE, deg
γ_{AIR} – AERODYNAMIC FLIGHTPATH ANGLE, deg
δ_F – FLAP SETTING, deg
V_C – CALIBRATED AIRSPEED, knots
V_g – GROUNDSPEED, knots
V_T – TRUE AIRSPEED, knots
s – LAPLACE OPERATOR

Figure 7. AWJSRA trim table block diagram.

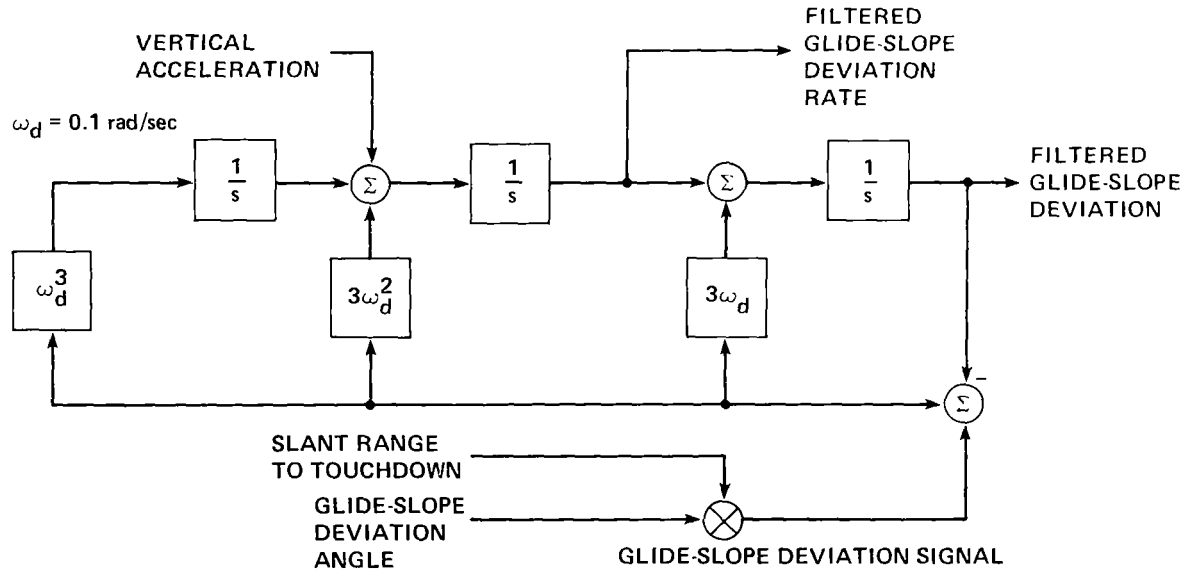

Figure 8.– Glide-slope complementary filter.

touchdown point on the runway centerline abeam the glide-slope antenna. The glide-slope deviation angle was the difference between the glide-slope reference angle, 7.5° for the AWJSRA autoland flight tests, and the MLS elevation angle. The slant range was computed from the X, Y, and Z filter elements of aircraft position. The X, Y, and Z filters are described in more detail in reference 28. The other input to the complementary filter was the vertical acceleration which was established by resolving on-board accelerometer signals into the X-, Y-, and Z-runway coordinate system. The frequency parameter, ω_d, shown in figure 8, was set to 0.1 rad/sec. The position and rate integrators in the glide-slope complementary filter were initialized when MLS was selected. To provide a smooth transition to the MLS glide slope, the initial condition of the position integrator was the difference between the MLS-derived altitude and the barometric altitude. MLS-derived altitude was computed as the distance from the glide-slope transmitter to the airplane multiplied by the tangent of the glide-slope reference angle. The initial condition of the rate integrator was the product of the true airspeed and the tangent of the glide-slope reference angle.

The second complementary filter, the radio altimeter sink rate complementary filter (fig. 9), had the same structure as the glide-slope filter except for the frequency and the reference input signal. The frequency, ω_{RA}, for the sink-rate filter was 0.6 rad/sec. The reference input signal was the radio altitude which was only valid at altitudes within 152 m (500 ft) of the terrain. In operational use, a technique for converging the sink-rate filter using MLS-derived altitude is needed to make the filter immune to irregularities in the radio altitude signal resulting from airplane passage over nonsmooth terrain prior to the STOL port. An extreme example of such surface irregularities is the step in the radio altitude signal that would occur as the airplane crosses over the edge of an elevated STOL port. A technique for transitioning from MLS-derived altitude to valid radio altitude is reported in reference 32. This technique was not developed when the AWJSRA autoland flight tests took place and was not needed because the airplane was flown over a smooth-level surface, the first half of the NALF Crows Landing runway 35 (fig. 4), for sufficient time to permit convergence of the sink-rate filter prior to the beginning of the flare maneuver.

The third filter is a second-order complementary filter (fig. 10) used for smoothing calibrated airspeed. The inputs to this filter were calibrated airspeed and the longitudinal acceleration.

Pitch Inner Loop

The pitch inner loop stabilized the aircraft attitude. Figure 11 shows the pitch-attitude inner loop which drove the elevator parallel servo. This servo was connected through a clutch to a drum attached to the cable between the control column and the power-control unit linkage of the hydraulically powered elevator. The inner loop input signal consisted of a pitch-attitude command. The feedback signals were a pitch attitude and a pitch rate. As shown in figure 11, the pitch-attitude command and feedback signals were summed and passed through the k_θ gain and subsequently summed with the pitch-rate feedback which passed through the gain, k_q. The sum of all of these signals was then gain-scheduled with dynamic pressure, q, to reduce the elevator drive signal as dynamic pressure increased. Three limiters were then applied; a limit of ±20° resulted from the digital to analog converter, a servo authority limit of ±11° was applied about the estimated trim position of the elevator and finally, a rate limit of ±24°/sec was applied.

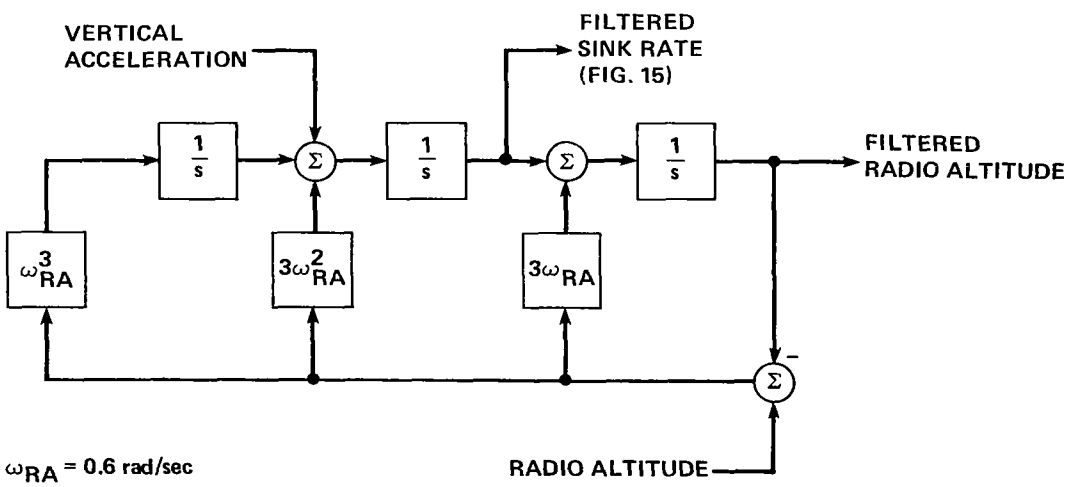

Figure 9.— Radio altitude sink rate complementary filter.

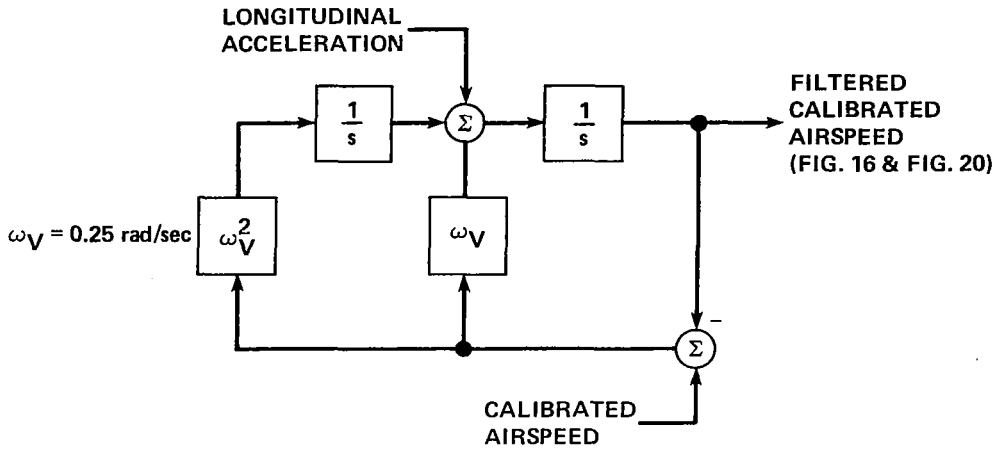

Figure 10.– Airspeed complementary filter.

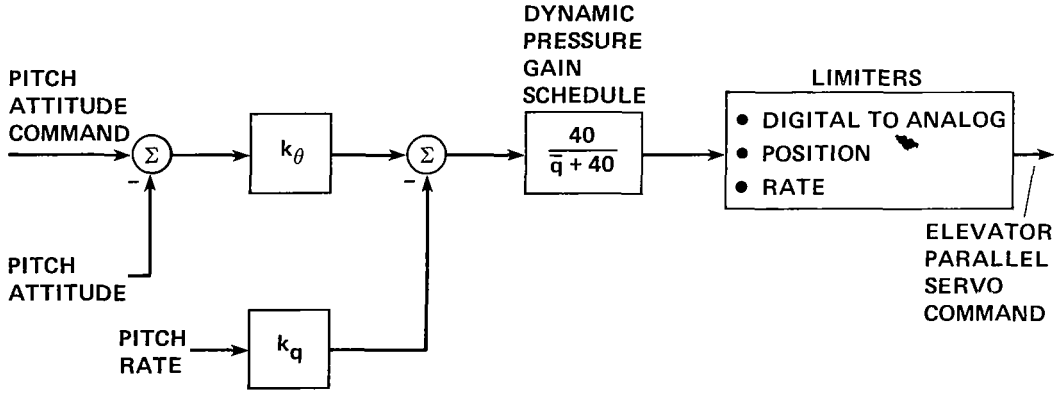

Figure 11.– Pitch inner loop block diagram.

The elevator trim actuator was driven at a rate of 0.33°/sec in a direction to offload the parallel servo whenever the drive voltage to the parallel servo, through a 2-sec lag, exceeded 10 V. Once active, the trim actuator continued to be driven until the drive voltage to the parallel servo, again through a 2-sec time constant, dropped below 6 V, at which point the trim actuator offload drive signal was set to zero.

Nozzle Inner Loop

The AWJSRA conical exhaust nozzles were rotated by an air motor capable of rates as high as full travel, approximately 100° of rotation, in less than 1 sec. The command to the nozzle air-drive motor was provided through a cable system from the pilot's nozzle handles located in the overhead quadrant adjacent to the throttle handles. Automatic control of the nozzles was provided by a rate servo coupled to the nozzle handle cables.

Figure 12 is a block diagram of the nozzle servomotor inner loop. A complementary filter smoothed the nozzle-angle feedback signal from the nozzle position transducers with integrated nozzle handle rate. The nozzle-angle transducer signals came from string-driven potentiometers mounted on one of the nozzles of each engine. The nozzle-handle rate term into the complementary filter came from the nozzle servomotor tachometer. Because of the 20-sec time constant in the nozzle complementary filter, the nozzle position estimate was heavily dependent on the nozzle handle rate. Since the position transducers were often biased, the actual nozzle angle was not well determined by this complementary filter. The nozzle error signal, the difference between the nozzle command and the nozzle-angle feedback estimate, was rate limited. During the glide-slope track and flare, the rate limit was set to 10°/sec.

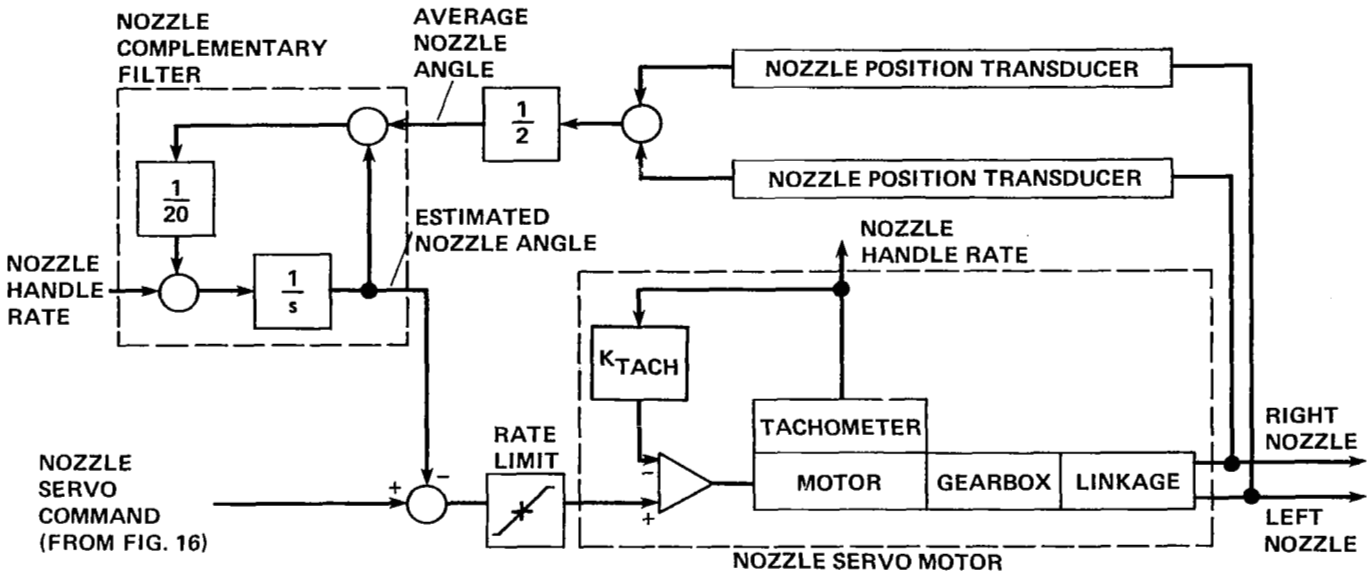

Figure 12.– Nozzle servo inner loop.

Autothrottle-Choke Inner Loop

The autothrottle servo installed in the AWJSRA was a rate-command servo of the type used in CTOL transports. The role of the autothrottle on a CTOL transport is to control speed, a task which does not require a high bandwidth since the speed-time constant of the airplane is on the order of 20 sec. On the AWJSRA, the autothrottle task was much more demanding since the autothrottle was used for precision path control during the glide-slope track and for precise sink-rate control during the flare. The autothrottle-choke mechanization described here was developed to provide the path-tracking capability necessary for the four-control system.

Figure 13 is a block diagram of the autothrottle-choke inner loop used for the AWJSRA autoland system. In figure 13, the throttle-choke command, δT_C, which comes from the path track or flare sink-rate control laws, are combined with average rpm feedback, N_H, and average throttle handle position feedback, δT_{AVE}, to produce a throttle-rate-command signal into the throttle servo, $\dot{\delta} T_C$. The feed forward gain is k_T, the throttle handle feedback gain is k_2, and the rpm feedback gain is k_3. The k_{NCH} gain is the ratio of the change in rpm to change in throttle handle position. The rationale for the values assigned to the gains is provided in appendix B. Because of the approximately 1-sec engine-time constant, τ_e in figure 13, and the rate-limited autothrottle servo, the autothrottle closed loop alone could not provide an inner-loop bandwidth above about 2.5 rad/sec. The implementation shown in figure 13 provided a means for increasing the effective autothrottle-choke inner-loop bandwidth when controlling the flightpath.

The throttle servo rate command was normally limited to ±6.28°/sec except when rpm approached the maximum limit defined in appendix A. To avoid an overshoot of the maximum rpm limit, the throttle servo-rate command was reduced to a value proportional to the increment between the limit rpm and actual rpm when the increment was less than 2%. When the maximum rpm limit was reached, the servo-rate command was set to zero. The full ±6.28°/sec throttle-rate-command authority was available for throttle retard until the minimum rpm limit was reached. The minimum rpm limit was 3% below the nominal rpm shown in appendix A. Since the full-rate-command authority was maintained to the minimum rpm limit, the actual rpm could coast below the limit value. Upon passing the rpm limit, the retard rate command was replaced by an advance-command proportional to the incremental difference between the limit rpm and the actual rpm which advanced the throttle until the minimum rpm was reached. Then the servo-rate command was set to zero. Normal servo-rate commands were resumed only when the command signal exceeded an advance command signal threshold value of 0.52°/sec.

The theoretical operation of the autothrottle-choke implementation, shown in figure 13, is presented in a simplified step response form in figure 14. In this block diagram, the autothrottle closed loop is characterized in transfer function form as described in equation (B3) of appendix B. The choke command was the difference between the autothrottle command and the engine rpm response (scaled in terms of the throttle handle position). When a step was inserted into the autothrottle servo loop, the rpm responded slowly through a second-order lag. The choke command in this example was initially a step. As the rpm began to build up, the command

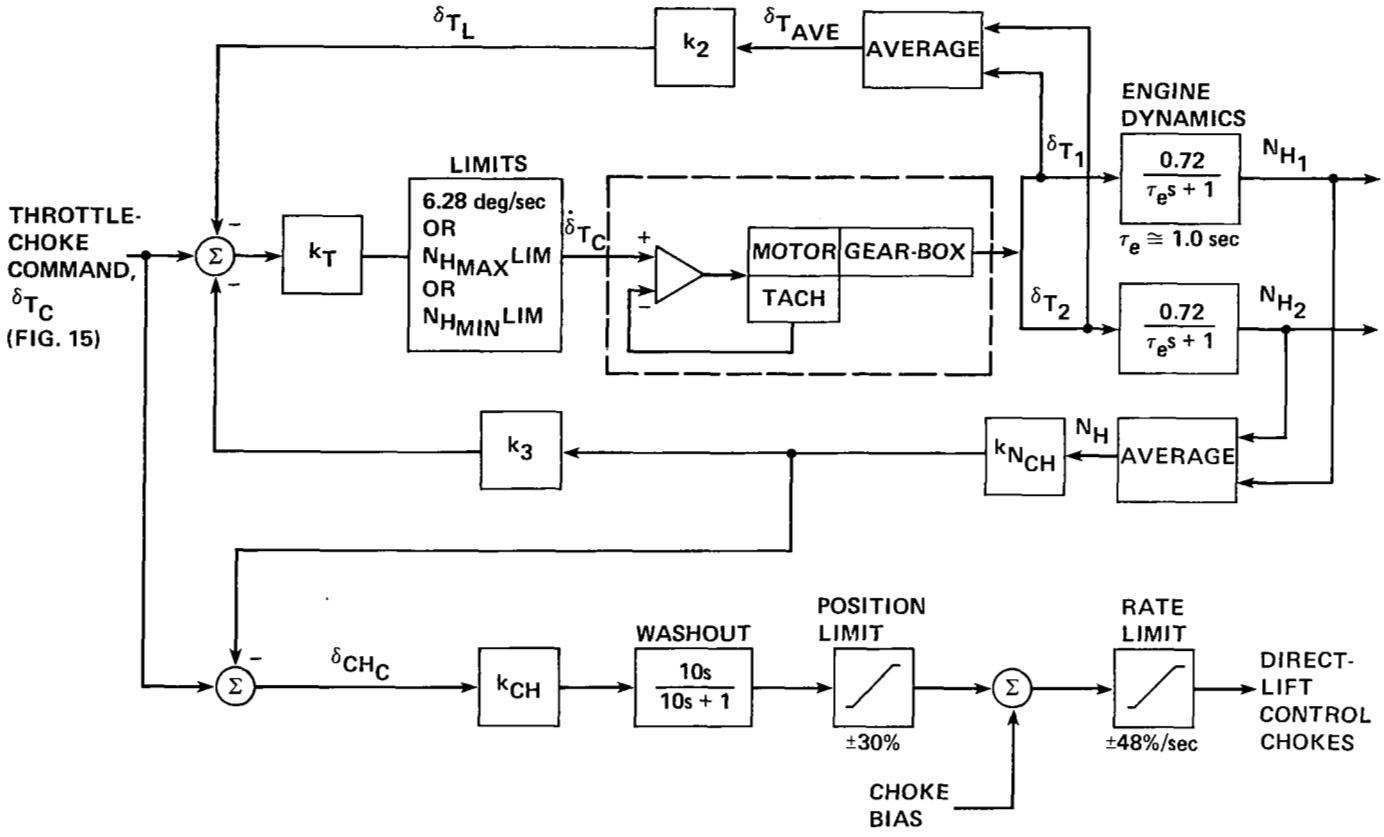

Figure 13.– Autothrottle-choke inner loop.

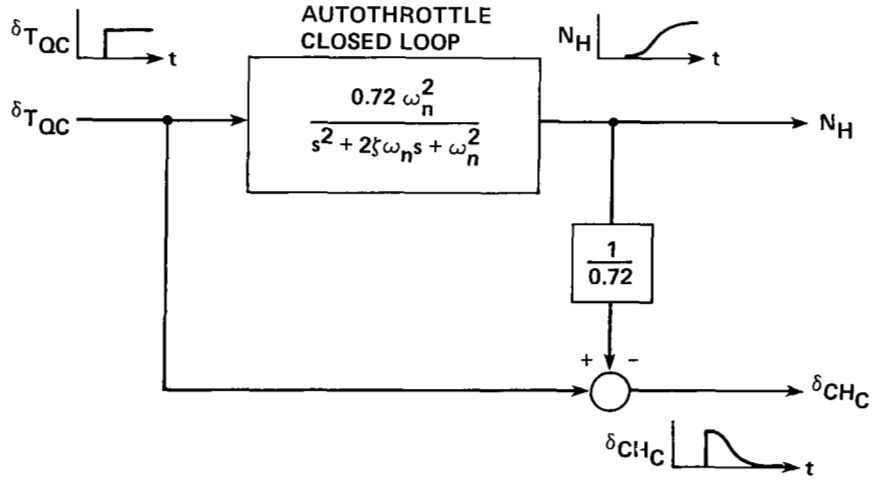

Figure 14.– Response to a step command into the autothrottle and choke.

to the choke began to decrease. By the time the rpm reached steady state, the choke command had returned to zero. Because of the high-frequency response of the chokes, the autothrottle-choke implementation provided path-tracking bandwidth greater than could be achieved from the autothrottle servo alone. The choke effectively complements the autothrottle to increase bandwidth.

The choke gain, k_{CH} (fig. 13), was chosen so the steady-state normal acceleration response to either an autothrottle or choke-position command would be the same regardless of whether the response came through the choke servo or through the autothrottle servo. In normal circumstances, the rpm-to-choke command term provided the choke washout. However, if the throttle stayed on either the maximum or minimum rpm limits described in appendix A, the rpm cross-feed term would no longer balance the autothrottle command to cancel the choke command. The 10-sec washout shown in the choke drive path in figure 13 eliminated any long term choke offsets. The chokes were limited in software to operate between 0 and 60% of closure. The choke drive signal was rate-limited in software to ±48% of closure per second to prevent choke-monitor disconnects because of large drive signals.

For the autothrottle configuration adopted for the four-control system, the autothrottle closed-loop natural frequency defined in appendix B, ω_n, was 2 rad/sec and the damping ratio, ζ, was 0.9. A faster autothrottle response was desirable but was experimentally determined to be impractical because of the maximum achievable rate of the autothrottle servo. The software rate command limit in figure 13 was set to avoid nuisance disconnects. The maximum rate of the autothrottle servo motor was somewhat higher than the 6.28 rad/sec in figure 13. However, if an attempt were made to drive the servo at a higher rate, the servo could not keep up with the command and a feedback monitor would detect the discrepancy between command and response and would disconnect the servo.

Glide-Slope Track

In figure 6, errors from the glide-slope complementary filter were nulled with commands to the autothrottle-choke inner loop. The glide-slope track control law portion of figure 15 became active at the end of the glide-slope capture and continued in effect to a radio altitude of 30 m (100 ft).

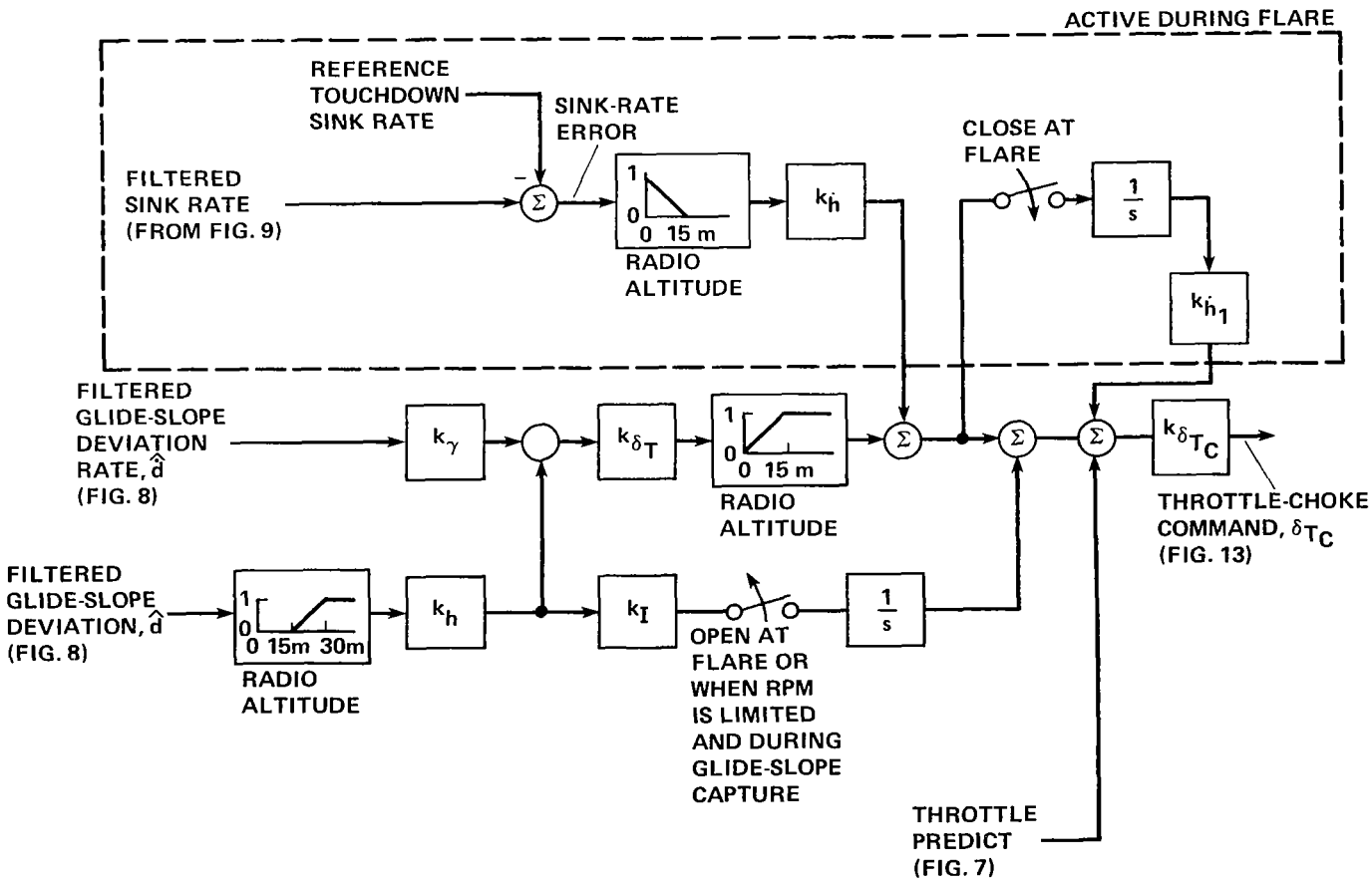

Figure 15.— Glide-slope track- and flare-control law.

Between 30 m (100 ft) and 15 m (50 ft) the path deviation gain was linearly reduced to zero. The form of the glide-slope track control law was:

$$\delta T_c = k_{\delta T_c}[k_{\delta T}(k_{I\dot{h}}\hat{d} + k_{\dot{\gamma}}\dot{\hat{d}}) + k_{I\dot{h}}k_I\int \hat{d}\,dt]$$

where δT_c is the throttle-command signal, $\hat{d}$ is filtered glide-slope deviation from figure 8 and $\dot{\hat{d}}$ is filtered glide-slope deviation rate from figure 8. The rate- and position-feedback terms provided proportional corrections to null glide-slope errors. The purpose of the integral terms was to eliminate standoff errors from the reference glide slope and to compensate for wind shears.

The flare terms in figure 15 will be discussed after the speed control during glide-slope track is examined.

Speed Control

Speed control during the glide-slope track for the four-control system was accomplished using a proportional signal to the nozzles and an integral term to the elevator. In figure 16, the proportional airspeed error was formed as the difference between the reference approach airspeed and the estimated calibrated airspeed from the airspeed complementary filter shown in figure 10. This error, when passed through the nozzle speed gain, k_{V_p}, provided the primary command signal to the nozzle servo. The error signal for the integral term in-pitch was the difference between the unfiltered calibrated airspeed and the reference approach airspeed (fig. 17). The raw airspeed could be used instead of filtered airspeed because the integral smoothed any noise present in the airspeed signal. The pitch-command signal was the sum of the speed through the integral gain, k_{I_I}, and the pitch-predict term from figure 7. The integral term provided a long-term correction for wind shear and eliminated any standoff from the reference airspeed.

The flare terms shown outlined with dashed lines in figures 15, 16, and 17 will be discussed in the section on flare which follows.

Flare

The autothrottle, chokes, elevator servo, and nozzle servo were all driven with commands during the flare maneuver. The flare began with a pitch rotation to provide aerodynamic lift to reduce the sink rate and to establish a favorable nose-up attitude at touchdown. The command to the autothrottle and choke actuators provided altitude-rate control throughout the transition from the glide-slope track to the target touchdown sink rate. A combination of a longitudinal deceleration command and a speed-error command drove the nozzles as speed decreased during the flare.

The concept of the AWJSRA autoland flare is shown in figure 18, which is an altitude versus altitude rate (sink rate), phase-plane diagram of the closed-loop flare profiles. The straight-line flare profile of figure 18 provided an exponential decay of altitude rate with time. The flare was initiated at a constant altitude from a sink rate that depended on the wind speed. The target touchdown sink rate, $\dot{h}_{TD}$, was always 0.95 m/sec (3.12 ft/sec). Since the inertial reference glide

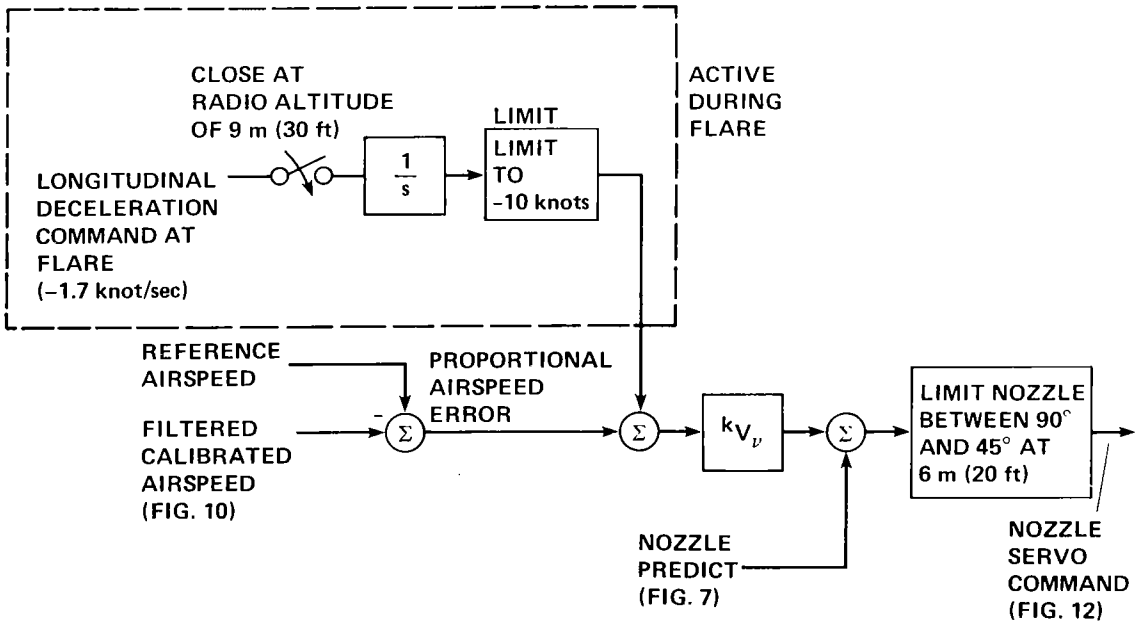

Figure 16. Nozzle speed-control law, four-control system.

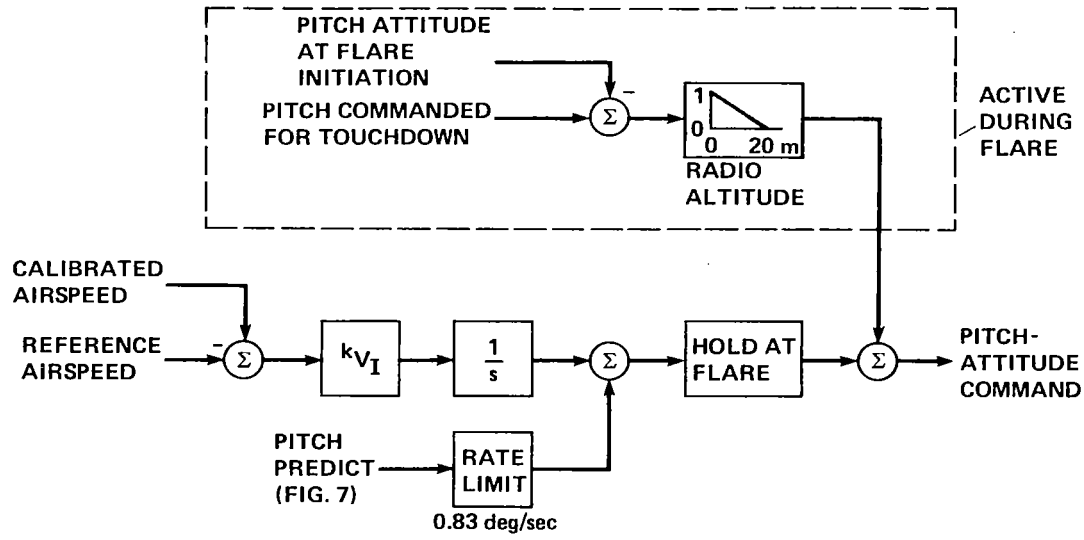

Figure 17. Pitch speed- and flare-control law, four-control system.

slope was 7.5°, the altitude rate on the glide slope prior to the flare maneuver was a function of groundspeed. Groundspeed was a function of approach reference airspeed and wind speed. Figure 18 contains altitude rate reference profiles for three different wind conditions. The profiles are constructed for an assumed constant approach airspeed of 70 knots. In a tailwind, the groundspeed was greater than the reference airspeed. Therefore, the sink rate required to track the inertial glide slope was greater than the sink rate for no wind. Conversely, in a headwind, the groundspeed was low and the sink rate was also low.

The airplane did not immediately follow the abrupt altitude rate reference-profile change depicted in figure 18. An example of the actual behavior during a calm-wind approach is shown in figure 19. The airplane altitude rate initially dropped below the reference profile but then corrected back to the profile at a radio altitude of 6 m (20 ft) and continued on down the profile to the target touchdown sink rate.

The procedure for transitioning from glide-slope track to flare began at 30 m (100 ft). Between 30 m (100 ft) and 15 m (50 ft), the filtered glide-slope deviation term in figure 15 was phased out as a function of radio altitude. The

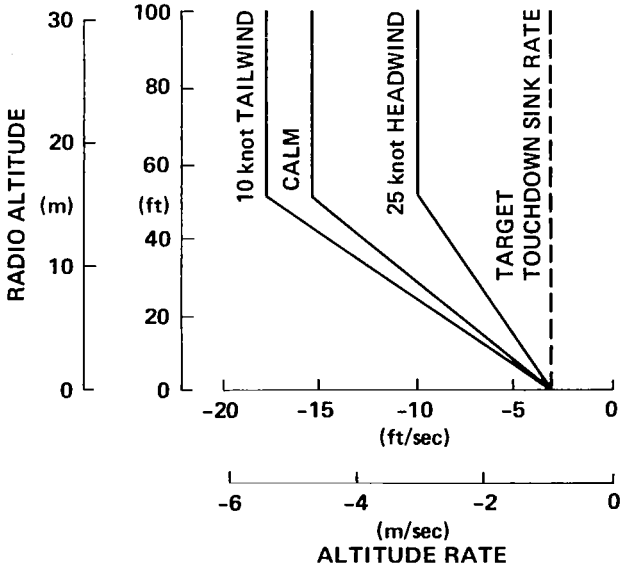

Figure 18.– Altitude versus altitude rate references for three wind conditions.

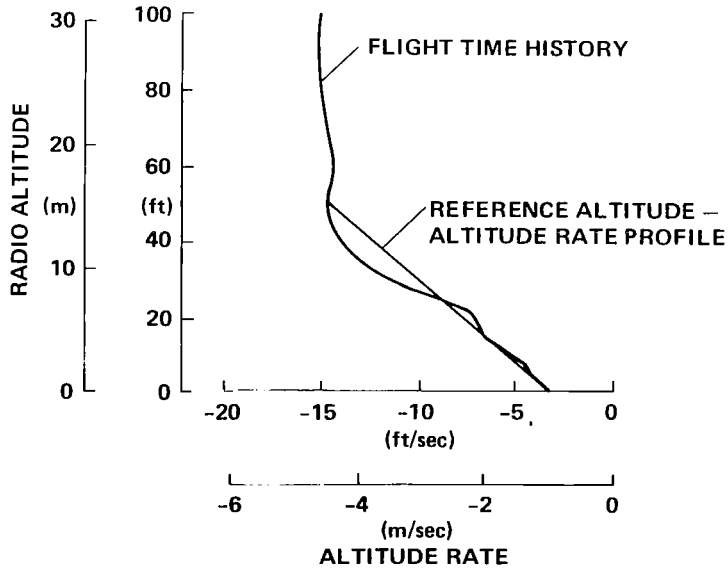

Figure 19.– Typical altitude-altitude rate profile during flare in a calm wind condition.

flare began at 20 m (65 ft) when the pitch predict and integral of airspeed error terms on figure 17 were frozen and a pitch command, θ^{c}_{TD}, to a 9° nose-up attitude was inserted into the radio-altitude-gain scheduler. The lag through the pitch inner loop attenuated the command so the airplane typically touched down with a desired 6° nose-up pitch attitude. This predictive pitch-up maneuver caused the airspeed to bleed off, partially arrested the sink rate, and ensured that the touchdown would be on the main wheels. The linear variation of the pitch-up maneuver with altitude was established on the basis of observed pilot technique during a simulation evaluation of the AWJSRA (ref. 33).

In figure 15, the filtered glide-slope deviation signal was phased out by the time the airplane had descended to 15 m (50 ft) radio altitude. Thus, at 15 m (50 ft) only the filtered glide-slope deviation-rate term remained. Reduction of altitude rate to the target touchdown sink rate began at 15 m (50 ft). Between 15 m (50 ft) and touchdown, the glide-slope deviation rate was phased out as the error from the target touchdown sink rate was phased in. The effect of the simultaneous phasing was to create the decreasing altitude rate reference shown in figure 18. The integral term, shown in the upper right portion of figure 15, was activated at flare-initiate to shorten the time needed to converge the airplane altitude rate onto the altitude-altitude rate reference line.

The filtered and calibrated airspeed command to the nozzle (fig. 16) continued to drive the nozzles throughout the flare maneuver. If the airspeed error were the only command to the nozzles, the nozzles would move aft to maintain a constant airspeed in opposition to the speed bleedoff resulting from the flare pitch-up maneuver. The longitudinal deceleration command term in figure 16 held the nozzles essentially constant throughout the flare in the absence of a wind disturbance. This allowed essentially the full-nozzle authority to be available to counter a major speed change because of a wind disturbance during the flare. The deceleration command of -1.66 knot/sec was initiated at 9-m (30 ft) radio altitude as shown in figure 16. This command was integrated, limited to a 10-knot speed-decrease command and summed with the speed-error command. The nozzle travel was limited between 90° and 45° when the airplane was below 6 m (20 ft).

Three-Control and Two-Control Systems

After the software for all the three control systems was developed, only gain changes were needed to evaluate the different systems. Table 1 lists the gains for all of the configurations that were flight tested and for a three-control system, referred to as the "Design Configuration," that was only simulated. After the three-control system (designated "Flight Configuration" in table 1) was flight-tested, errors were discovered in the scaling of the autothrottle feedback gain k_2 and in the rpm to choke gain k_{NCH} (fig. 13). The design configuration incorporated corrected values of k_2 and k_{NCH}. More details on the differences in the three control systems follow.

The principal difference between the four-control and the three-control systems was the method used for speed control during the glide-slope track phase of flight. For the four-control system the nozzles were driven by the error signal which was the difference between filtered calibrated airspeed and the reference airspeed; the integral of airspeed error provided the pitch command. For the three-control system, the proportional speed error based on filtered and calibrated airspeed, and the integral of speed error were combined to form a pitch attitude command signal as shown in figure 20. This figure shows that the filtered and calibrated airspeed from the airspeed complementary filter in figure 10 passed through the pitch proportional gain, k_{V_θ}, and was summed with the pitch-predict term from the trim table of figure 7. The sum was rate limited and added to the integral of speed-error term to form the pitch attitude command.

The pitch-flare logic shown in figure 20 for the two- and three-control systems is the same as the logic in figure 17 for the four-control system. The nozzle was driven for the three- and two-control systems to provide only a trim function as described in the section on the predict terms. The autothrottle-choke inner loop developed for the four-control system was also used for the flight configuration and the design configuration three-control systems. As shown in table 1, the only differences between the four-control system and the design configuration three-control system were in the damping ratio ζ and in the autothrottle command gain $k_{\delta T_c}$. These differences were minor. There were greater differences between the four-control system and the flight configuration three-control system.

The values of k_T and k_{NCH} used for the flight configuration three-control-system resulted in a nearly constant rpm throughout the approach; thus the burden-of-path tracking depended almost entirely on the chokes which, consequently, became very active. The frequency of the flight configuration three-control-system autothrottle inner loop was 3.5 rad/sec and the damping ratio was 1.58. Furthermore, the steady-state gain of the autothrottle loop, as determined from equation (B2) of appendix B, was not 0.72 as planned and achieved for the four-control system; rather, it was 0.23. This low steady-state gain accounts for the inactive rpm time histories for the flight-tested three-control system discussed later in this report.

Figure 13 describes the two-control autothrottle inner loop when the choke gain, k_{CH}, and the choke bias were set to zero. For the two-control system, the autothrottle inner-loop frequency ω_n was 2.5 rad/sec, the damping ratio ζ was 1.0, and the autothrottle gain $k_{\delta T_c}$ was 0.6.

TABLE 1. CONTROL-LAW GAINS FOR THE CONTROL SYSTEMS TESTED IN FLIGHT AND IN SIMULATION

Configuration	Control systems			
	Four	Three		Two
		Flight configuration	Design configuration	
k_θ, deg/deg	5.01	5.01	5.01	5.01
k_q, $\frac{\text{deg}}{\text{deg/sec}}$	2.06	2.06	2.06	2.06
k_T, $(\text{rad/sec})^2$	4.0	4.0	4.0	6.25
k_2, deg/deg	.662	2.529	.448	.650
$k_3/0.7212$, deg/% rpm	.339	.766	.766	.496
ω_n, rad/sec	2.0	3.5	2.0	2.5
ζ	.9	1.58	.7	1.0
k_{CH}, % choke/deg	10.5	10.5	10.5	0
$k_{N_{CH}}$, deg/% rpm	1.387	.385	1.387	not applicable
k_γ, $\frac{\text{m/sec}}{\text{m/sec}}\left(\frac{\text{ft/sec}}{\text{ft/sec}}\right)$	1.0	1.0	1.0	1.0
k_{δ_T}, $\frac{\text{deg}}{\text{m/sec}}\left(\frac{\text{deg}}{\text{ft/sec}}\right)$	4.72 (1.438)	4.72 (1.438)	4.72 (1.438)	4.72 (1.438)
k_h, $\frac{\text{m/sec}}{\text{m}}\left(\frac{\text{ft/sec}}{\text{ft}}\right)$	.5	.5	.5	.5
k_I, $\frac{\text{deg}}{\text{m/sec}}\left(\frac{\text{deg}}{\text{ft/sec}}\right)$	.26 (0.06)	.26 (0.06)	.26 (0.06)	.26 (0.06)
$k_{\delta T_C}$	.65	.75	.75	.6
$k_{\dot{h}}$, $\frac{\text{deg}}{\text{m/sec}}\left(\frac{\text{deg}}{\text{ft/sec}}\right)$	4.59 (1.4)	4.59 (1.4)	4.59 (1.4)	4.59 (1.4)
$k_{\dot{h}_1}$, 1/sec	.5	.5	.5	.5
k_{V_v}, deg/kt	5.55	0	0	0
k_{V_I}, $\frac{\text{deg/sec}}{\text{kt}}$	.051	.051	.051	.051
k_{V_θ}, deg/kt	0	.42	.42	.42
θ^c_{TD}, deg	9	9	9	9
$\dot{h}^c_{TD}$, m/sec (ft/sec)	.95 (3.12)	.95 (3.12)	.95 (3.12)	.95 (3.12)

FLIGHT-TEST RESULTS

Three different control law systems were flight tested: the four-control, three-control, and the two-control systems. Each of these systems was developed to the point of providing good glide-slope tracking and flare performance. Further minor refinements to the glide-slope track and flare systems would have been desirable but would not have substantially improved the final system performance.

The results are presented in three forms: (1) time histories, (2) exceedence plots, and (3) summaries (appendix E). Time histories of selected approaches are used to

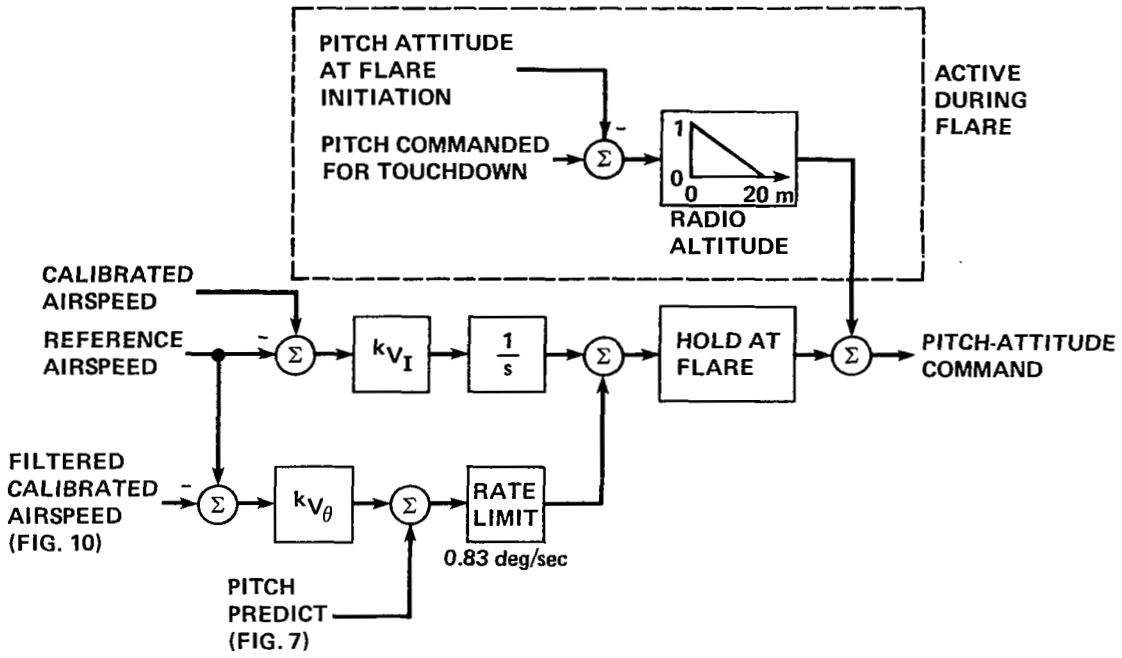

Figure 20.– Pitch speed and flare control law for the two- and three-control systems.

identify distinguishing characteristics of each of the control-law configurations. Exceedence plots relate the small sets of flight-test data to the much larger sets of data available from the high-speed simulation. Summaries of the flight-test parameter mean values and standard deviations, taken throughout the glide-slope tracking phase of the approach, are provided in appendix E.

A number of disturbances affected the behavior of the airplane during the approach. These included winds and MLS noise in the azimuth, elevation, and DME signals. The simulator studies reported in reference 16 provided the insight that atmospheric disturbances dominated system performance. The next section relates the winds recorded during flight testing to the wind models used for simulation studies.

Wind Conditions

Wind data were recorded during flight tests from two sources: from an anemometer located on a mast near the STOL port touchdown zone and from a postflight computation that established the wind vector as the difference between the airspeed derived from the pitot-static system of the airplane and groundspeed derived from tracking radar. The procedures used to gather these data and an estimate of the accuracy of these data are presented in appendix D.

Wind was the single major disturbance acting on the airplane during the autoland approaches. A knowledge of the winds is therefore necessary to understand the behavior of the control laws.

Reference 34 presents wind-probability data on a number of airports around the world. Figure 21 shows a comparison of the wind-magnitude data obtained from a 5.5 m (18 ft) mast near the touchdown zone at NALF Crows Landing with data from reference 34. The curve labeled 24 U.S. airports was developed from data accumulated from anemometers mounted at a height of 6 m (20 ft). The curve labeled ARB (for British Air Registration Board) represents data from airports around the world. The higher wind speeds associated with the ARB curve are assumed to be the result of anemometers being mounted at the greater height of 10 m (33 ft). These two curves are approximately the same as the downwind probability curve specified by the FAA for automatic-landing-system simulation studies as shown in AC 20-57A (ref. 22). The low ceiling and visibility curve from reference 34 shows that the wind magnitude tends to be lower during periods of fog with visibility of 0.5 n. mi. or less and no precipitation. Wind-magnitude data accumulated during the AWJSRA autoland flight-test approaches were plotted for comparison with the published wind-speed descriptions from reference 34. Although the three-control-system wind data appears to correlate with the low ceiling and visibility curve of figure 21, this is just coincidence because the three-control data are attributable to thermal turbulence associated with light winds and high temperatures. At probability levels above 20%, the wind magnitude encountered by the two- and four-control systems were less than the low ceiling and visibility curve. At probabilities below 20%, wind magnitudes were as great or greater than the 24 U.S. airports or the ARB data. These high wind

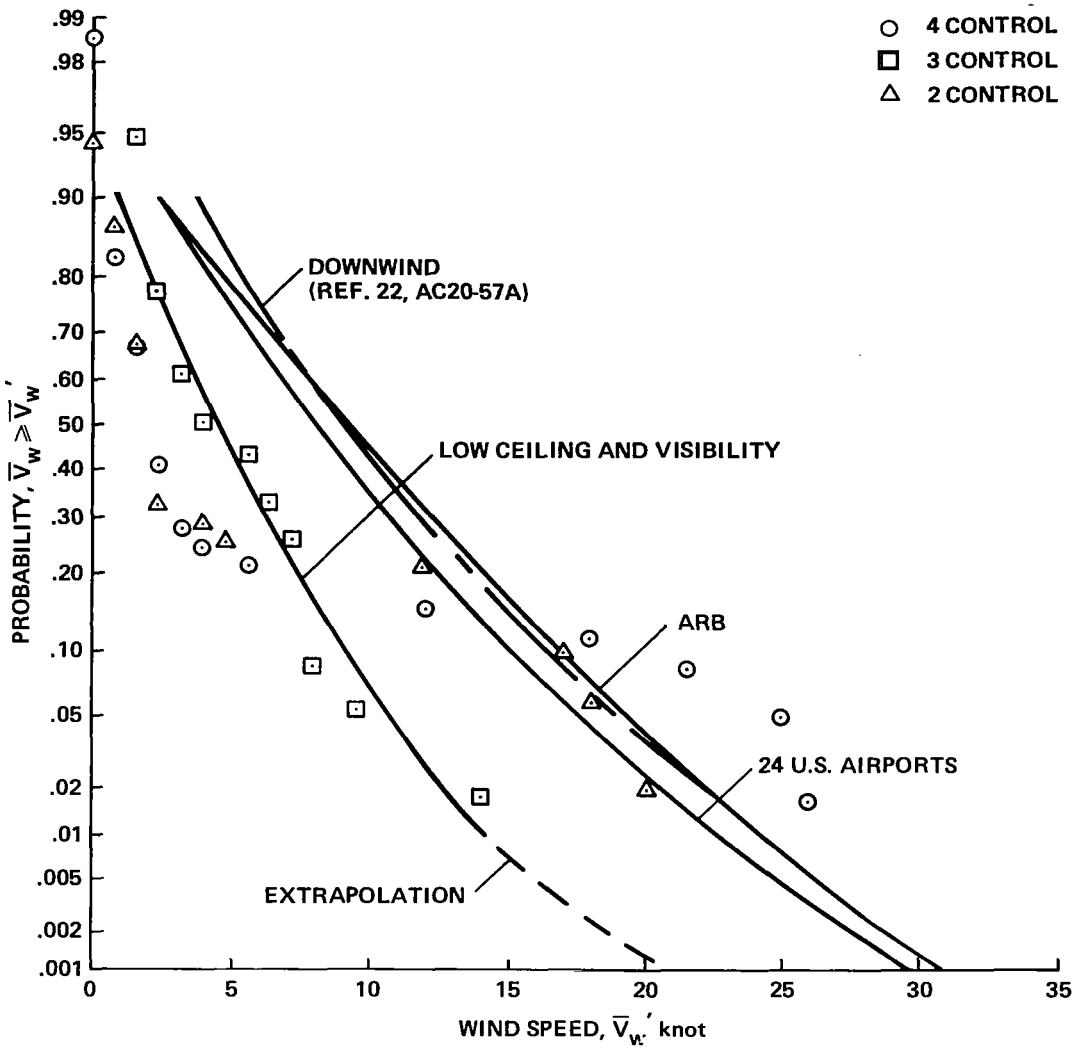

Figure 21.– Comparison of mast-determined wind data obtained during AWJSRA autoland flight testing with published wind-speed descriptions.

conditions were particularly useful in demonstrating the capabilities of the AWJSRA autoland system for coping with representative severe conditions.

Glide-Slope Track Performance

The time histories shown in this section demonstrate how the control laws performed in flight in various wind conditions. The time histories began just before glide-slope capture and ended after the touchdown. Although the primary emphasis in this section is on the portion of the approach which began when the airplane was stabilized on the glide slope and ended with flare entry, a brief description of the glide-slope capture procedure will explain the events during the first portion of the time histories.

The glide-slope capture law was based on the idea that the capture could be accomplished along a constant, normal-acceleration, circular path by freezing power setting and changing the airplane configuration. In the case of the AWJSRA, which had a fixed landing gear, the configuration change consisted of lowering the flaps, rotating the nozzles, and ramping the chokes to the nominal 30% closure position. A 20-sec circular, arc-capture maneuver was selected as a compromise between the requirement to establish glide-slope tracking as soon as possible and the desire to avoid a large, normal-acceleration and associated big control motions. Establishing glide-slope tracking quickly is especially important in a tailwind. Excessive control motion can result in instability due to control saturation. The equations describing the glide-slope capture are derived in appendix C.

A number of events occurred during the glide-slope capture. The path reference became -7.5° and the airspeed

reference became the landing approach airspeed (LAS). The nozzles were rotated to the nominal approach reference setting and the chokes were ramped to their 30% nominally deployed position. The throttle gain was reduced to maintain a constant rpm during capture. Following the configuration change, both the choke and throttle gains were gradually increased to the final glide-slope track values.

The glide-slope capture law used for the AWJSRA autoland flight tests was effective in the sense that the airplane was almost always established on the -7.5° glide slope with sufficient time remaining to ensure stabilized tracking from 152 m (500 ft) to the flare initiation altitude. However, frequently there was an objectionable overshoot in the capture maneuver. Further development would have been required to perfect this law. Other flightpath angle transitions were developed and tested during the AWJSRA research program in connection with area navigation-system developments. The most effective of these procedures is reported in reference 12.

Calm Wind.– Figures 22(a) and (b) show the performance of the four-control system operating in calm wind conditions. Following a capture involving a single glide-slope error overshoot, the airplane was well stabilized on the glide slope below 244 m (800 ft) barometric altitude. During the capture the nozzles and chokes were deployed to their nominal operating positions, the throttle and choke gains were initially reduced to avoid large control transients and were subsequently ramped to the final glide-slope track values. In figure 22(a) the deployment of the choke and nozzle occurred between 2 and 12 sec into the record. Throttle and choke gains were increased during the period between 30 and 45 sec, and the full glide-slope gain configuration was established after 50 sec.

The path and the speed tracking were satisfactory when the airplane was below 244 m (800 ft) barometric altitude. Specifically, in figure 22(a) the glide-slope error did not exceed 1.5 m (5 ft) relative to the 7.5° reference glide slope and in figure 22(b) the speed was within 4 knots of the 70-knot landing approach airspeed (LAS) reference.

The design features of the four-control system that are evident in figures 22(a) and (b) are summarized next.

Figure 22(a) shows that the autothrottle-choke complement was an effective path controller. However, the rpm and chokes were surprisingly active considering the calm surface wind conditions and the standard day temperature. Although the glide-slope errors were small, the glide-slope tracking was not absolutely smooth.

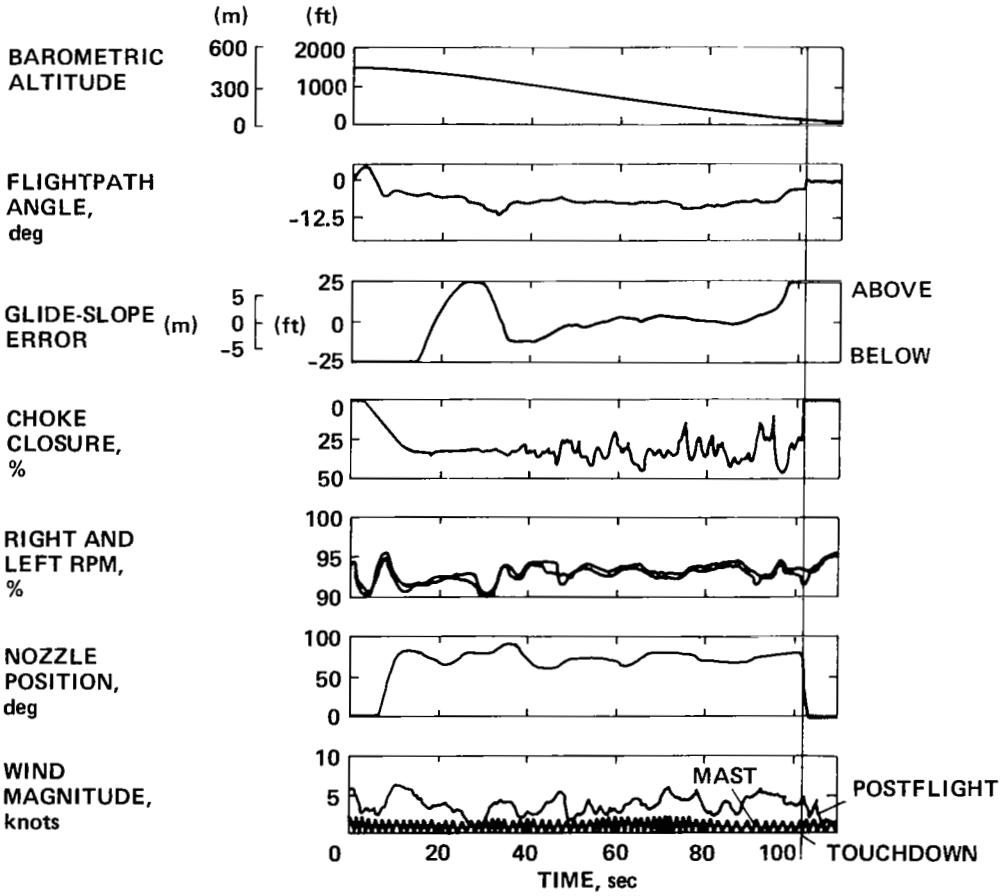

Figure 22(a).– Glide-slope track and flare performance of the four-control system; calm wind, standard day temperature.

Figure 22(b) indicates that although the speed stayed within 4 knots of the landing airspeed (LAS) reference of 70 knots, the nozzle-control activity was high. This activity was apparently due to hysteresis in the nozzle-drive system. Big speed errors were handled adequately but small errors were uncorrected because the error signal was not large enough to break through the nozzle hysteresis.

Figure 22(b) also shows that just after the glide-slope capture, when the airplane was above 244 m (800 ft) barometric altitude, the nozzles and pitch attitude were operating in opposition while correcting airspeed errors. The sequence began 30 sec into the record. Airspeed at this point was 2 knots above the 70-knot LAS reference speed and was increasing to 5 knots above LAS. The nozzle angle was increasing and the integral of speed error was pitching the nose up to slow the airplane. At 37 sec into the record, the airspeed was dropping through LAS on its way to 4 knots below the 70-knot reference speed. At this point, the nozzle angle decreased to provide a force in a direction to increase the airspeed. Note the change in the longitudinal acceleration. At 40 sec into the record, the airplane was pitched 2° nose-up above the final trim value to slow the airplane while the nozzle angle was decreased to increase the airspeed. This was a case where the nozzle moved excessively to compensate for the slowly changing pitch-attitude integral term. This integral term for speed on pitch was essential to keep the nozzles centered in their operating range. However, the integral gain was small to reduce a long-term oscillatory tendency. At 50 sec into the approach, the pitch attitude had settled to minus 2° where it remained until flare initiation.

The throttle and choke inner loop effectively nulled path errors and the nozzle and elevator effectively maintained speed. The elevator trace in figure 22(b) is an indication of the column activity that the pilots observed and corresponds to about 0.5 cm (0.2 in.) of column travel.

The angle of attack in figure 22(b) exceeded 12.5° momentarily just after the glide-slope capture as the system corrected for the glide-slope capture overshoot but was steady near 7.5° after the airplane was stabilized on the glide slope. The pilots objected to the high angle of attack and the associated low airspeed that occurred early in the approach but considered the final track angle of attack and airspeed to be acceptable.

The normal acceleration trace appears in figure 22(b). Normal acceleration provides one measure of ride quality. According to reference 35, rms normal acceleration levels under 0.09 g are considered acceptable to passengers provided lateral rms acceleration does not exceed 0.06 g. By this

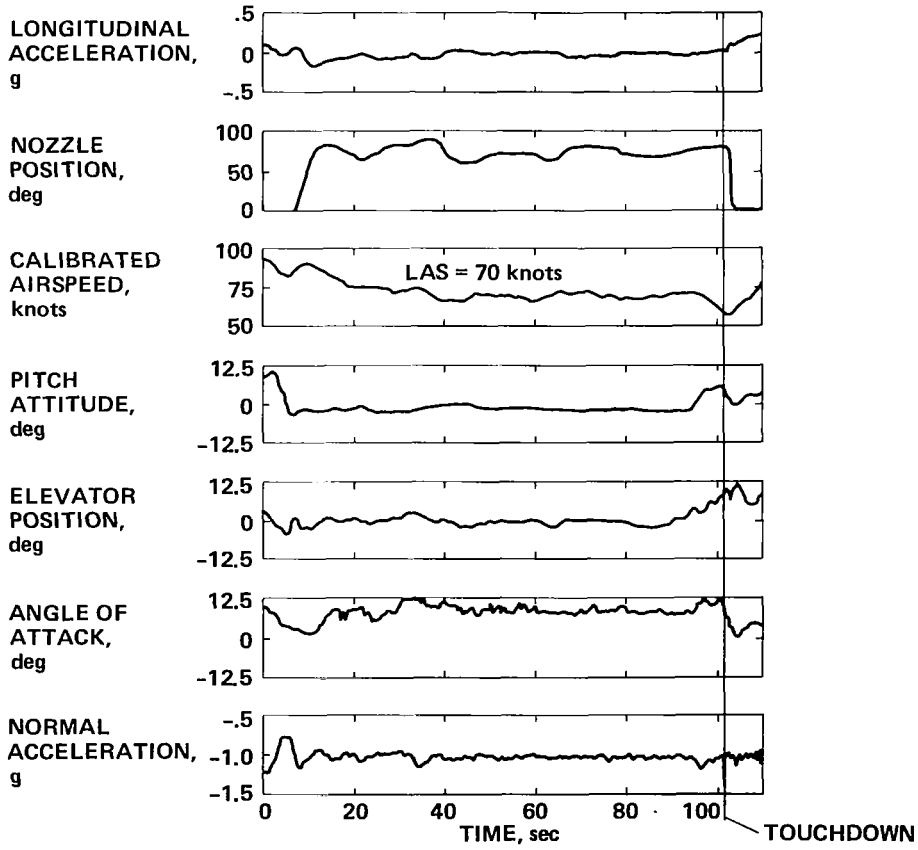

Figure 22(b).— Glide-slope track and flare performance of the four-control system; calm wind, standard day temperature.

criterion, the glide-slope tracking performance of the AWJSRA autoland system was acceptable for this particular approach.

One of the pilots commented that the choke activity associated with the four-control and three-control systems was high. In some cases the chokes were driven all the way open. When the choke motion was small enough to keep each choke operating near the 30% nominal position, the pilots were not aware of the choke activity. When the pilots were asked specifically about the acceptability of the high-frequency choke activity they commented that the chokes were less objectionable than the nozzles. The pilots were aware of the nozzle activity because they could feel longitudinal acceleration when the nozzles moved and because the motion of the nozzles was reflected back into the nozzle handle in the cockpit. Figure 22(b) shows that the longitudinal acceleration was from -0.1 g to 0 g during the latter half of the approach.

Figures 23(a) and (b) show the performance of the flight configuration three-control system operating in light but not calm wind conditions. The light wind activity evident in figure 23(a) was caused by thermal disturbances over the runway associated with the high temperature which was 17° C above standard day temperature.

The primary performance difference between the four-control system (figs. 22(a) and (b)) and the flight configuration three-control system (figs. 23(a) and (b)) was the higher choke activity of the three-control system. As discussed earlier, this difference was due to the reduced-throttle feedback and rpm to choke crossfeed gains used for the flight configuration three-control system that caused the increased choke and decreased rpm activities.

The basic design difference between the four- and three-control systems was the method of controlling airspeed. The three-control system depended entirely on pitch corrections for speed control, whereas the four-control system used nozzles for short-term speed corrections. Figure 23(b) shows that speed stayed within ±2 knots of the 75-knot airspeed reference. The nozzle angle was constant after the glide-slope capture maneuver was completed. Consequently, the longitudinal-acceleration time history shown for the flight three-control system in figure 23(b) is smoother than the comparable time history for the four-control system shown in figure 22(b).

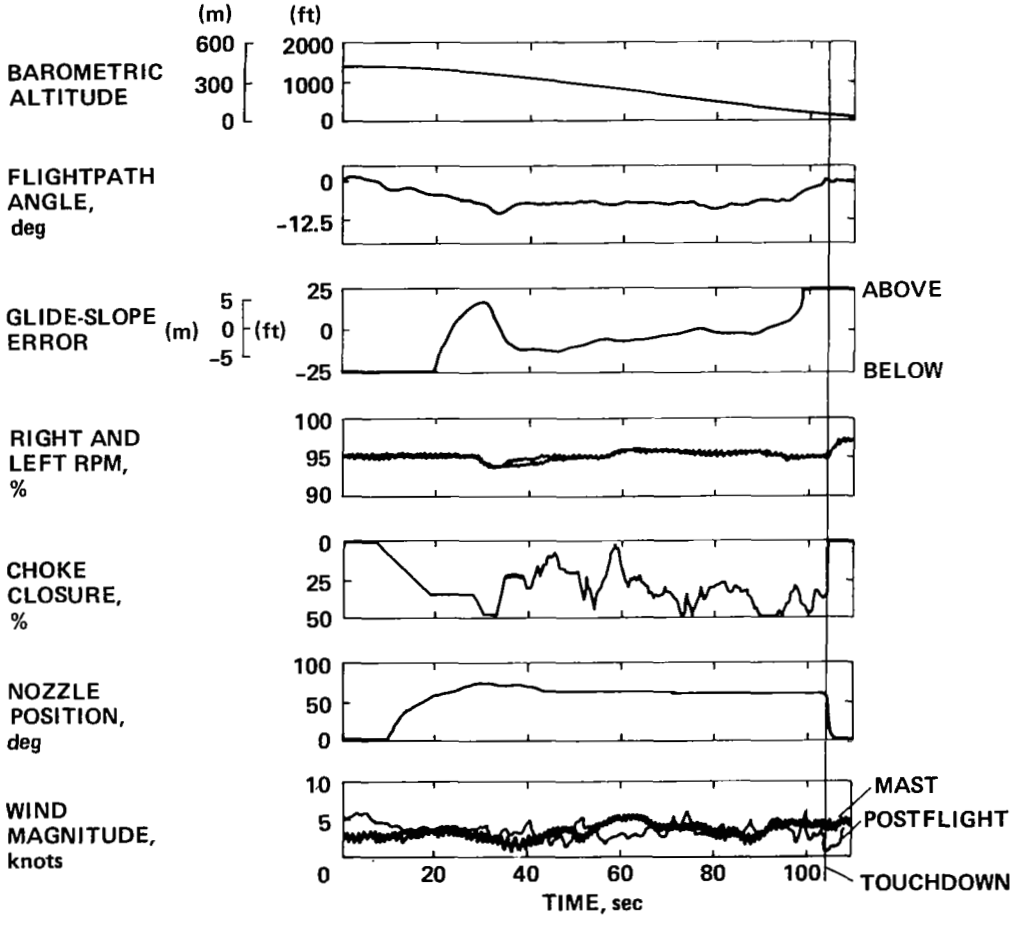

Figure 23(a).– Glide-slope track and flare performance of the flight three-control system; calm wind, standard day at +17°C.

The high temperature day caused the rpm to be higher than was generally considered desirable. The rpm in figure 23(a) operated between 95% and 96%, which was 1% to 2% above the nominally desired value of 94% for the approach weight of 19,504 kg (43,000 lb). The angle of attack was also high; just prior to flare entry, the angle of attack was 10°. The pilots preferred an angle of attack closer to 7°. This could have been accomplished, using the tradeoff factors developed in appendix A, by raising the airspeed 2 knots to lower the rpm 1% and lower the angle of attack 1°. Although adjustment to the airspeed and rpm would have produced more nominal trim conditions, these adjustments would not have affected the speed error or path-tracking performance. The main adverse effect of the higher airspeed associated with the higher temperatures was the increased landing distance.

Figures 24(a) and (b) and 25(a) and (b) demonstrate (1) the performance of the two-control system in calm surface wind conditions, and (2) the effect of the path-tracking gain, $k_{\delta T_c}$ (fig. 15), on the rpm and normal-acceleration responses of the two-control system. In figs. 24(a) and (b), $k_{\delta T_c}$ = 0.75 and in figures 25(a) and (b), $k_{\delta T_c}$ = 0.6. The postflight wind-magnitude records in figures 24(a) and 25(a) indicate a headwind near 15 knots just before glide-slope capture which decreased to calm by the time the airplane had descended below 152 m (500 ft).

The autothrottle inner-loop frequency was set to 2.5 rad/sec and the damping ratio was 1.0 for the two successive approaches (figs. 24 and 25). The only control-system difference between the two approaches was the value of $k_{\delta T_c}$. There was a pronounced oscillatory tendency in the engine rpm in figure 24(a) which was not evident in figure 25(a). This oscillatory tendency is also seen in the normal acceleration record in figure 24(b). The overall glide-slope tracking performance was the same for both gains. There was also no difference in the airspeed-tracking performance or elevator activity when $k_{\delta T_c}$ was varied. To avoid the oscillatory rpm and normal acceleration tendency, $k_{\delta T_c}$ was set to 0.6 for the subsequent two-control-system approaches.

The path tracking performance for the two-control system (fig. 25(a)) can be compared with the performance of the flight configuration three-control system (fig. 23(a)) and the four-control system (fig. 22(a)). All three systems provide performance that would meet the FAA requirements

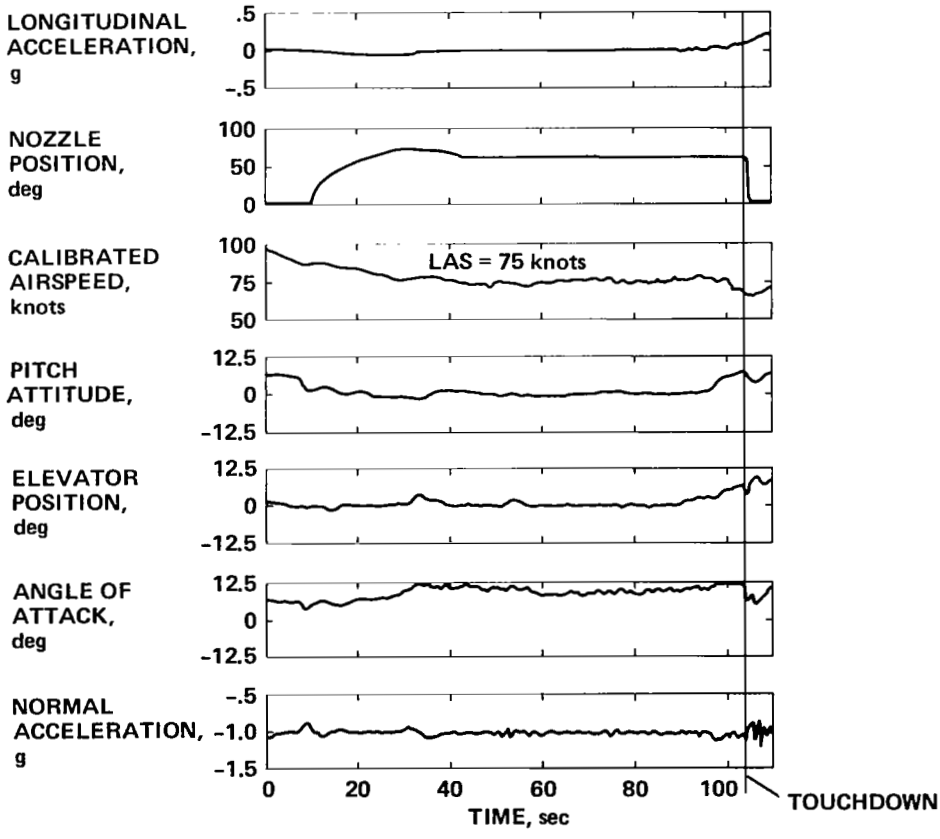

Figure 23(b).– Glide-slope track and flare performance of the flight three-control system, calm wind, standard day at +17°C.

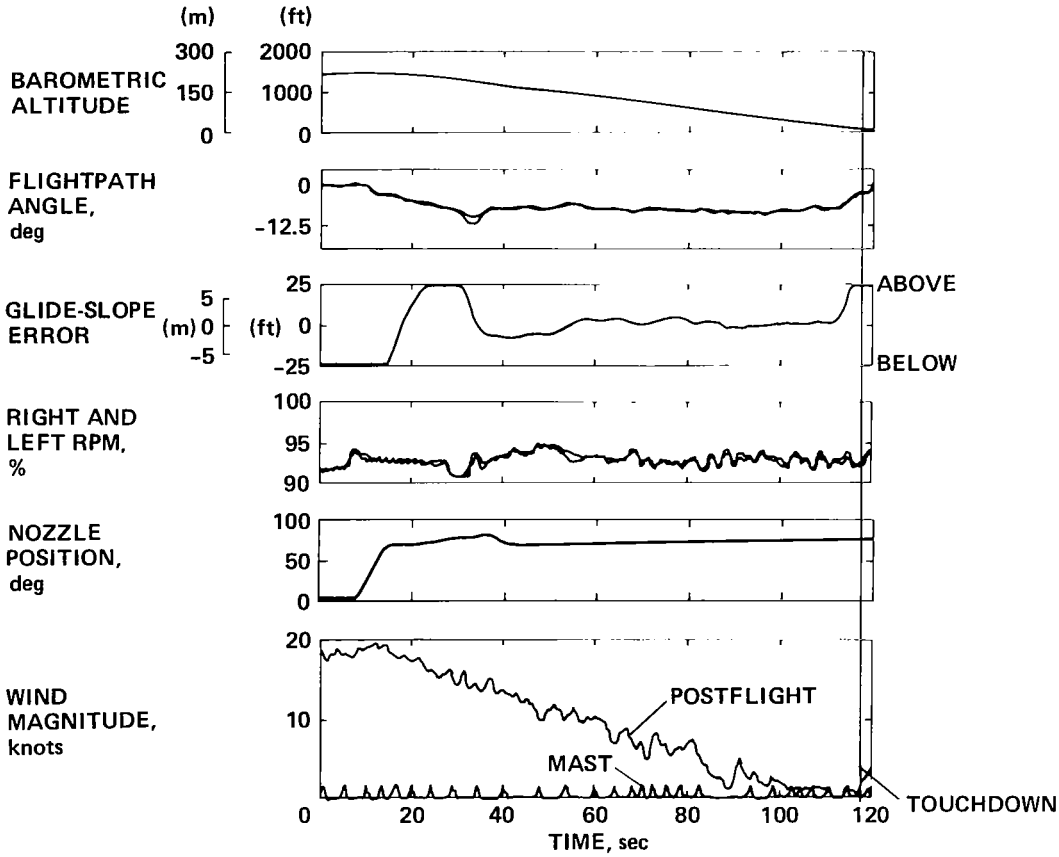

Figure 24(a).– Glide-slope track and flare performance of the two-control system; calm wind, standard day -3°C, $k_{\delta T_c} = 0.75$.

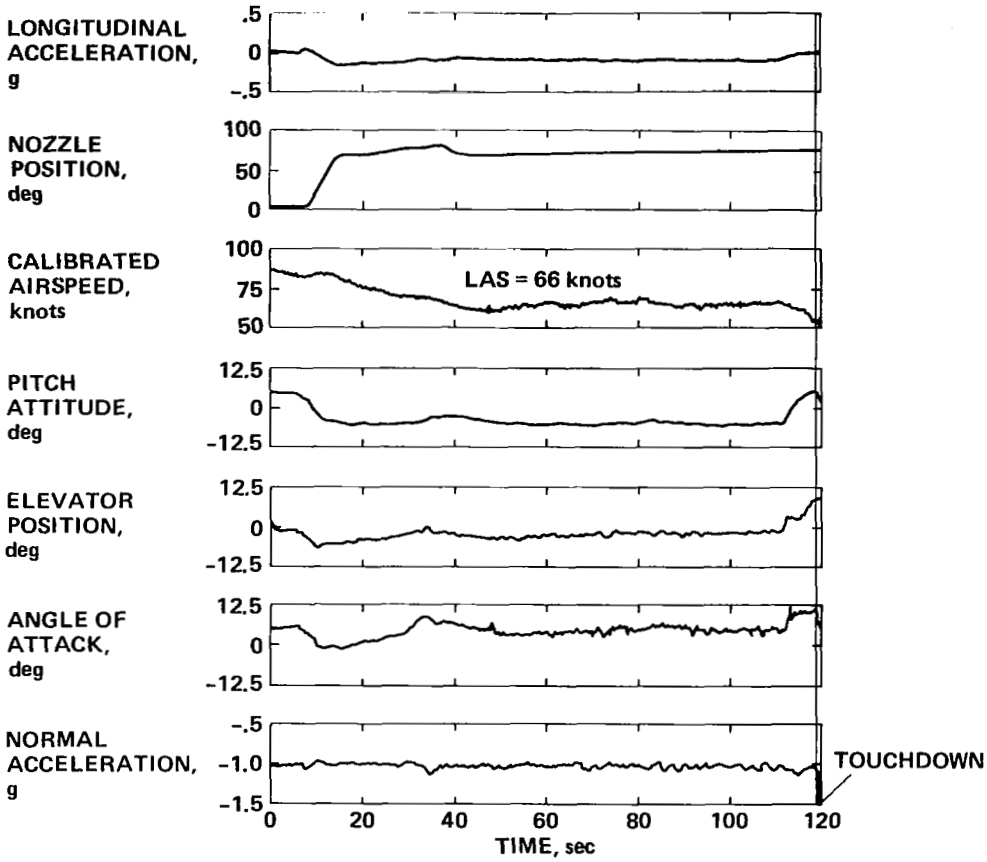

Figure 24(b).-- Glide-slope track and flare performance of the two-control system; calm wind, standard day -3°C, $k_{\delta T_c} = 0.75$.

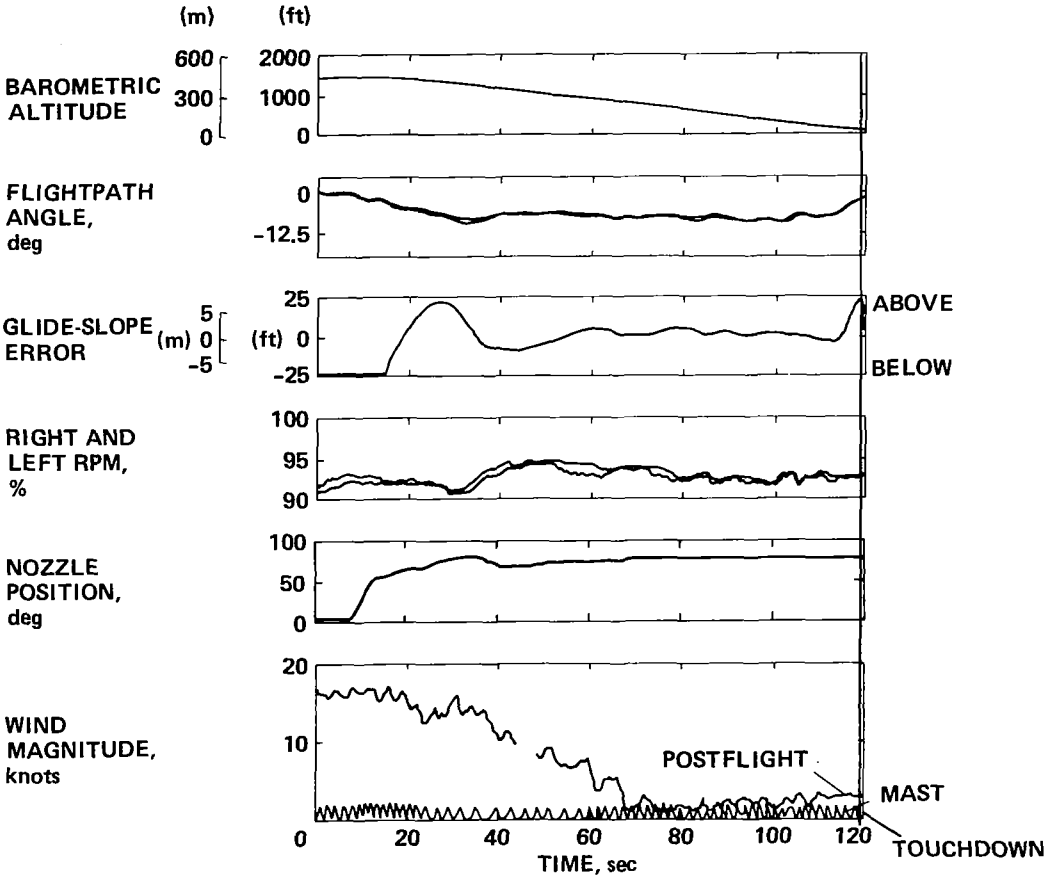

Figure 25(a).– Glide-slope track and flare performance of the two-control system; calm mast wind, standard day -3°C, $k_{\delta T_c} = 0.6$.

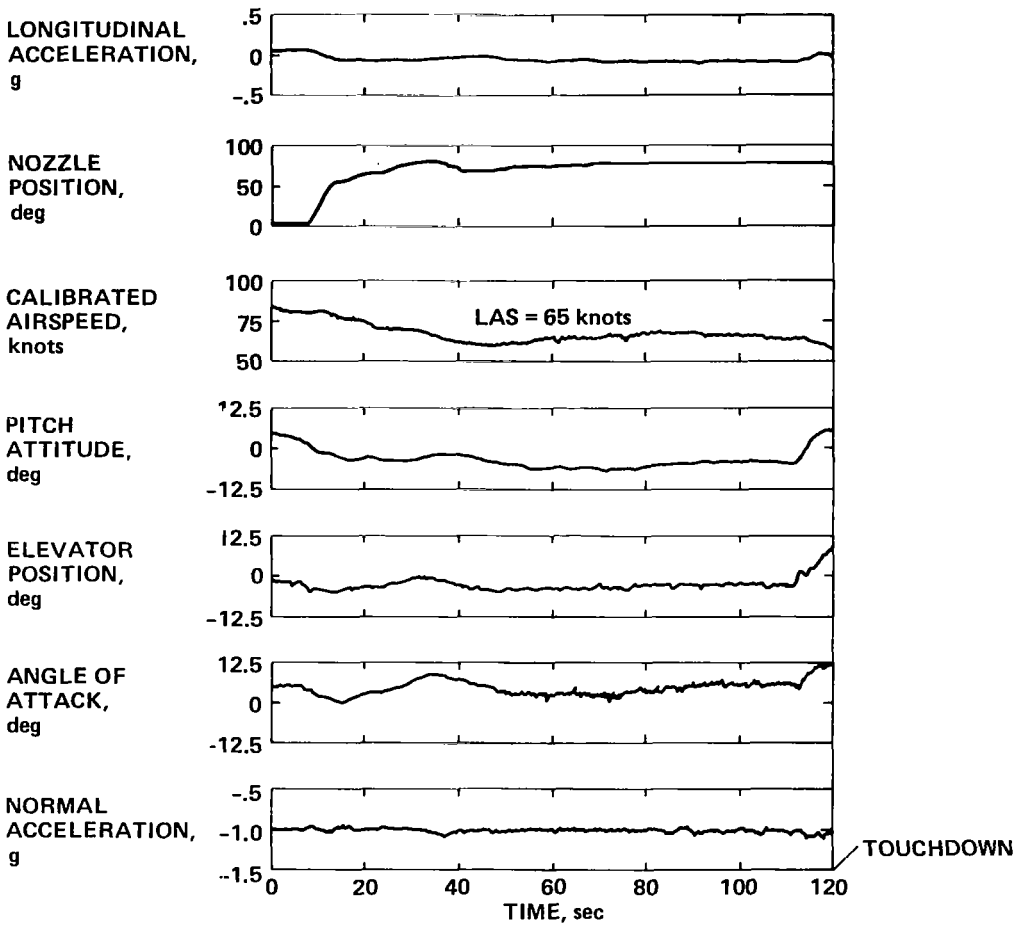

Figure 25(b).– Glide-slope track and flare performance of the two-control system; calm mast wind, standard day -3°C, $k_{\delta T_c} = 0.6$.

contained in reference 23 for ILS glide-slope tracking of the CTOL transport. The significant differences in the performance of the three systems in light winds were in the control activity.

Head Winds– The performance of all three control systems in headwind conditions is documented in figures 26-28; figure 26 for the four-control system, figure 27 for the three-control system, and figure 28 for the two-control system.

Figure 26(a) shows the glide-slope tracking performance for the four-control system operating in winds from 46 to 50 knots at glide-slope capture and decreasing to 30 to 35 knots at touchdown. Considerable choke and rpm activity appears and although the rpm was on the minimum limit of 90% for 5 sec as the airplane descended through 183 m (650 ft), the glide-slope error did not exceed 3 m (9 ft). This error was reduced to zero within 5 sec.

A wind gust occurred at 106 sec into the record that affected the airspeed-tracking performance. The wind speed in figure 26(a) dropped from 43 knots to 31 knots in 7 sec. This gradient can be characterized as either 1.7 knot/sec or 18 knot/30 m (18 knot/100 ft). Figure 26(b) shows that during this period, the airspeed dropped from 3 knots above the 71-knot landing-airspeed reference to 7 knots below the airspeed reference. The nozzles moved aft to increase airspeed and after a 5-sec lag, the airspeed-error-integral term pushed the airplane nose down. Although airspeed varied during the approach, the airplane was speed-stabilized at flare entry. The changing wind speed caused the angle of attack to vary ±2° but did not affect the normal acceleration significantly.

Although there was considerable control activity, with control excursions occasionally reaching limits, the overall glide-slope and speed-tracking performance remained satisfactory.

Figure 27(a) shows the performance of the flight configuration three-control system operating on a hot day in a 10-knot headwind. The turbulence, reported as light, was the

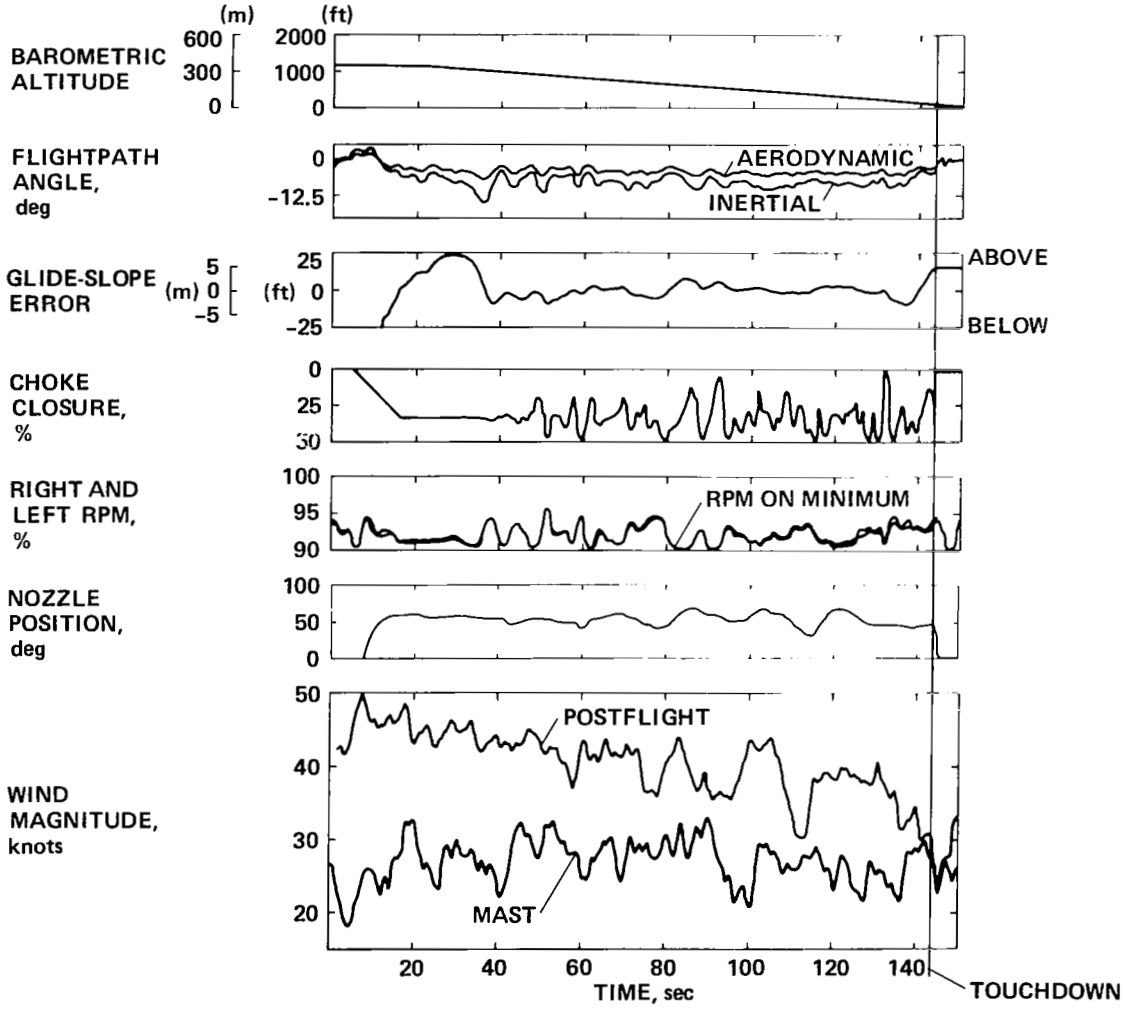

Figure 26(a).– Glide-slope track and flare performance of the four-control system; mast wind was 310° magnetic at 26 knots gusting 30 knots (headwind and left 45° crosswind), standard day -5°C.

result of thermal activity. Only the mast winds were available during this approach. The glide-slope tracking performance and the rpm activity were satisfactory but the choke activity was not. There were extended periods of time when the chokes were on the fully closed limit and other periods when the chokes were fully open in spite of only light turbulence. This tendency of the chokes to saturate resulted from the incorrect throttle gains for the flight configuration three-control system. The airspeed tracking performance in figure 27(b) was good. The pitch activity, the angle-of-attack activity, and the normal-acceleration performance were all satisfactory.

Figure 28(a) shows the performance of the two-control system in a 20- to 25-knot headwind and in turbulence reported as light to moderate. The glide-slope tracking performance was again satisfactory. The nominal rpm was maintained in a good operating range but oscillatory performance did occur several times during the approach. Since no limiting occurred during the approach, the short durations of oscillatory performance were acceptable. Airspeed-tracking performance was good and was maintained without excessive pitch activity. Both the angle of attack and the normal acceleration were satisfactory.

Tailwind– Tailwind situations were not encountered with either the flight configuration three-control system or the two-control system. Figures 29(a) and (b) show the performance of the four-control system operating in a significant tailwind with light turbulence and in near-standard day temperatures. The only unique feature of this approach was its short duration. The performance and control activity were typical of all of the other four-control-system approaches flown in light-wind conditions.

If the guidelines established by the FAA to certify a CTOL transport autoland system which used ILS were directly applied to a STOL airplane flying an MLS approach, the time histories in this section and the flight performance summaries shown in appendix E suggest that all three systems would be regarded as satisfactory even in strong winds.

Many more approaches would be required to fully establish glide-slope track performance but such testing would be prohibitively expensive. An estimate of the low probability event performance can be obtained from high-speed simulation. The results of just such a study are contained in the next section.

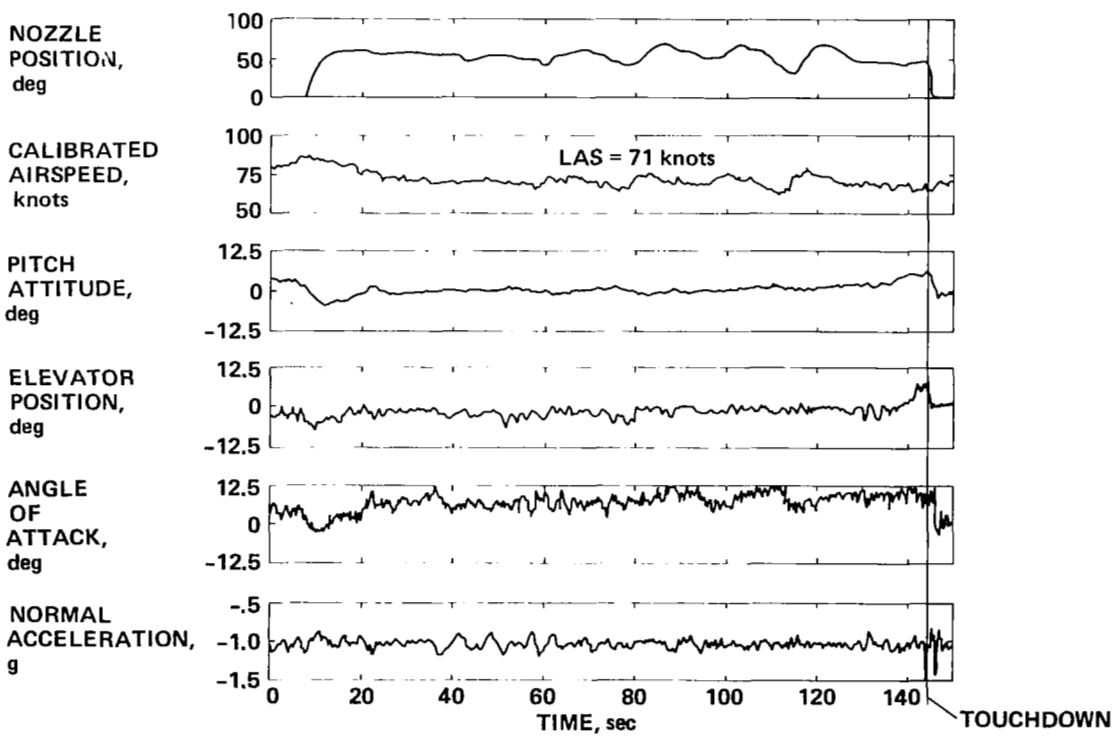

Figure 26(b).– Glide-slope track and flare performance of the four-control system; mast wind was 310° magnetic at 26 knots gusting 30 knots (headwind and left 45° crosswind), standard day -5°C.

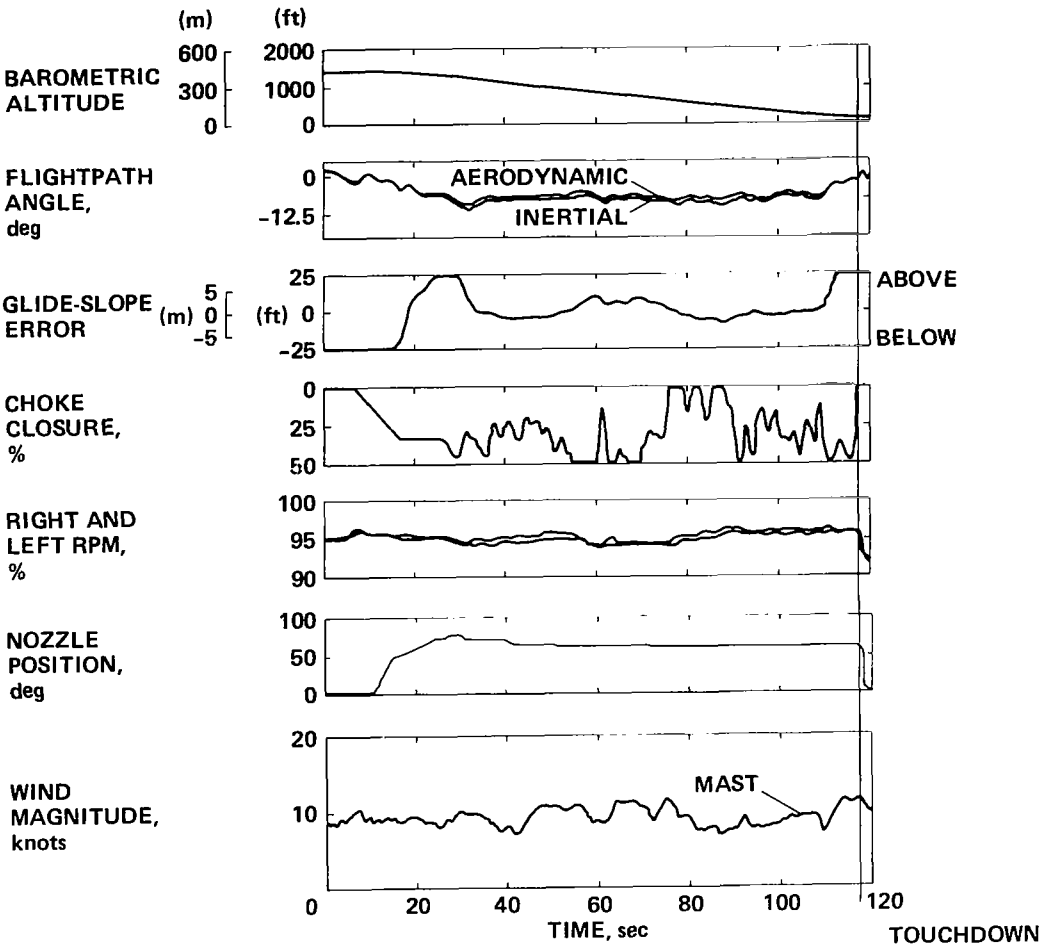

Figure 27(a).– Glide-slope track and flare performance of the flight configuration three-control system; mast wind was 300° magnetic at 12 knots (headwind with left 50° crosswind), standard day +13°C.

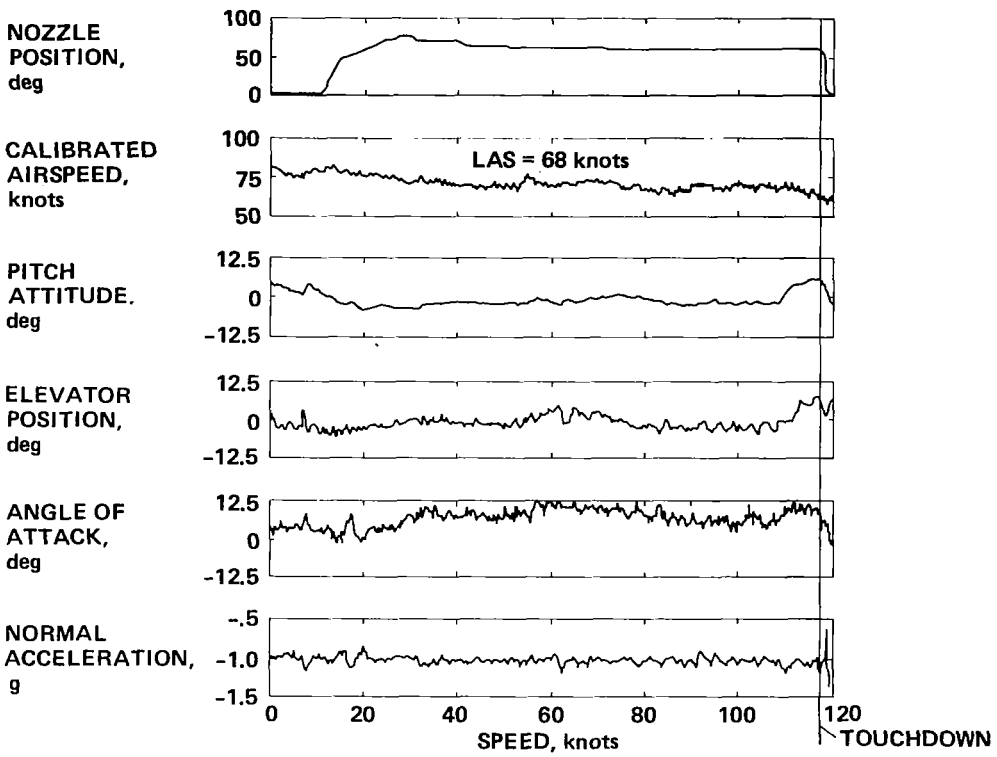

Figure 27(b).– Glide-slope track and flare performance of the flight configuration three-control system; mast wind was 300° magnetic at 12 knots (headwind with left 50° crosswind), standard day +13°C.

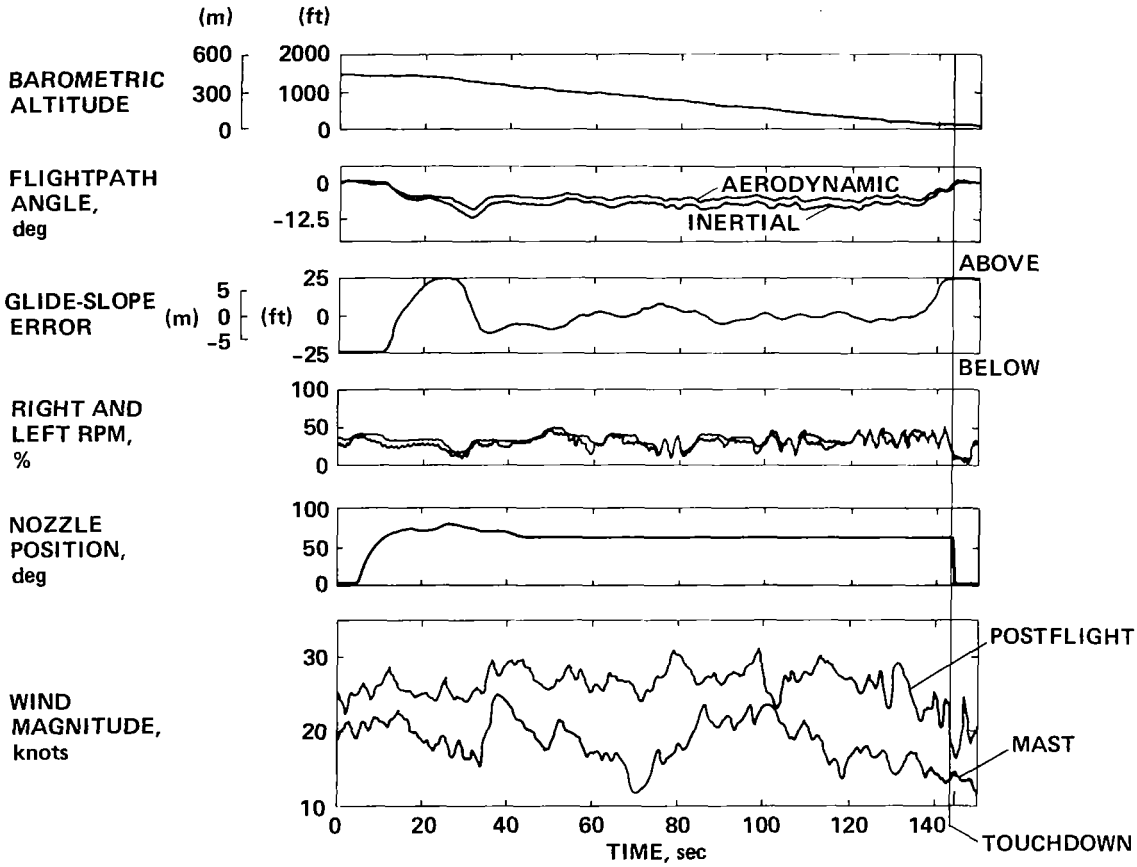

Figure 28(a).– Glide-slope track and flare performance of the two-control system; mast wind was 300° magnetic at 18 knots (headwind and left 50° crosswind), standard day -2°C.

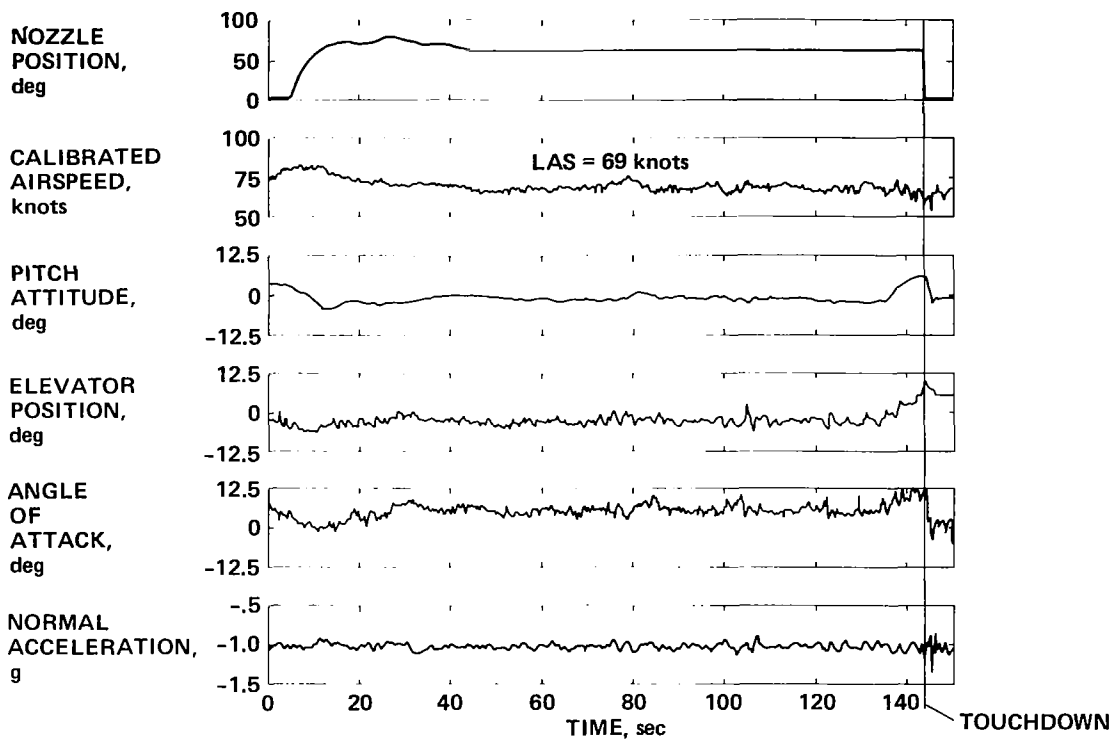

Figure 28(b).– Glide-slope track and flare performance of the two-control system; mast wind was 300° magnetic at 18 knots (headwind and left 50° crosswind), standard day -2°C.

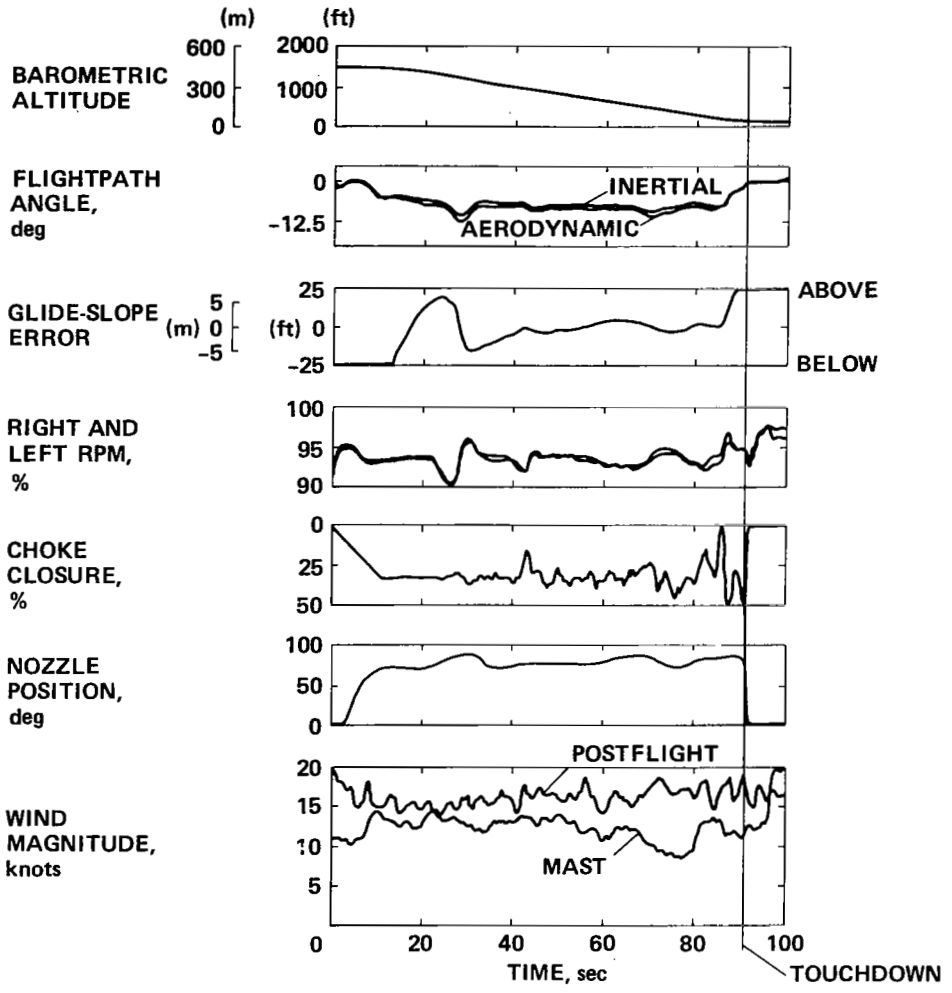

Figure 29(a).– Glide-slope track and flare performance of the four-control system; mast wind was 130° magnetic at 12 knots (tailwind and right 45° crosswind), standard day -3°C.

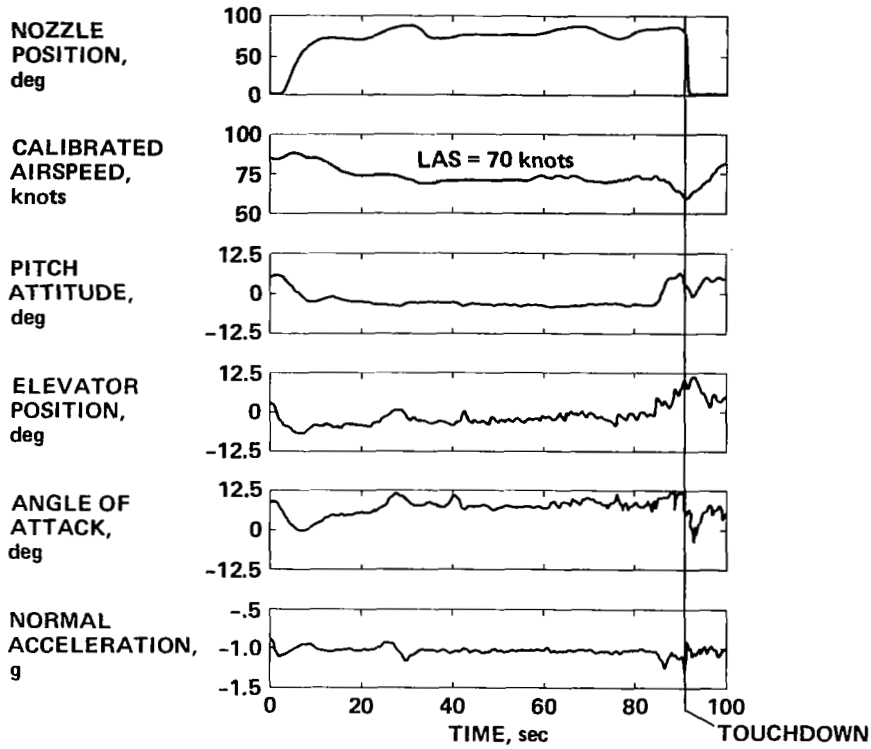

Figure 29(b).– Glide-slope track and flare performance of the four-control system; mast wind was 130° magnetic at 12 knots (tailwind and right 45° crosswind), standard day -3°C.

Statistical Flare-Entry Conditions

The time histories presented in the previous section indicate how the AWJSRA autoland system performed as the airplane descended on the glide slope to 20 m (65 ft). This section summarizes the glide-slope tracking performance just before flare entry as determined from flight tests and high-speed simulation. For purposes of establishing conditions at flare entry, data are compiled for a radio altitude of 30 m (100 ft).

The statistical data presented in this and later sections of this report are in the form of exceedence probability-distribution plots. The data are plotted on graph paper on which a normal probability distribution appears as a straight line. On this type of graph paper a very good control system is represented by a nearly vertical line. A poor control system is represented by a line leaning away from vertical. If the control system is nonlinear due to control limiting the probability curve will consist of two segments – a straight line in the most probable region near the center of the graph and a segment that bends away from the straight line. Both the straight line characteristic and the bending characteristic in the low probability tails of the plot appear in the figures that follow.

Figure 30 shows the glide-slope tracking performance of the four-control system as the airplane descended through 30 m (100 ft). The data points in figure 30 represent 41 approaches flown with the four-control system, and the solid line represents more than 2000 data points compiled from the high-speed simulation described in reference 16. The flight-data points may represent only one approach or may represent multiple approaches which produced the same glide-slope error. Therefore, the 41 approaches are represented by less than 41 points. The ordinate in figure 30 shows the probability that the glide-slope error (Δh_{100}) will exceed the value of the glide-slope error shown on the abscissa ($\Delta h_{100}'$). The glide-slope error is positive when the airplane is above the glide slope. The simulator data in figure 30 show that 97.7% of the time (-2σ), the airplane will be above a point which is 2.8 m (9.5 ft) below the 7.5° glide slope. Approximately 2.3% of the time ($+2\sigma$), the airplane will be above a point which is 3.8 m (12.5 ft) above the glide slope. The 2σ distribution is the difference between the $+2\sigma$ and -2σ values which in this case is 6.7 m (22.0 ft). Figure 30 also shows that the mean of the simulator data was 0.6 m (2 ft) above the 7.5° glide slope.

The flight test data provided a good estimate of the mean value and the 1σ (standard deviation) performance of the glide-slope track system, a poorer estimate of the 2σ performance, and no estimate at all of the low-probability performance. The low-probability performance was estimated using the high-speed simulation to generate the large data base. Figure 30 shows considerably smaller spread in the 2σ flight-test data than in the simulation data. There are two reasons for this. First, the wind disturbances encountered in flight were generally smaller than the limiting wind disturbances derived from the FAA wind model specified in AC 20-57A (ref. 22), which were used in the simulation. Second, the flight-test data sample is very small compared to the data base generated in the simulator.

As noted in the section on current autoland practice, AC 120-28B (ref. 23) requires that for an ILS Category IIIa automatic approach, the airplane must be within ±35 μA (2σ) or ±3.7 m (12 ft) of the glide slope as it descends from 213 m (700 ft) to the flare height. At 30-m (100-ft) height above the touchdown zone, the ±3.7-m (12-ft) requirement is applicable. Figure 30 shows this requirement in the form of the crosshatched 2σ boundaries. The four-control system essentially meets the FAA requirement for the flight and simulation cases.

Figure 31 shows data from 29 approaches with the flight configuration three-control system as well as data from the simulator for both configurations of the three-control system. Again, the probability spread for the flight data is less than for the simulator data and this difference reflects the light winds encountered in flight and the moderate winds modeled in the simulator. The simulator shows that performance for the flight configuration three-control system is deteriorated for the low probabilities beyond 2σ. This deterioration is caused by the saturation of the chokes which occurred when the flight configuration three-control system encountered large disturbances. For the design configuration three-control system, choke saturation was significantly reduced and provided better performance in the presence of the large disturbances.

Figure 32 shows the glide-slope tracking performance of the two-control system. The flight-test data for 26 approaches show better agreement with the simulator data than was seen for the four- and three-control systems. An explanation for this agreement is that more random winds were encountered for the two-control system than for the other systems. In the summary of the glide-slope error data presented in figure E2 of appendix E, it is noted that the last six approaches were flown in wind-shear situations resulting in late stabilization on the glide slope. The glide-slope error data for the last six two-control approaches are noted in figure 32. The lowest glide-slope error data points correspond to late stabilization on the glide slope.

The 30-m (100-ft) glide-slope track data from figures 30–32 are summarized in table 2. The flight-test data showed less tracking error for all of the control systems than was determined from the high-speed simulation data. Because the winds during the flight testing were less severe than those of the high-speed simulation model, only the simulation data are useful for determining the ultimate performance of the control systems.

All of the control systems were capable of meeting the glide-slope track requirements like those that are imposed by the FAA on CTOL transport autoland systems for Category IIIa operations with ILS.

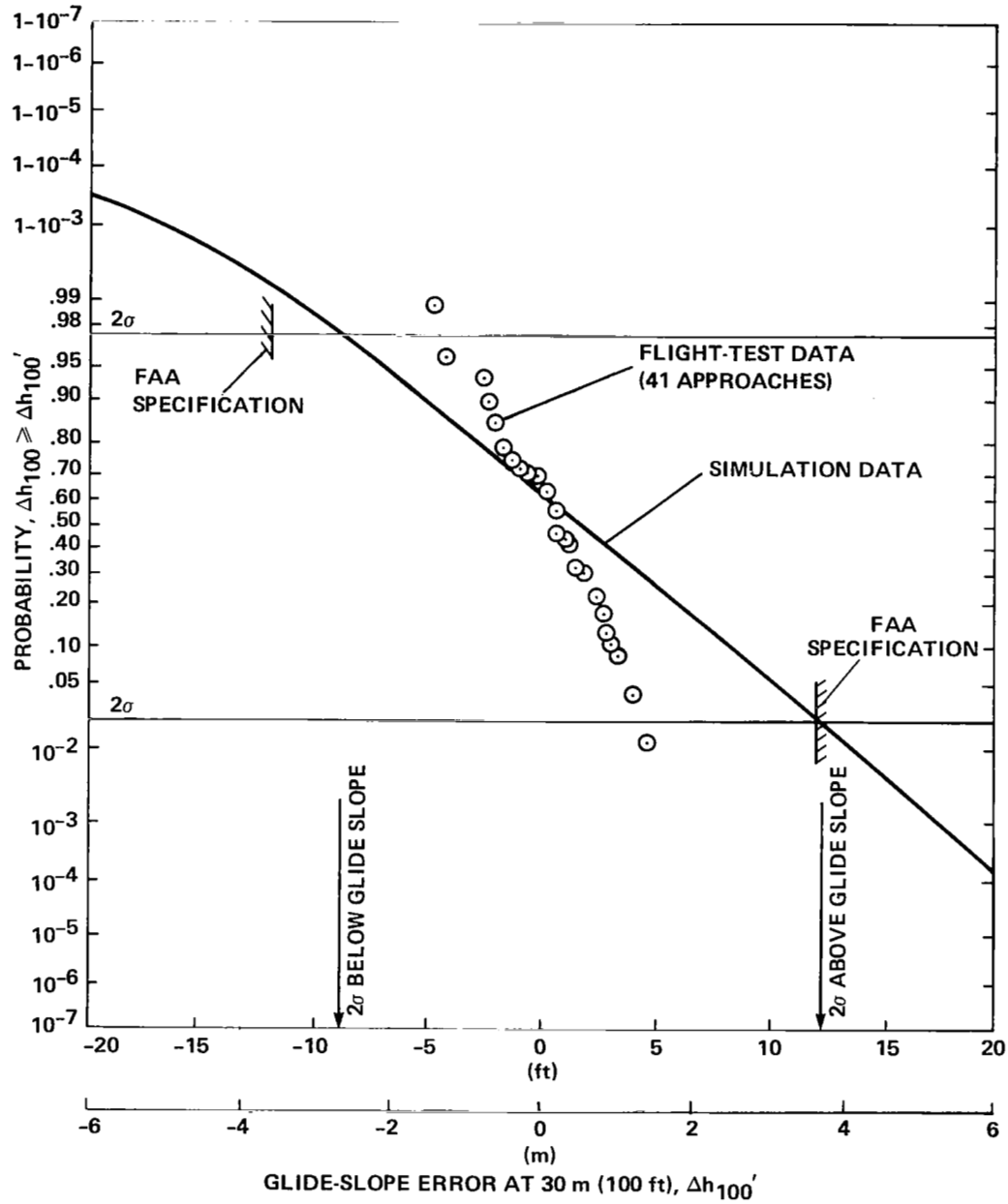

Figure 30.– Four-control system glide-slope tracking performance as the airplane descended through 30 m (100 ft).

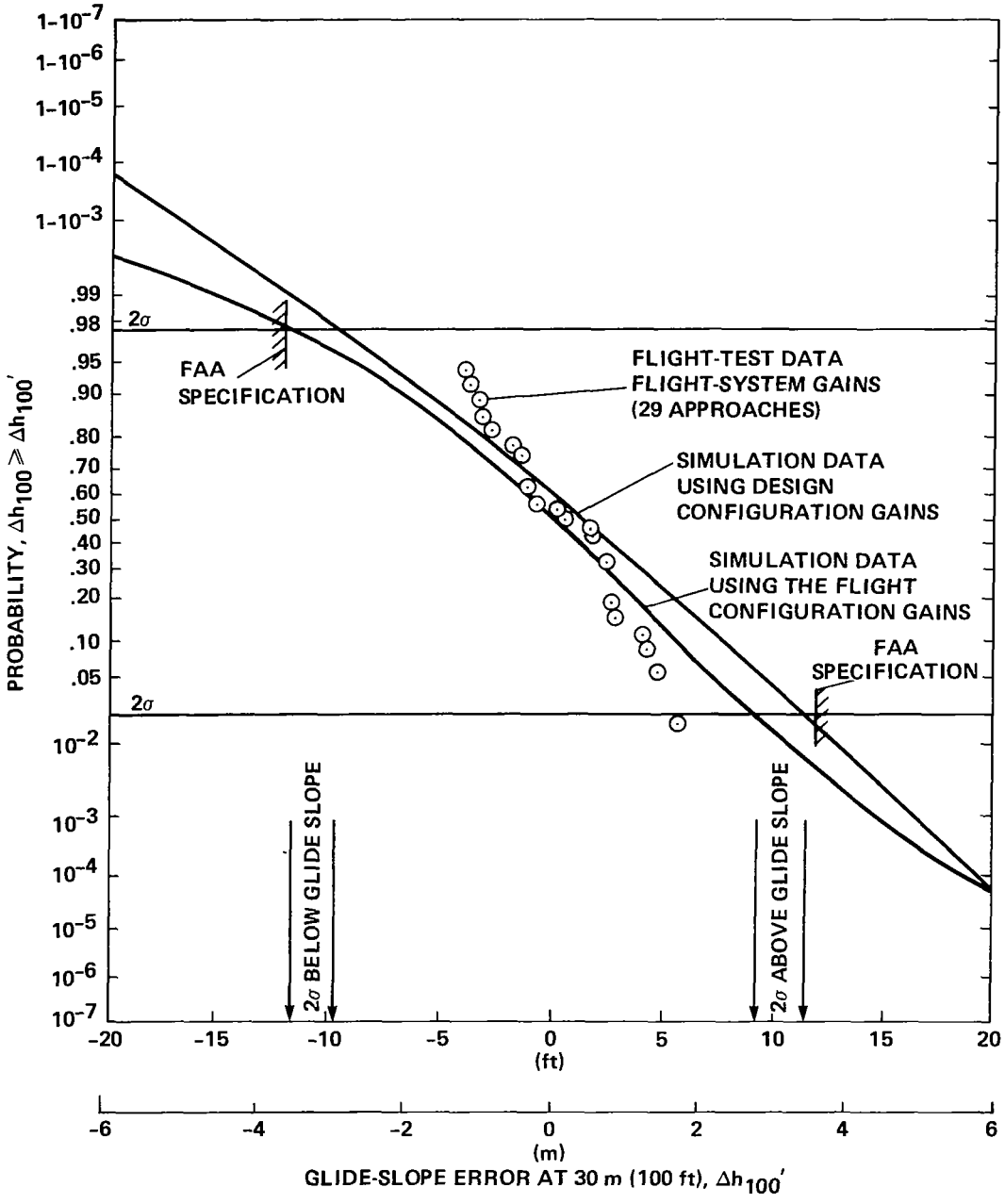

Figure 31.– Three-control system glide-slope tracking performance as the airplane descended through 30 m (100 ft).

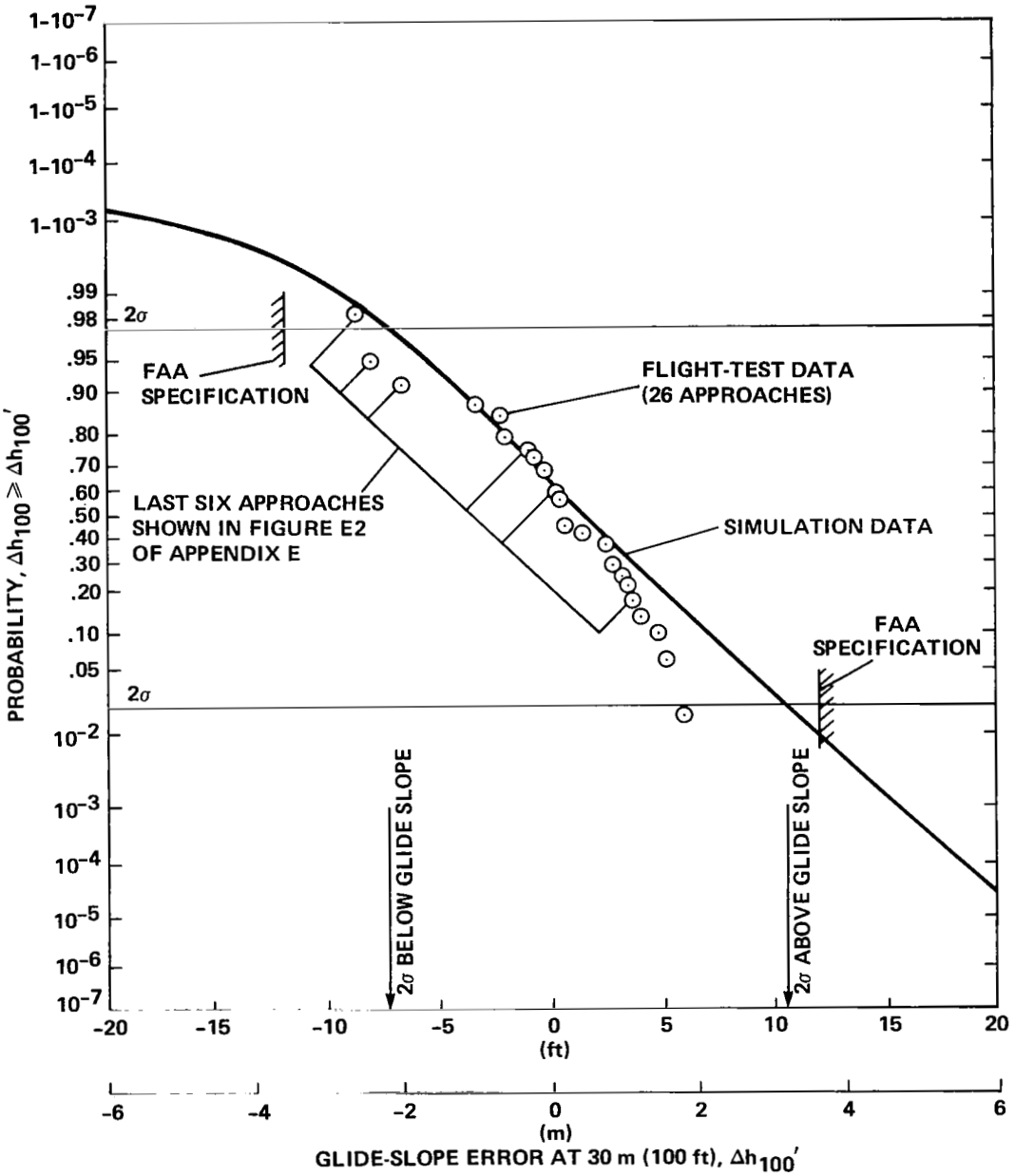

Figure 32.– Two-control system glide-slope tracking performance as the airplane descended through 30 m (100 ft).

TABLE 2.– SUMMARY OF GLIDE-SLOPE ERROR PERFORMANCE AT 30 m (100 ft)

Glide-slope error	Four controls		Three controls			Two controls	
	Flight, m (ft)	Simulation, m (ft)	Flight, m (ft)	Simulation configuration		Flight, m (ft)	Simulation, m (ft)
				Flight, m (ft)	Design, m (ft)		
Number of data points	41	>2000	29	>2000	>2000	26	>2000
2σ above glide slope	1.37 (4.5)	3.81 (12.5)	1.68 (5.5)	2.83 (9.3)	3.51 (11.5)	1.68 (5.5)	3.20 (10.5)
Mean	.24 (.8)	.46 (1.5)	.15 (.5)	.08 (.25)	.46 (1.5)	.15 (.5)	.55 (1.8)
2σ below glide slope	-1.28 (-4.2)	-2.89 (-9.5)	1.46 (-4.8)	-3.51 (-11.5)	-2.98 (-9.8)	-2.59 (-8.5)	-2.13 (-7.0)
2σ dispersion	2.65 (8.7)	6.70 (22.0)	3.14 (10.3)	6.34 (20.8)	6.49 (21.3)	4.27 (14.0)	5.33 (17.5)

The airspeed error performance of all three control systems was recorded during the autoland flight tests. A summary of the airspeed error data is contained in figure E5 of appendix E but comparable high-speed simulation data are not available. Figure E5 shows that all three systems held the speed error to less than ±5 knots, thus speed performance was generally satisfactory. In the absence of simulation data, it is not possible to determine whether the apparent superior speed-tracking performance of the four- and three-control system designs is attributable to differences in the control system designs or to different wind conditions.

Flare Performance

This section presents the time histories of the flare and altitude-altitude rate profiles that correspond to the time histories of the glide-slope track and flare discussed in the previous section. The data are presented for calm wind conditions, headwinds, and tailwinds.

Calm Winds– Figure 33 shows the expanded time history of the flare for the four-control system approach shown in figure 22. The first event in the flare maneuver was the pitch command as a function of altitude which began at 20 m (65 ft). Figure 33 shows that the elevator responded rapidly, within 0.1 sec of flare initiation and that the subsequent pitch response followed 1 sec later. The pitch maneuver initiated the reduction of the altitude rate, rotated the airplane nose up so the touchdown would be on the main landing gear first and caused the airplane to decelerate to reduce the aerodynamic lift and the landing-rollout braking requirements. Figure 33 shows that as the airspeed decreased, additional elevator was required to maintain the high pitch attitude of the nose. The airspeed dropped 11 knots during the flare maneuver. The deceleration-speed schedule (fig. 16) provided a touchdown-target speed of 61.5 knots. The nozzle angle increased 5° to help bleed off the airspeed. Beginning at 15 m (50 ft) radio altitude, the throttle and chokes were commanded to reduce the altitude rate according to the altitude-altitude rate profile described in figure 18. The goal of this schedule was to reduce the altitude rate from the value needed to maintain the 7.5° MLS glide slope to a touchdown-target value of -0.95 m/sec (-3.12 ft/sec). Figure 33 shows that the chokes began to move to reduce the altitude rate within 0.1 sec of the airplane passing through 15 m (50 ft). The rpm responded after approximately 1 sec. A change in the altitude rate was evident 0.5 sec after the airplane descended through 15 m (50 ft). The altitude rate rapidly changed from -4.27 m/sec (-14 ft/sec) to -1.5 m/sec (-5 ft/sec) during the next 4 sec and stabilized thereafter at -1.37 m/sec (-4.5 ft/sec) until the touchdown.

Another view of the behavior of the airplane during the flare maneuver is provided by figure 34 which shows the altitude-altitude rate profile corresponding to the time histories in figure 33. Figure 34 shows that the airplane descended 3 m (10 ft) below the planned altitude-altitude rate profile before responding to the control inputs. The initial altitude rate adjustment caused the airplane to go above the reference profile. The airplane returned to the reference profile at a radio altitude of 1.5 m (5 ft). During the final 1.5 m (5 ft) before touchdown, the airplane dropped below the reference profile and held a nearly constant sink rate of 1.3 m/sec (4.3 ft/sec) to touchdown. Figure 33 shows that the chokes were moving to provide additional lift to return the airplane to the reference profile but the airplane had not yet responded by the time touchdown occurred.

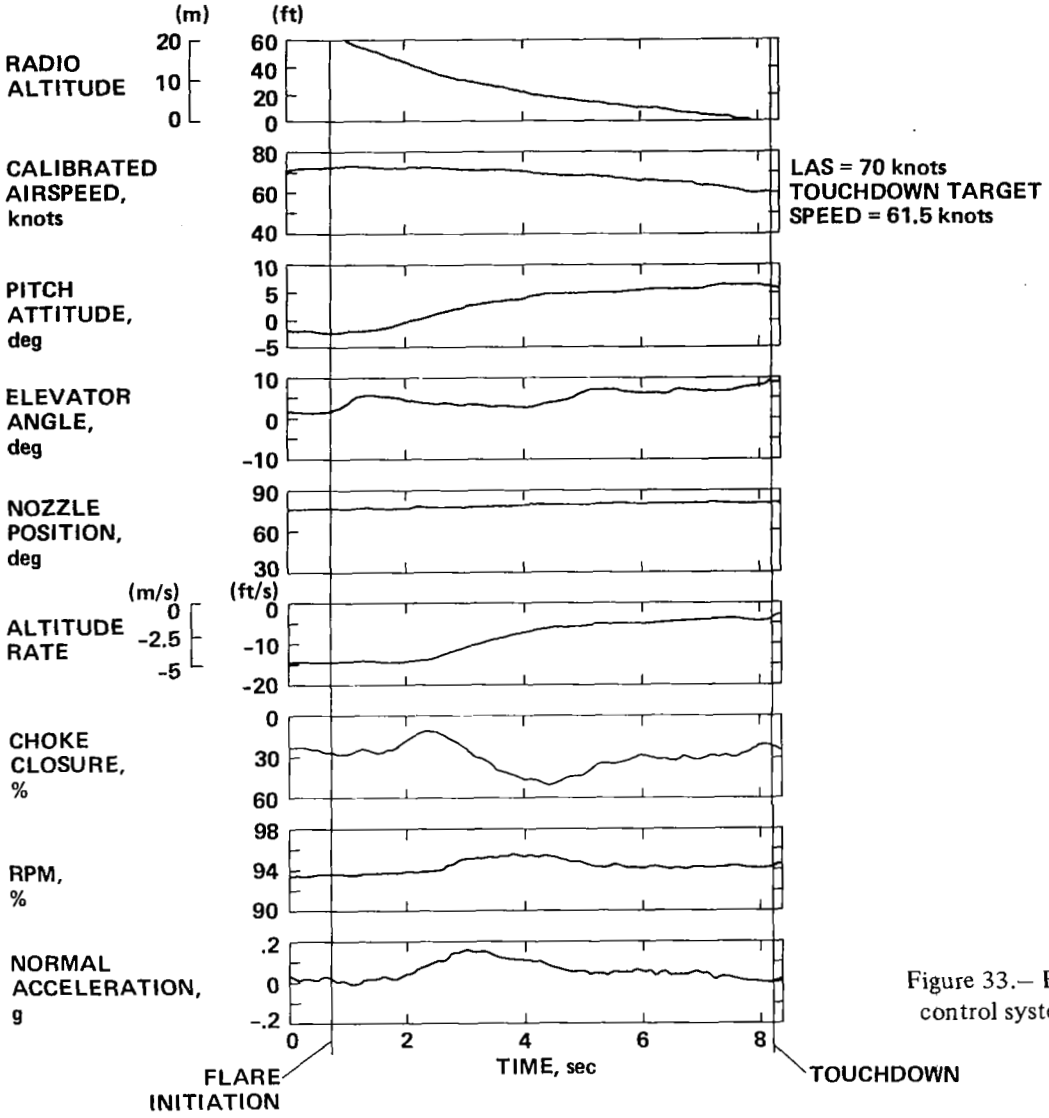

Figure 33.– Flare time history for the four-control system; calm wind, standard day.

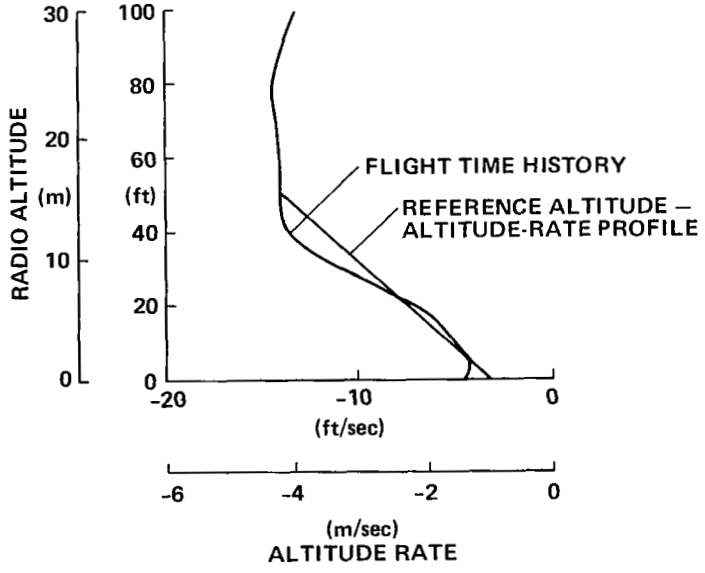

Figure 34.– Altitude vs altitude rate for the four-control system; calm wind, standard day.

Figure 35 presents the expanded flare time history for the flight configuration three-control system that corresponds to the glide-slope track and flare time history shown in figures 23(a) and (b). Recall that the flight configuration three-control system was similar to the four-control system for the flare except that the nozzles were not used for speed control and the throttle feedback and rpm to choke gains were reduced. Figure 35 indicates that the pitch maneuver for the flight configuration three-control system was similar to the pitch maneuver for the four-control system. The speed reduction during this flare maneuver was 7 knots. Nozzles remained fixed at an indicated 60° throughout the maneuver. Figure 35 shows that regulation of the altitude rate was accomplished entirely with the chokes. The rpm remained constant because of the low throttle gain used for this configuration.

Figure 36 indicates that the pitch-flare maneuver, which began at the flare-initiate altitude of 20 m (65 ft), was effective in establishing the airplane on the altitude-altitude rate profile and that the airplane closely tracked the profile to touchdown.

Figure 37 presents the expanded flare time history for the two-control system that corresponds to the glide-slope track and flare time history shown in figures 25(a) and (b). Figure 37 indicates that the speed bleedoff, in this case 6 knots, and the altitude rate arrestment were accomplished through the pitch maneuver since the rpm remained essentially constant.

Figure 38 shows that the altitude rate dropped below and then asymptotically closed on the altitude-altitude rate profile to produce a landing near the target-touchdown sink rate of -0.95 m/sec (-3.12 ft/sec).

This review of the selected time histories and altitude-altitude rate profiles, shown for the three systems operating in calm winds, suggests that the choke control may not have been needed for accomplishing the flare maneuver. Indeed, the time history for the four-control system (fig. 33) even seems to suggest that the attempt to aggressively control the altitude rate may have adversely excited the rpm. It is necessary to evaluate the performance in stronger wind-disturbance conditions to determine the benefits of the four-control system versus the other control systems.

Headwind– Figure 39 shows a flare time history for the four-control system in a strong, gusty-wind condition. This figure corresponds to the glide-slope track and flare time histories shown in figures 26(a) and (b). Only the portion of the flare maneuver below 15 m (48 ft) is presented in figure 39 because the flare duration in the strong winds exceeded 10 sec. The flare maneuver began with the pitch input at 20 m (65 ft). The full maneuver is shown in figure 26 and is partially complete by the time the record in figure 39 begins. Subsequently, the elevator deflection increased to hold the nose up as the flare progressed. The airspeed remained relatively constant. The time history leading into the flare (fig. 26) indicates that as the airplane descended through 20 m (65 ft), the airspeed was 3 knots below the 71-knot LAS reference. Recall that the nozzles were driven by two commands: a deceleration command and a speed error command. In the absence of wind, the nozzle command was essentially nulled. The situation was different in figure 39. During the flare, the speed error was greater than the deceleration command and that caused the nozzles to rotate aft to an angle less than 45°. At 6 m (20 ft), the 45° nozzle limit included in figure 16 caused the average nozzle angle to increase to 45°. As soon as the 45° limit was imposed, the speed decreased 4 knots as indicated in figure 39.

Figure 40 presents the altitude-altitude rate profile corresponding to the flare time history shown in figure 39. The most obvious feature of figure 40 is the random-appearing altitude rate as the airplane descended. In one sense, there was less demand placed on the control system to accomplish the flare maneuver because the strong headwind caused the altitude rate to be only about 3 m/sec (10 ft/sec) as the airplane descended on the 7.5° MLS glide slope. The incremental change in altitude rate required to acquire the target-touchdown sink rate was less than it would have been if the wind were calm. On the other hand, the strong wind and turbulence placed heavy demands on the control system to restore the airplane to the glide-slope reference before the flare maneuver began and to the altitude-altitude rate profile after the flare maneuver began. The airplane tended to ride through the gusts with the control system unable to hold the altitude rate errors to less than ±0.6 m/sec (±2 ft/sec). Figure 40 indicates that the altitude rate gradually tapered from 1.7 m/sec (5.5 ft/sec) to zero as the airplane descended through the last 0.6 m (2 ft) of radio altitude. This behavior in the altitude rate was the result of the wing-down landing associated with the forward-slip maneuver used to counter the 45° left crosswing. The left landing-gear wheel touched down first as shown in figure 40. Then the airplane rolled to the right for 0.5 sec until the right main-landing-gear wheel touched down very softly. The radio altimeter recorded the altitude change of the aircraft centerline throughout the landing as the right wheel settled to the runway.

Figure 41 presents the expanded flare time history for the flight configuration three-control system corresponding to the glide-slope track and flare-time history in figures 27(a) and (b). Figure 41 shows that the airspeed at flare entry was near 69 knots, close to the landing-airspeed reference. Following the usual pitch-up flare maneuver, the airspeed dropped to 62 knots at touchdown. Nozzle position remained constant throughout the flare. The rpm in figure 41 remained essentially constant because of the low-throttle feedback and rpm-to-choke gains used for the flight configuration three-control system. The burden of closed-loop control of the altitude rate change required for the flare was on the chokes alone. The altitude rate trace in figure 41 shows that a two-segment flare maneuver occurred.

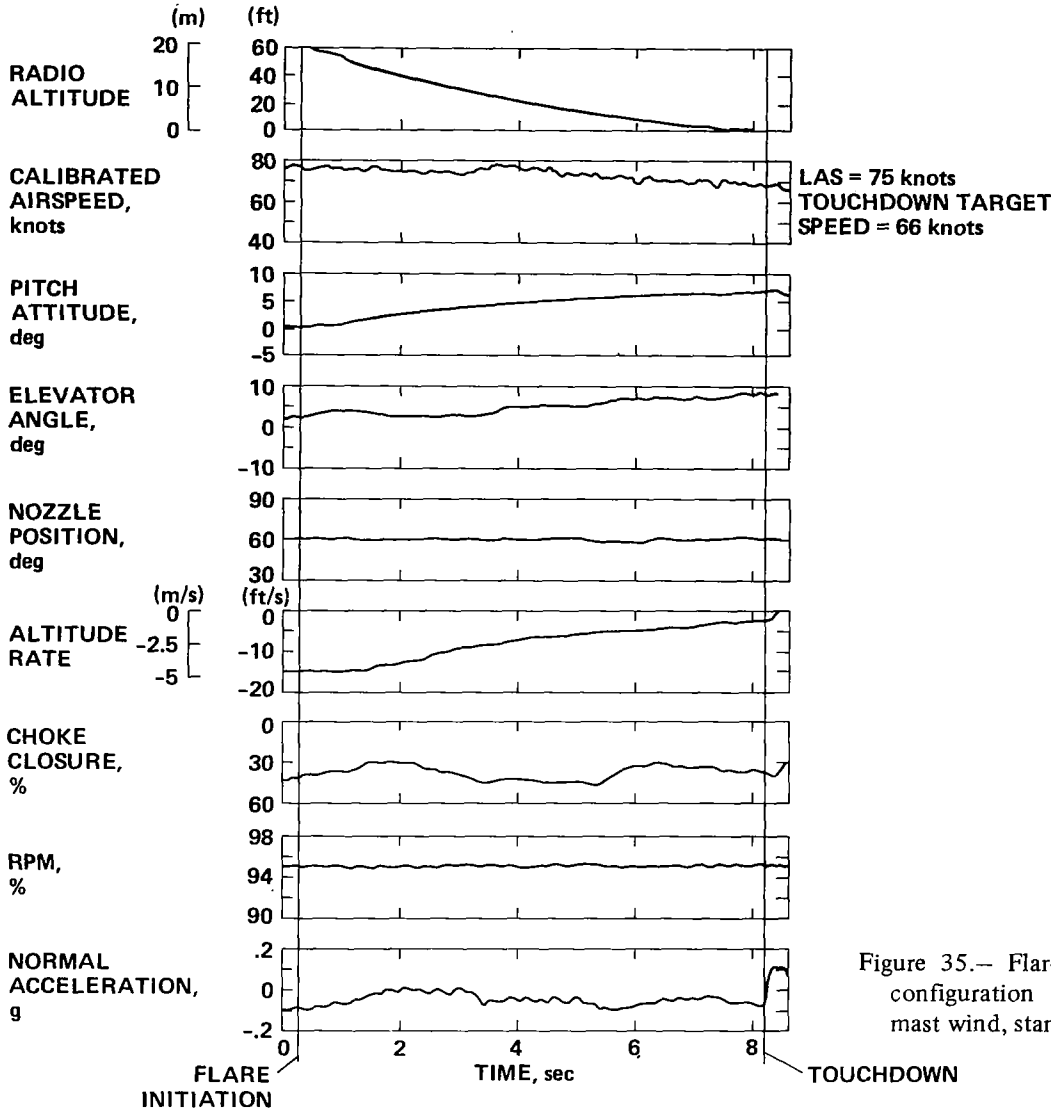

Figure 35.– Flare time history for the flight configuration three-control system; calm mast wind, standard day + 17°C.

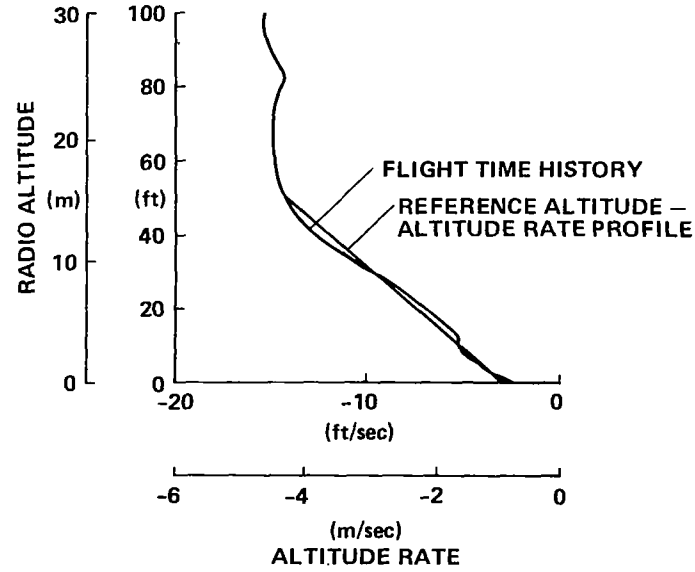

Figure 36.– Altitude vs altitude rate for the flight configuration three-control system; calm wind, standard day + 17°C.

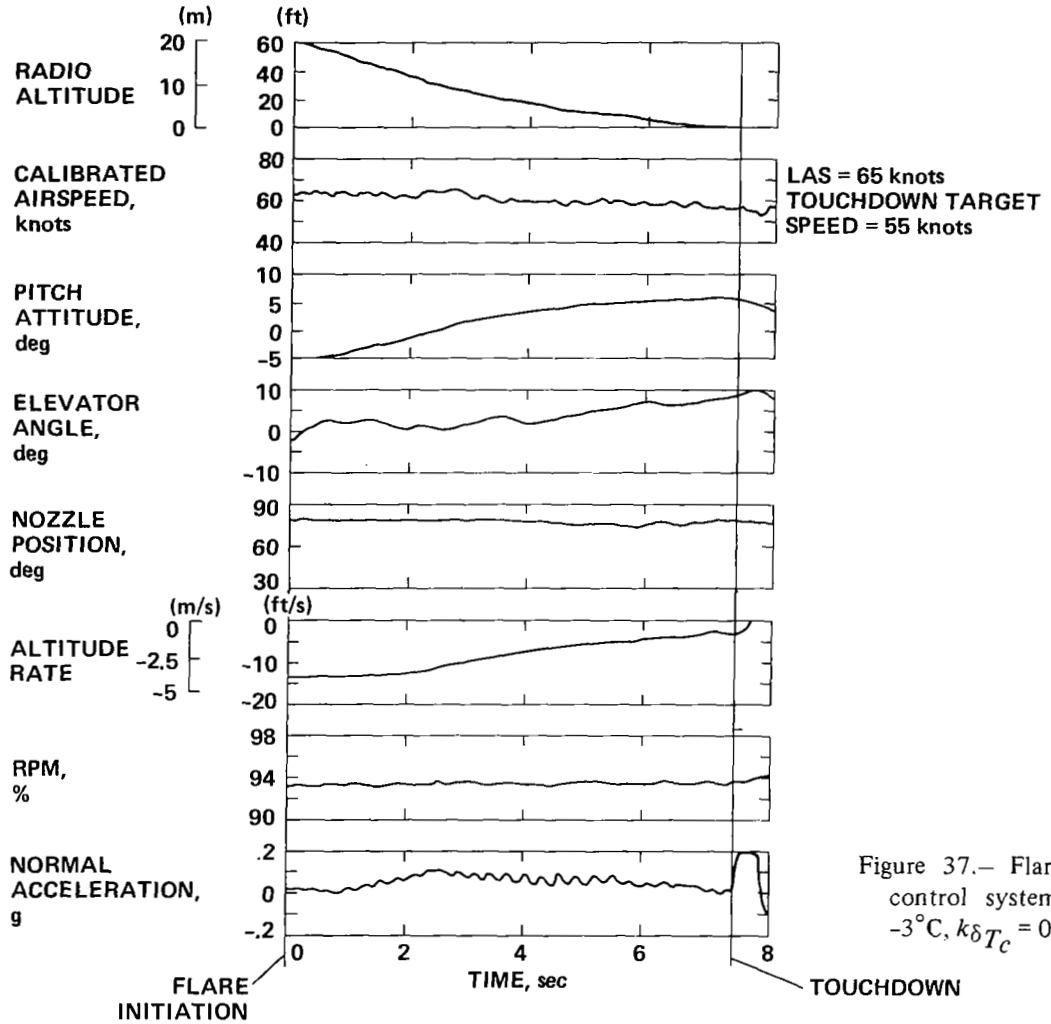

Figure 37.– Flare time history for the two-control system; calm wind, standard day -3°C, $k_{\delta T_c} = 0.6$.

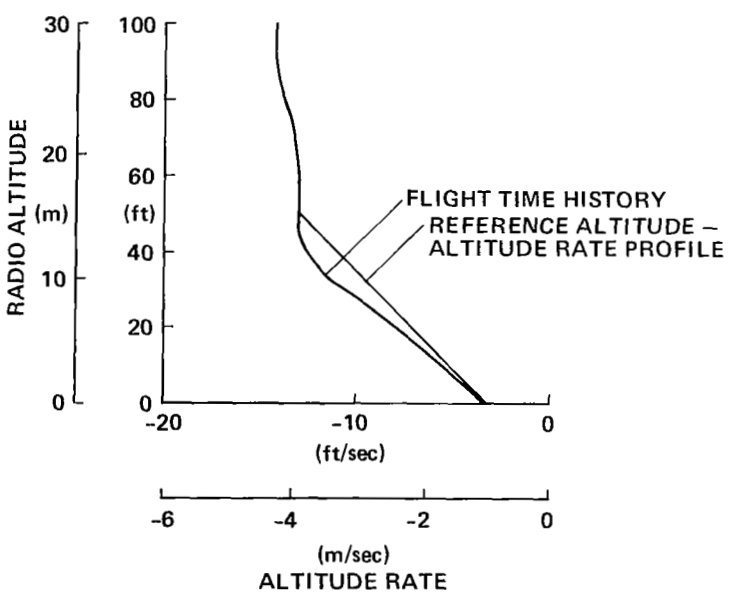

Figure 38.– Altitude vs altitude rate for the two-control system; calm wind, standard day -3°C, $k_{\delta T_c} = 0.6$.

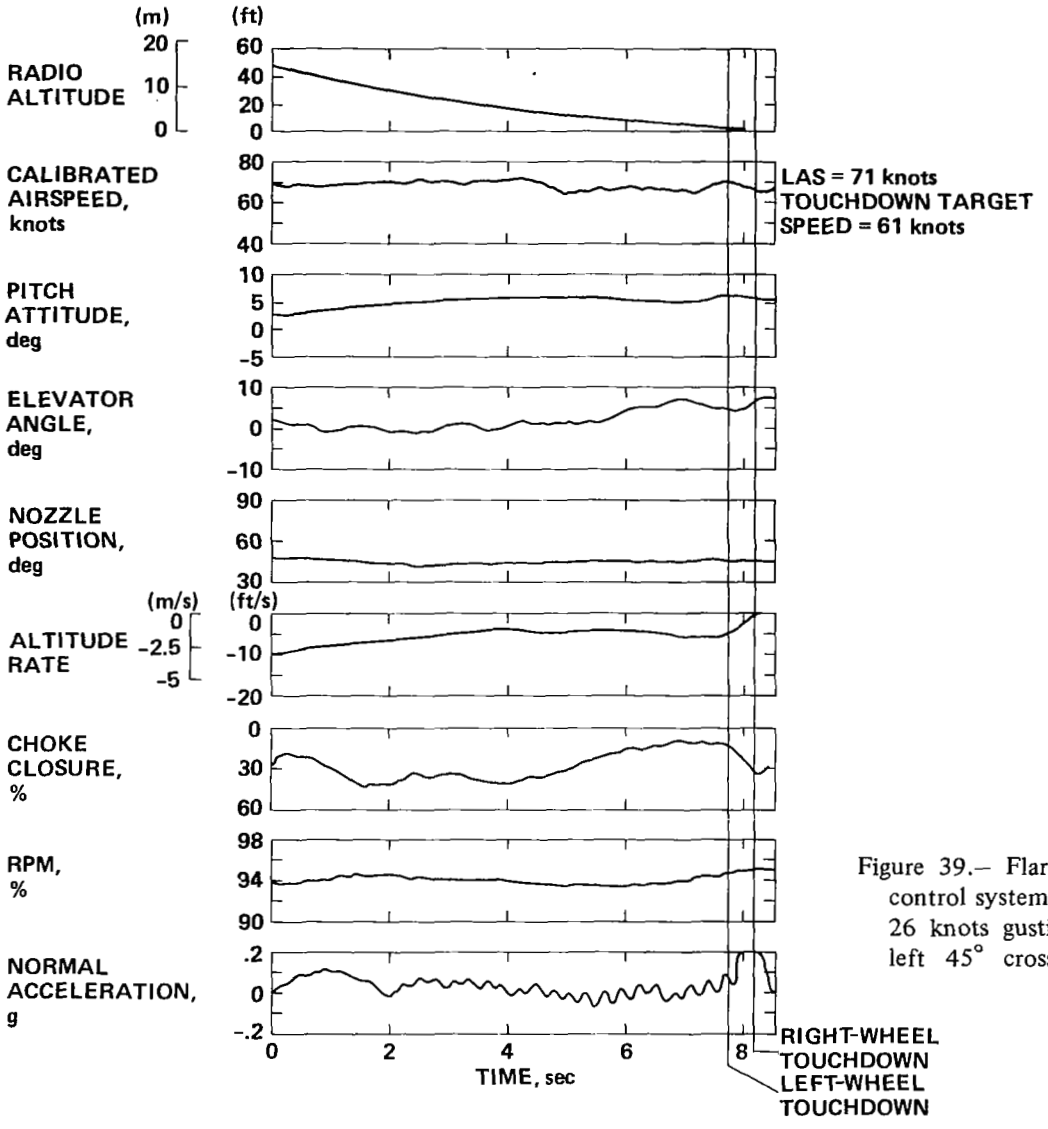

Figure 39.– Flare time history for the four-control system; mast wind at 310° magnetic, 26 knots gusting 30 knots (headwind and left 45° crosswind), standard day -5°C.

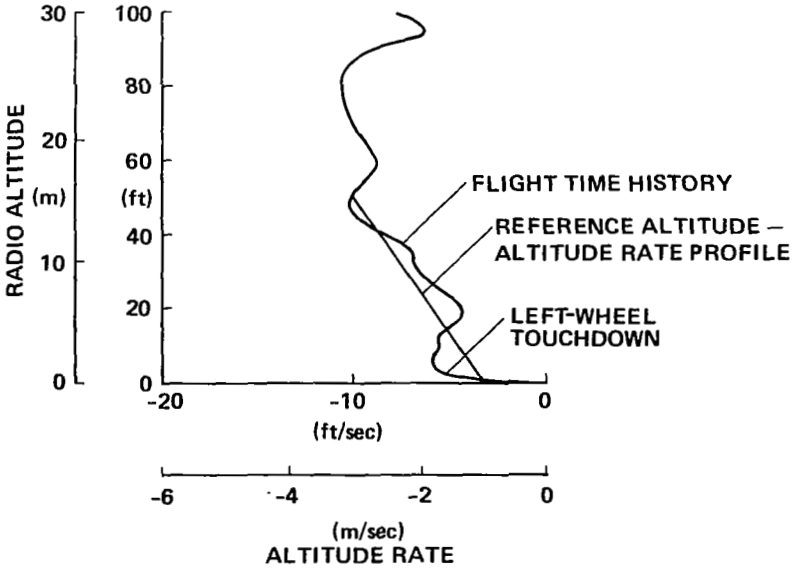

Figure 40.– Altitude vs altitude rate for the four-control system; mast wind at 310° magnetic, 26 knots, gusting 30 knots (headwind and left 45° crosswind), standard day -5°C.

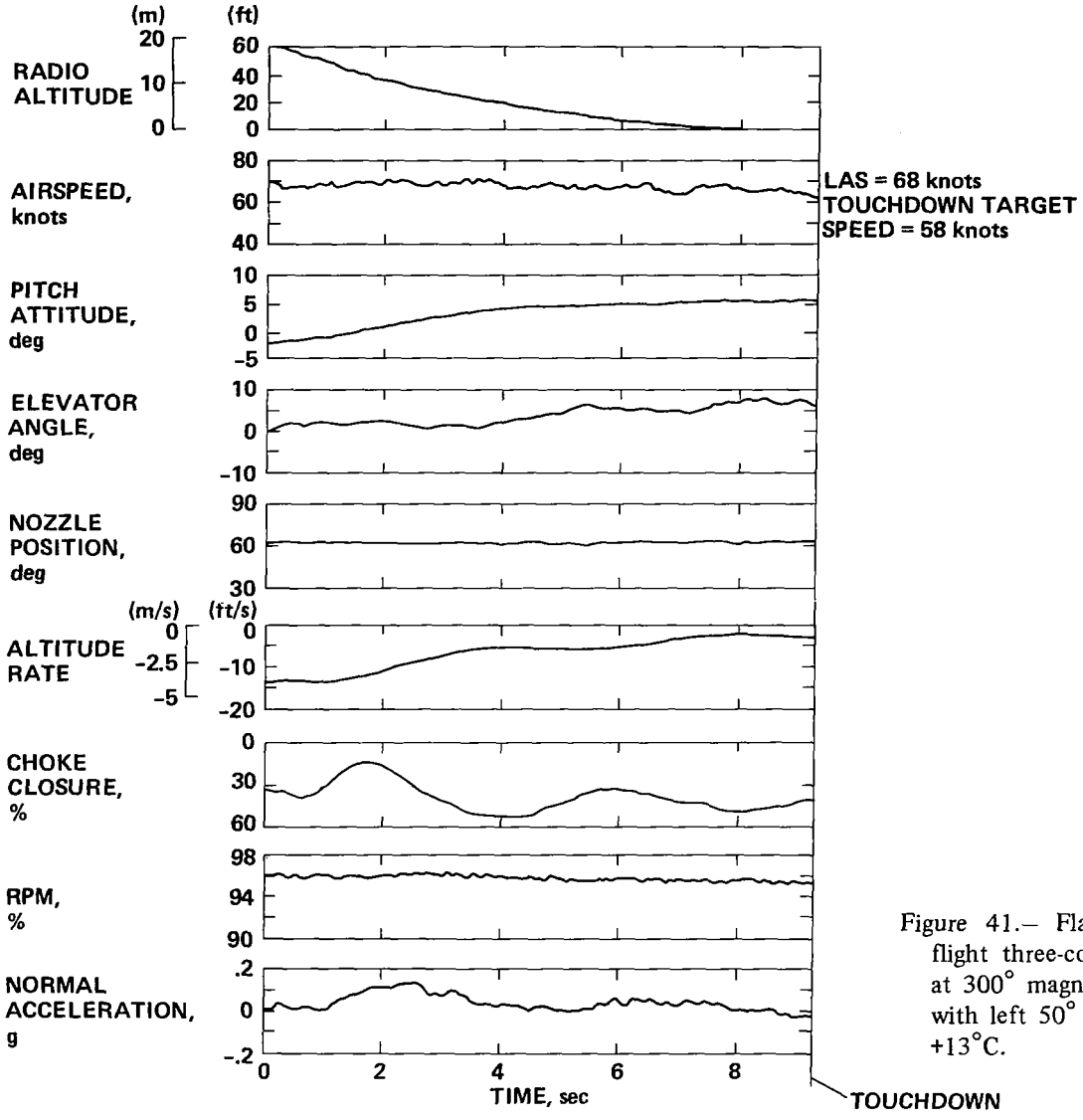

Figure 41.– Flare time history for the flight three-control system; mast wind at 300° magnetic, 12 knots (headwind with left 50° crosswind), standard day +13°C.

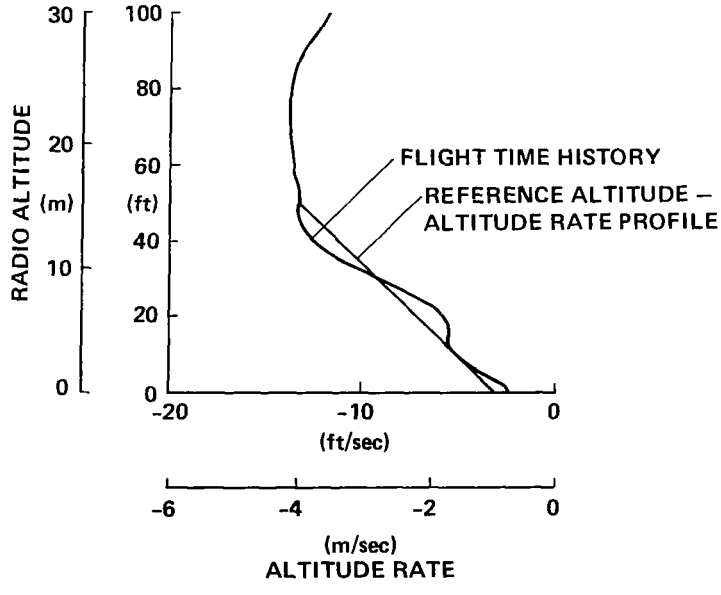

Figure 42.– Altitude vs altitude rate for the flight three-control system; mast wind at 300° magnetic, 12 knots (headwind with left 50° crosswind), standard day + 13°C.

In a two-segment flare maneuver, the altitude rate initially decreased, then temporarily held at an intermediate value, and finally decreased to end up near the touchdown-target sink rate. The two-segment characteristic is also seen in the altitude-altitude rate profile in figure 42, which indicates that the two-segment maneuver was the result of an initial overshoot of the desired profile followed by an opposite-direction correction back to the profile. The pilots often commented on and objected to the two-segment flare maneuver. They preferred an asymptotic approach to the final touchdown sink-rate target value.

There were no strong wind conditions encountered during the three-control-system flight tests.

Figure 43 shows how the two-control system performed a flare in a strong-wind situation, specifically, in an 18-knot crosswind. The corresponding glide-slope track and flare time history is shown in figures 28(a) and (b). The airspeed, which was 68 knots at flare entry, dropped to 63 knots at touchdown in an oscillatory fashion. The oscillatory tendency is also seen in the altitude rate and rpm records in figure 43. The path-tracking gain, $k_{\delta_{T_c}}$ in figure 15, although apparently adequate for glide-slope tracking, was perhaps too high for use during the flare where a significant change in the flightpath angle was demanded. The oscillatory tendency in figure 43, while objectionable, did not produce an unsatisfactory landing. Any decrease in the path-track gain would result in degraded performance. On the other hand, any increase in the path track gain could have resulted in decreased stability in the flare.

The altitude-altitude rate profile (fig. 44) corresponds to the time histories shown in figure 43. The oscillatory tendency is evident in figure 44 but there is no doubt that the

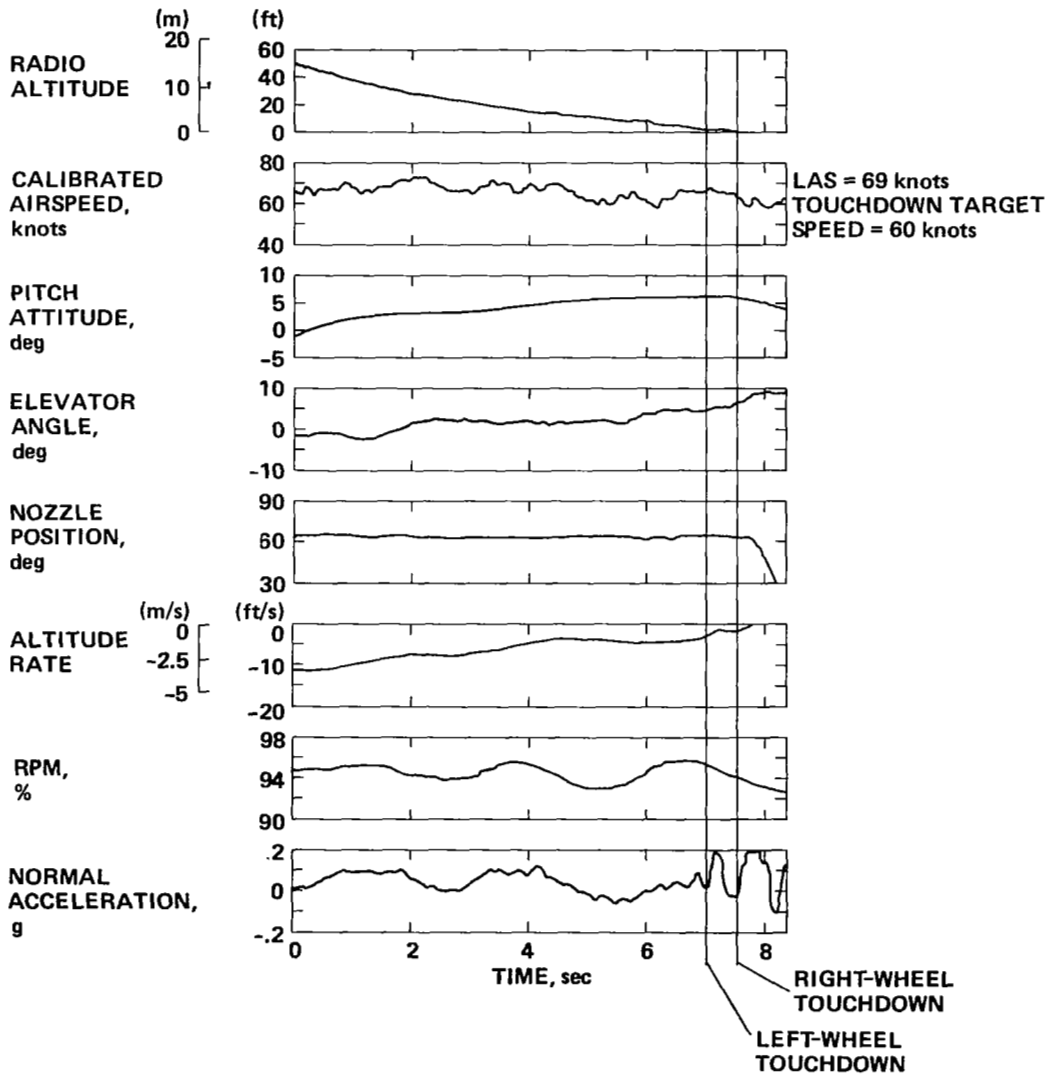

Figure 43.– Flare-time history for the two-control system; mast wind at 300° magnetic, 18 knots (headwind and left 50° crosswind), standard day -2° C.

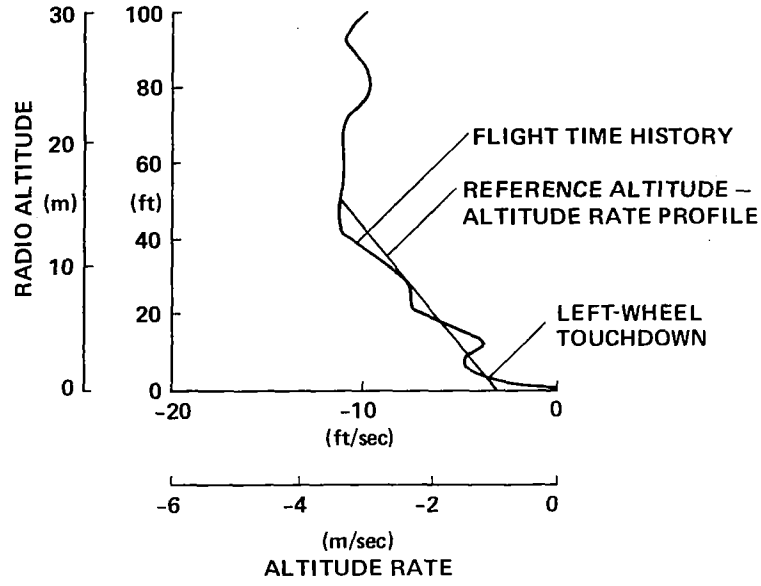

Figure 44.– Altitude vs altitude rate for the two-control system; mast wind at 300° magnetic, 18 knots (headwind and left 50° crosswind), standard day -2° C.

general altitude rate trend was progressing toward a satisfactory touchdown with altitude-rate errors generally within 0.3 m/sec (1 ft/sec) of the profile. The gradual decrease in the sink rate at touchdown is caused by the strong left crosswind.

Tailwind– A tailwind situation represents the most extreme steady condition that will be encountered by the autoland system. The control system must deal with a large incremental change in altitude rate to accomplish the flare.

Figure 45 shows the expanded time history of the flare maneuver for the four-control system operating in a tailwind situation as severe as is required to be demonstrated in a CTOL transport certification simulation study (ref. 22). Figure 45 corresponds to the time history shown in figures 29(a) and (b). The flare maneuver for the tailwind situation was very similar to the calm-wind situation except that the changes in pitch attitude and altitude rates were greater for the tailwind. The change in altitude rate required to go from glide-slope track to the target-touchdown sink rate required a significant control input from the chokes and the rpm. The chokes reached the fully closed limit and moved at rates near the software rate limit to establish the airplane on the reference altitude-altitude rate profile.

Figure 46 shows that the airplane dropped below the desired altitude-altitude rate profile initially but was on the profile as the airplane descended through 4.6 m (15 ft).

As noted in the section on glide-slope track performance, no significant tailwind situations were encountered with either the flight configuration three-control system or the two-control system.

Statistical Flare Summaries

The statistical touchdown performance achieved for all three control systems evaluated both in flight and with the high-speed simulation of the AWJSRA autoland system is summarized and compared in this section. The first three figures in this section present the touchdown sink-rate performance of the four-, three-, and two-control systems, respectively.

Figure 47 shows the results of 31 flight-test approaches with the four-control system, indicated by circles, and the simulation data, indicated by solid lines. In general, between 2,000 and 10,000 simulation runs were required to construct the simulation line but this number of runs was still not adequate to confidently predict the actual 10^{-6} probability performance. A straight line was used to extrapolate the available simulation data to the 10^{-6} hard-landing probability level. The controls are assumed to be operating without encountering limits. This procedure was not adequate for extrapolation in the other direction to the $1\text{-}10^{-6}$ soft-landing probability level since the touchdown sink-rate line in figure 47 is necessarily a negative number. The extrapolated upward bend of the probability curve at the soft landing end of the curve was not observed in the AWJSRA autoland simulation data. However, the authors of reference 16, who conducted simulation studies for the AWJSRA and the L-1011, indicate that such an upward bend has been observed in the L-1011 autoland simulation studies where more than a million data points were generated.

The slope of the flight-test data is steeper than the slope of the simulation data. This difference in the slopes reflects the light winds encountered in flight compared to the

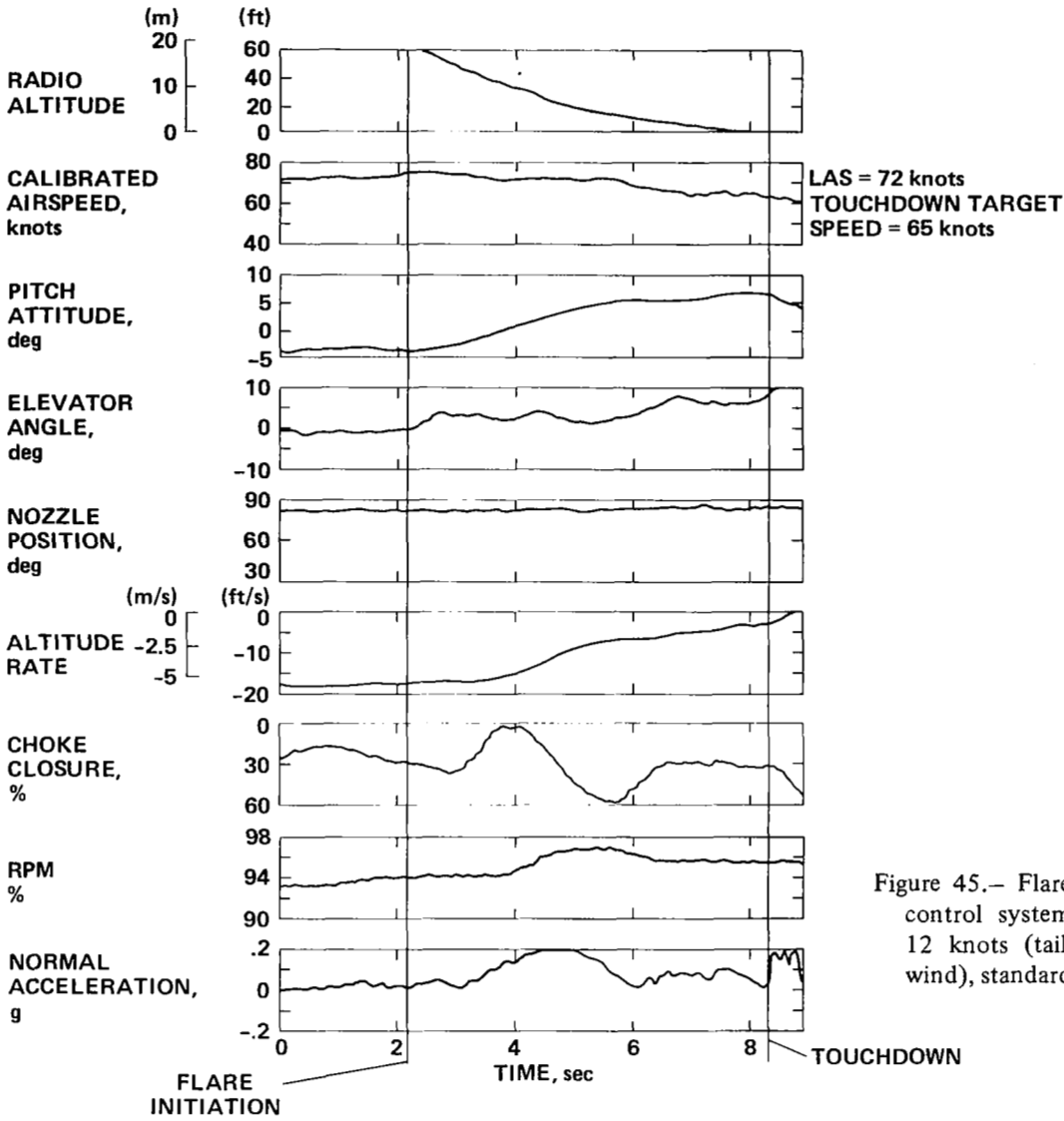

Figure 45.– Flare time history for the four-control system; wind at 130° magnetic, 12 knots (tailwind and right 45° crosswind), standard day -3°C.

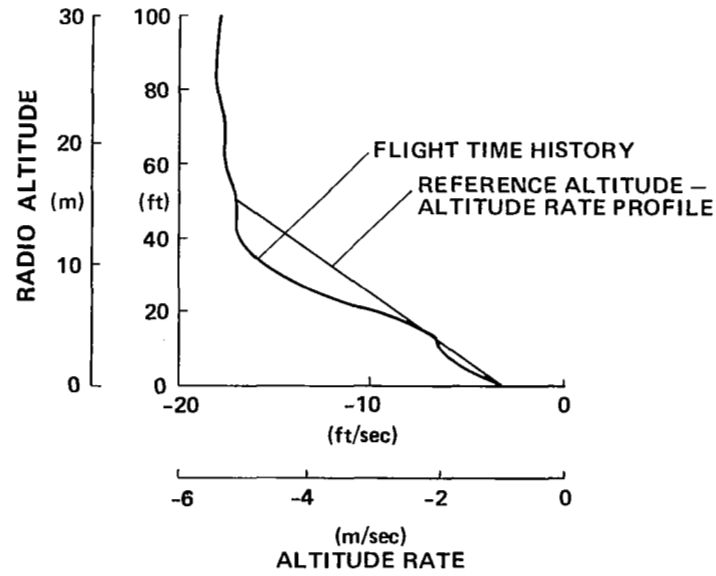

Figure 46.– Altitude vs altitude rate for the four-control system; mast wind at 130° magnetic, 12 knots (tailwind and right 45° crosswind), standard day -3°C.

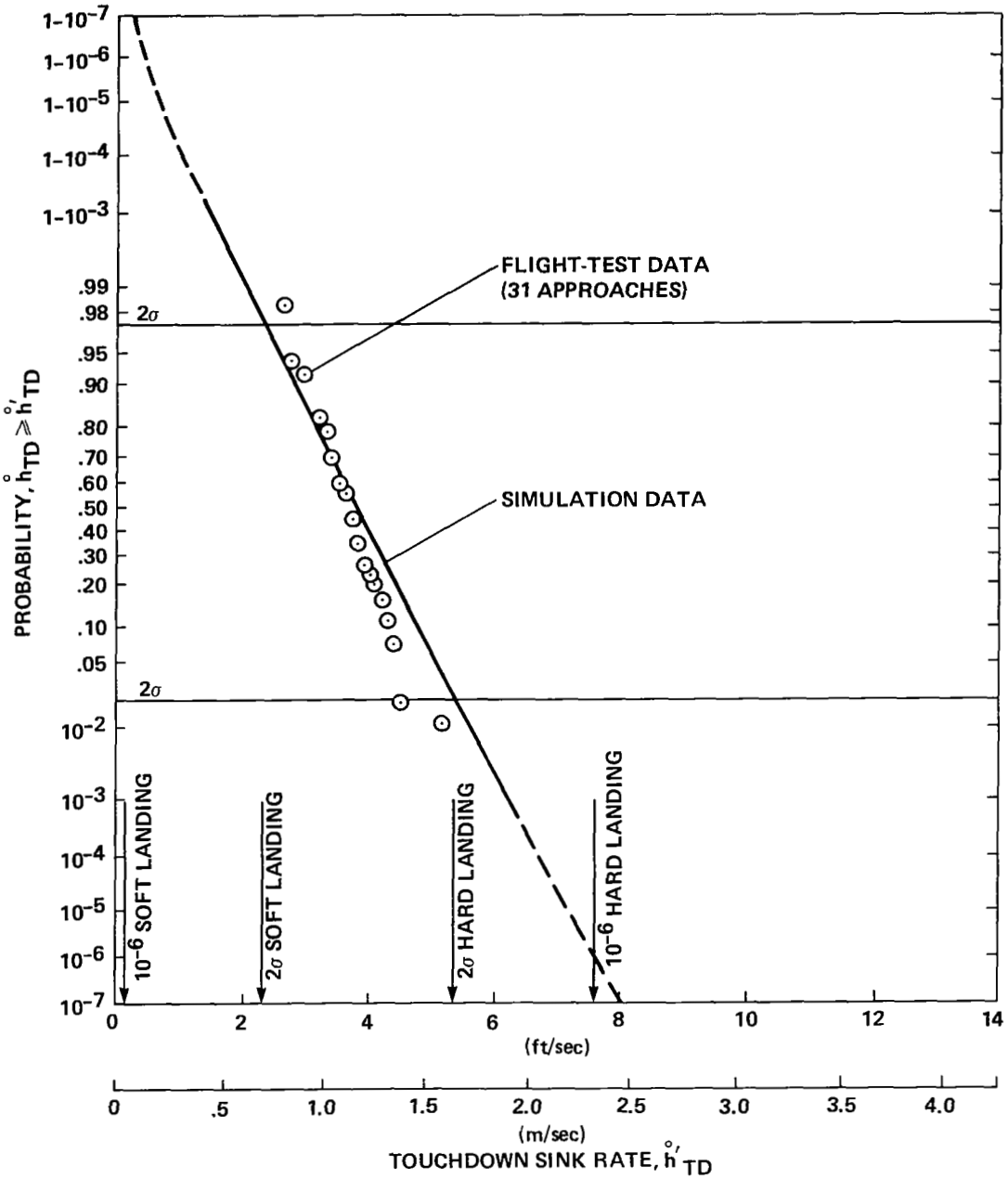

Figure 47.– Touchdown sink-rate performance of the four-control system.

moderate winds adopted for the simulation. Since the throttle and chokes were actively controlling the sink-rate variable, as opposed to the range, there was good agreement between the flight and simulation touchdown data.

The highest touchdown sink rate observed during the flight testing of the four-control system was 1.6 m/sec (5.2 ft/sec). The 10^{-6} probability hard landing predicted by the simulation data was 2.3 m/sec (7.6 ft/sec) which was well within the 3.8 m/sec (12.5 ft/sec) landing-gear strength limit of the AWJSRA.

Figure 48 summarizes the flight-test data for 29 approaches with the flight configuration three-control system, simulation data for the flight configuration three-control system, and simulation data for the design configuration three-control system. The simulation data, for

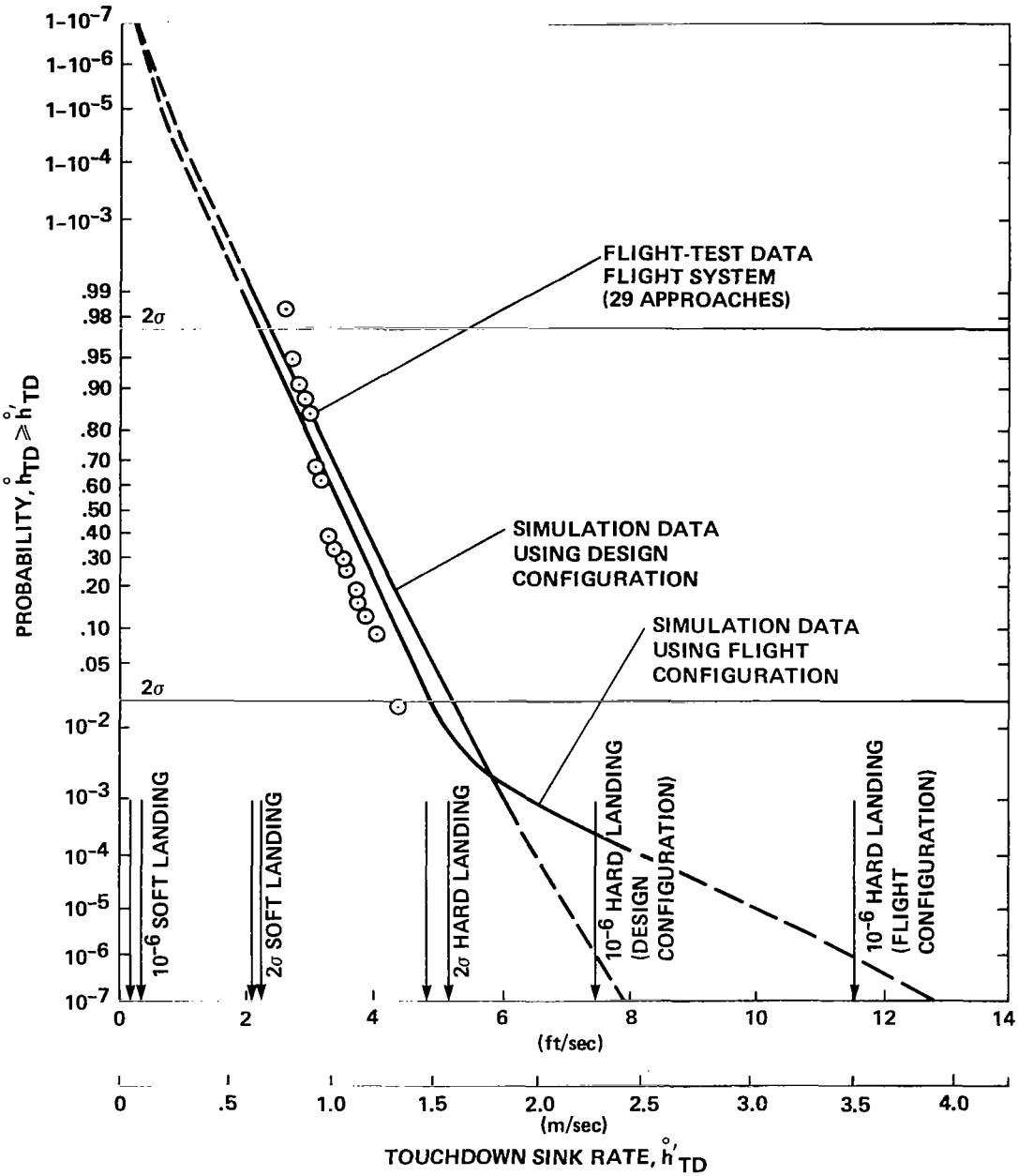

Figure 48.– Touchdown sink-rate performance of the three-control system.

the flight configuration three-control system show the adverse effect of choke-limiting on touchdown sink-rate performance. The performance is satisfactory for the majority of the approaches but hard landings occurred at low-probability levels because the chokes were on limits and the rpm was providing no effective control. Since only light to moderate wind conditions were encountered during the flight testing, the choke-limiting was not observed in the flight data.

The design configuration three-control simulation data in figure 48 indicate performance essentially identical to the performance of the four-control system in figure 47. This was expected since the only difference between the four- and three-control systems was the method of controlling airspeed.

Figure 49 summarizes the flight and simulation performance of the two-control system. Again, the spread in the simulation data exceeds that of the flight data because of the light winds encountered in flight. The extrapolation of the simulation data to the 10^{-6} probability level projects that the highest sink rate landing would be 3.5 m/sec (11.6 ft/sec) which is within the AWJSRA gear-strength limit of 3.8 m/sec (12.5 ft/sec).

Table 3 is a summary of the touchdown sink-rate performance of the control systems either flight-tested or simulated. All of the systems would be considered satisfactory from the point of view that, at the 10^{-6} probability level of a hard landing, the sink rate should not exceed the 3.8 m/sec (12.4 ft/sec) gear limit of the AWJSRA. On the other hand, the softer 10^{-6} hard-landing result of 2.3 m/sec (7.6 ft/sec) for the four-control system and the 2.9 m/sec (7.5 ft/sec) for the design configuration three-control system could have design implications for the landing gear.

The 2σ data shown in table 3 were read from the simulation data in figures 47–49. These data provide a measure of the spread in performance that would be expected in the majority (98%) of the landings. There is little indication of

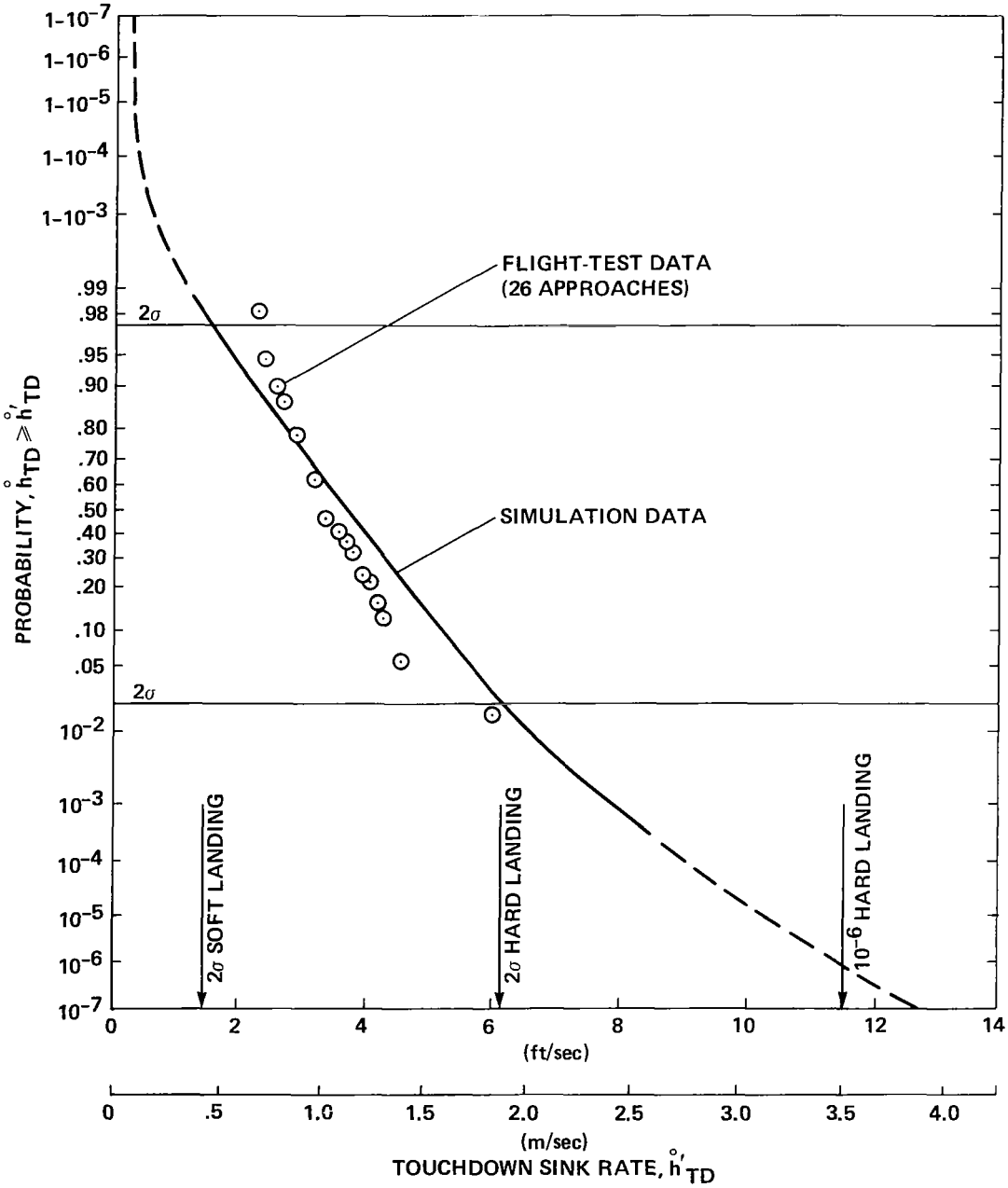

Figure 49.– Touchdown sink-rate performance of the two-control system.

TABLE 3.– SUMMARY OF TOUCHDOWN SINK RATE PERFORMANCE

Touchdown sink rate	Four controls		Three controls			Two controls	
	Flight, m/sec (ft/sec)	Simulation, m/sec (ft/sec)	Flight, m/sec (ft/sec)	Simulation configuration		Flight, m/sec (ft/sec)	Simulation, m/sec (ft/sec)
				Flight, m/sec (ft/sec)	Design, m/sec (ft/sec)		
Number of data points	31	>2000	29	>2000	>2000	26	>2000
2σ soft	0.79 (2.6)	0.70 (2.3)	0.76 (2.5)	0.64 (2.1)	0.67 (2.2)	0.67 (2.2)	0.49 (1.6)
Mean	1.13 (3.7)	1.16 (3.8)	.97 (3.2)	1.07 (3.5)	1.13 (3.7)	1.01 (3.3)	1.13 (3.7)
2σ hard	1.52 (5)	1.65 (5.4)	1.31 (4.3)	1.46 (4.8)	1.58 (5.2)	1.52 (5)	1.89 (6.2)
10^{-6} hard		2.32 (7.6)		3.53 (11.6)	2.29 (7.5)		3.54 (11.6)
2σ dispersion	.73 (2.4)	.95 (3.1)	.55 (1.8)	.82 (2.7)	.91 (3)	.85 (2.8)	1.40 (4.6)

the relative advantages or disadvantages of the various control systems flight-tested when only the 2σ numbers are examined. It is only at the 10^{-6} probability level that the merits of the four-control and design configuration three-control systems emerge.

Touchdown-distance performance of each of the three AWJSRA autoland control systems evaluated in flight is shown in figures 50 through 52. Figure 50 presents the performance of the four-control system. The circles indicate the flight-test data from 31 approaches and the diagonal line summarizes the high-speed simulation data. The abscissa represents the touchdown distance measured with respect to the 7.5° MLS glidepath-intercept point (GPIP) shown in figure 5. The ordinate shows the probability that the touchdown distance will exceed the abscissa value. The shaded vertical band in figure 50 locates the 61-m (200-ft) STOL port touchdown zone marked as shown in figure 5. The solid portion of the simulation data line summarizes approximately 10,000 simulation approaches. The dashed portion of the simulation data line represents extrapolation of data beyond the 10,000 simulation approaches.

Figure 50 shows agreement between the flight and simulation data provided the differences in the wind conditions are taken into account. Recall that figure 21 indicated the winds during flight were generally less severe than the wind model specified in AC 20-57A, reference 22. Two trend lines have been fitted through the data shown in figure 50. The line labeled "light winds" shows the trend of the data falling between a probability of 0.1 and 0.9 which represents the approaches flown in either calm- or light-wind conditions. This line is steeper than the simulation-derived line obtained with the FAA autoland wind model. The line labeled "all winds" includes those approaches flown in winds that, as shown in figure 21, were greater than the winds specified by the FAA, which were used for the simulation. This line is parallel to the simulation data line. This match between the simulation and flight data established the validity of the simulation data. The small difference in the mean touchdown distance between flight and simulation can be attributed to the lack of explicit control of range in the AWJSRA autoland system and modeling discrepancies of the simulation model. Figure 50 shows that the touchdown dispersion for a 10^{-6} probability was 297 m (970 ft) and compares with 792 m (2600 ft) which was required for a wide-body transport (ref. 18).

The circles in figure 51 represent the performance of the flight configuration three-control system during the flight tests. Simulation data for both the flight configuration and design configuration three-control system are shown by the lines. The choke limiting, which occurred with the flight configuration three-control system, had almost no effect on the touchdown-distance performance.

The landing-distance performance of the two-control system that was flight-tested and simulated is presented in figure 52. The two-control system lacked the bandwidth needed to minimize the touchdown-distance dispersion.

Table 4 summarizes the touchdown-distance performance from all of the systems that were flight-tested or simulated. Almost identical touchdown distance dispersions were obtained from the four-control system and from each of the three-control-system configurations. The touchdown distance dispersions of the two-control system were significantly worse than those of either the three- or four-control systems.

No touchdown-dispersion requirement for the STOL airplane presently exists. However, reference 36 proposes that the STOL runway length could be defined as the sum of a touchdown dispersion, a transition segment (the distance from touchdown to the point where braking begins), and a stopping segment. If STOL port runway lengths were as short as those specified in the FAA planning document for STOL ports (ref. 3), and the method proposed in reference 36 were adopted, a strong premium would be placed on minimizing the touchdown dispersion. Under those circumstances, the performance exhibited in table 4 for the four- or three-control systems would be preferred over the performance of the two-control system.

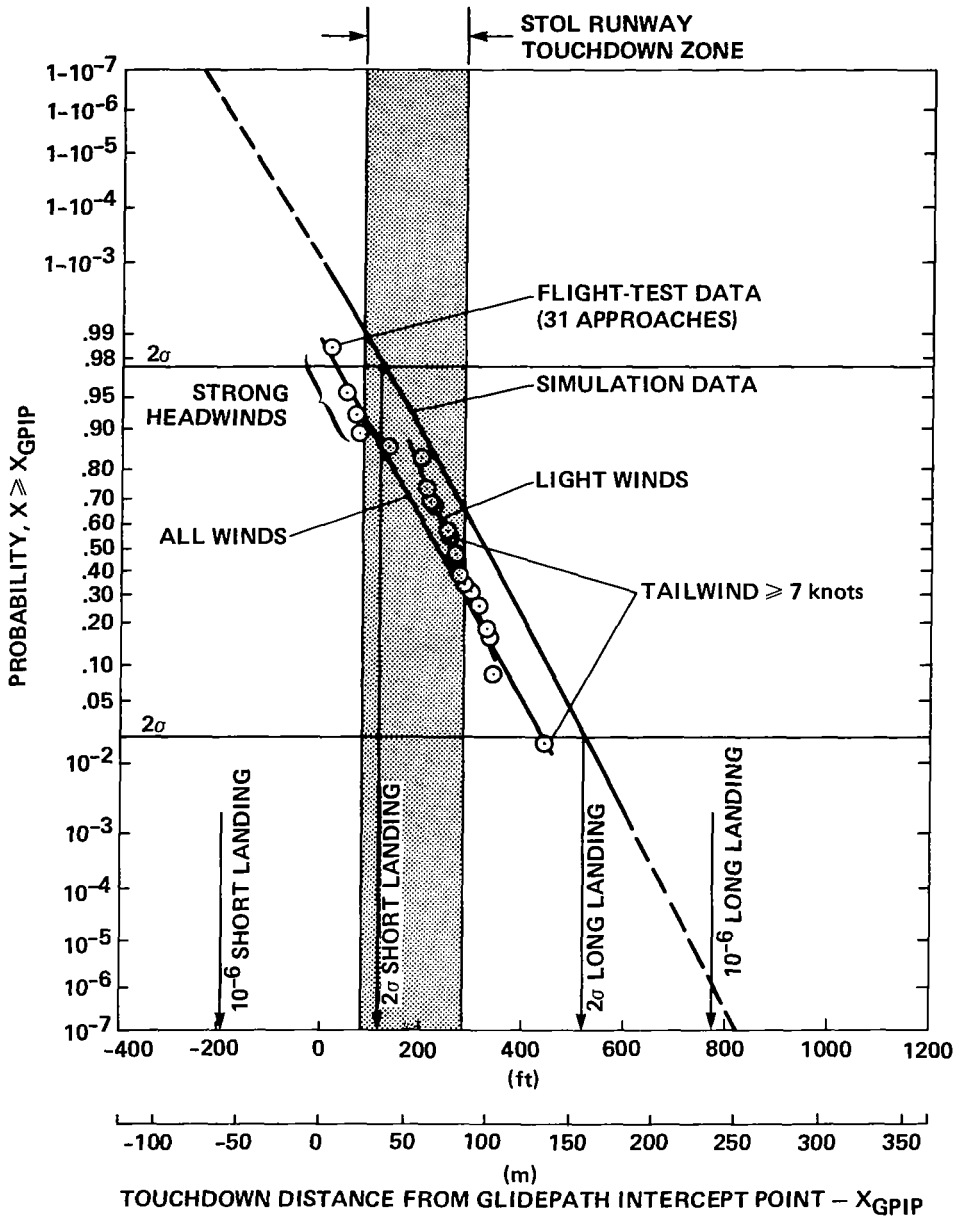

Figure 50.– Touchdown-distance performance of the four-control system.

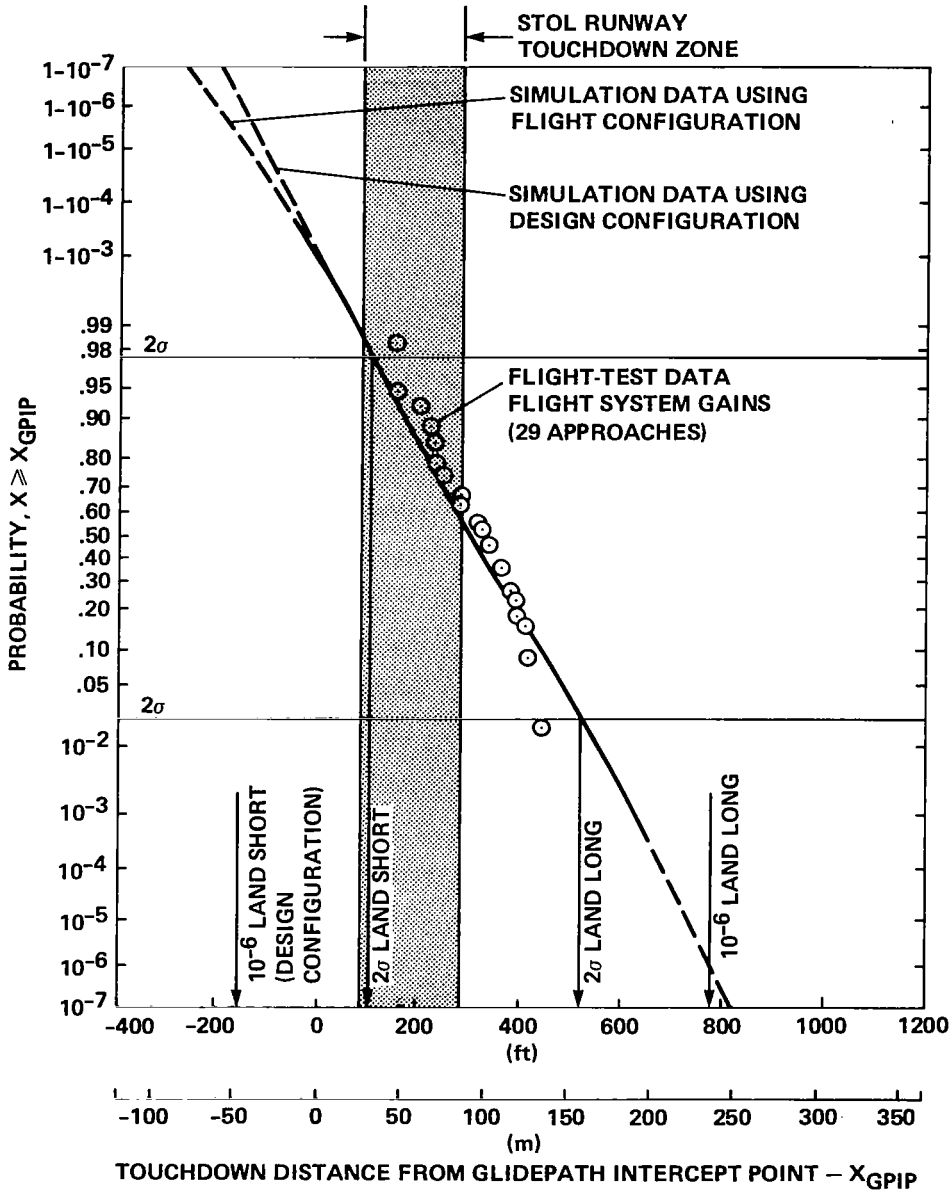

Figure 51.– Touchdown-distance performance of the three-control system.

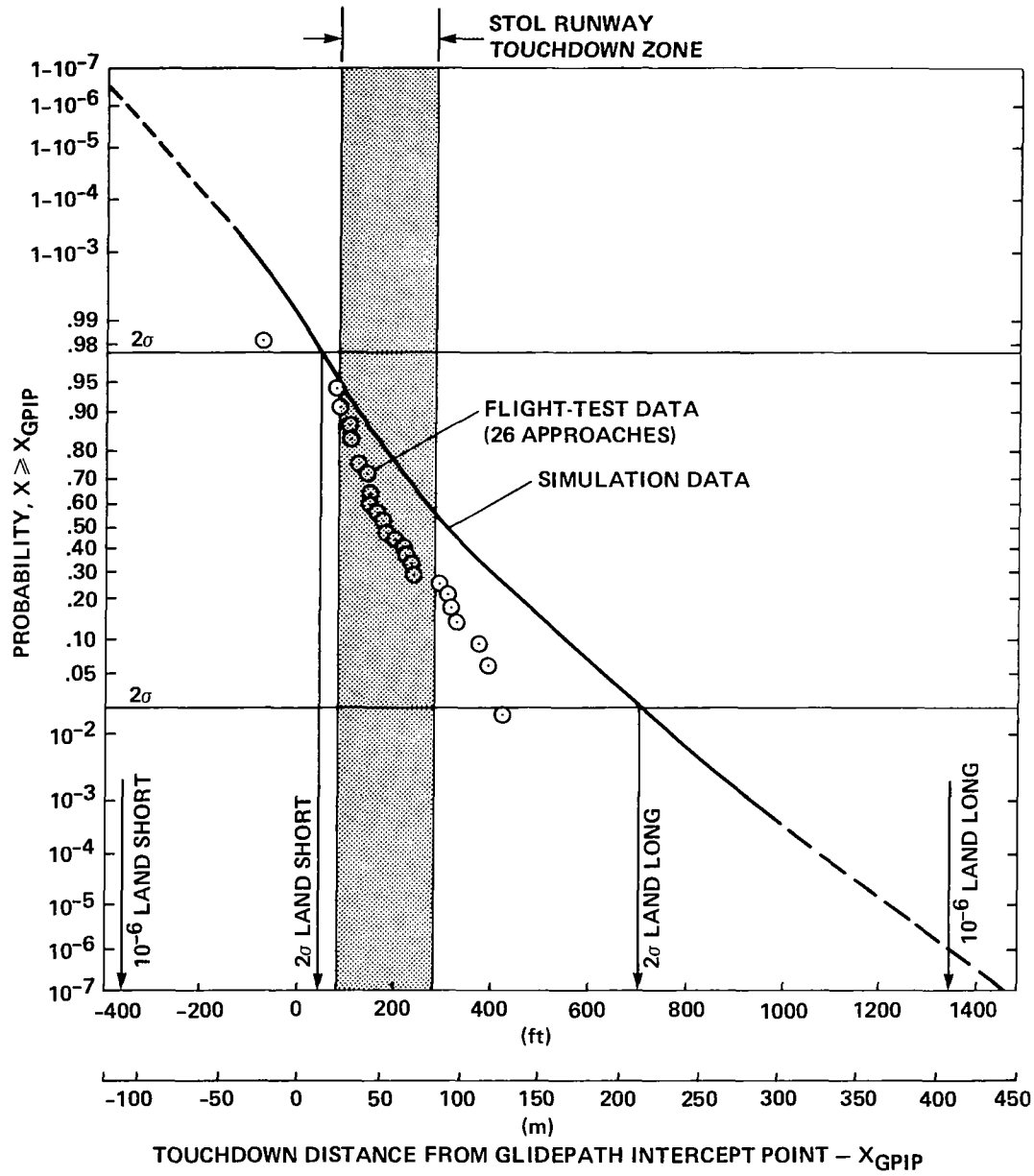

Figure 52.– Touchdown-distance performance of the two-control system.

TABLE 4.– SUMMARY OF TOUCHDOWN-DISTANCE PERFORMANCE

Touchdown distance from GPIP	Four controls		Three controls			Two controls	
	Flight, m (ft)	Simulation, m (ft)	Flight, m (ft)	Simulation configuration, Flight, m (ft)	Simulation configuration, Design, m (ft)	Flight, m (ft)	Simulation, m (ft)
Number of data points	31	>2000	29	>2000	>2000	26	>2000
10^{-6} short		-58 (-190)		-67 (-220)	-49 (-160)		-113 (-370)
2σ short	3 (10)	34 (110)	43 (140)	30 (100)	30 (100)	-24 (-80)	12 (40)
Mean	79 (260)	94 (310)	98 (320)	88 (290)	88 (290)	52 (170)	91 (300)
2σ long	131 (430)	155 (510)	128 (420)	158 (520)	158 (520)	128 (420)	213 (700)
10^{-6} long		238 (780)		238 (780)	238 (780)		408 (1340)
2σ dispersion	128 (420)	121 (400)	85 (280)	128 (420)	128 (420)	152 (500)	201 (660)
10^{-6} dispersion		296 (970)		305 (1000)	287 (940)		521 (1710)

On the other hand, if there were no premium on minimizing the runway length requirement, the performance of the two-control system would be considered satisfactory.

One of the requirements for the AWJSRA autoland flare system was that the airplane land on the main landing gear with the nose wheel well clear of the runway. Figures 53 through 55 summarize the pitch attitude at touchdown for the control systems either flight tested or simulated. All of the control systems produced satisfactory pitch attitude performance at touchdown. At the 10^{-6} probability level corresponding to the minimum touchdown pitch attitude, the pitch attitude always exceeded 2.5°.

While no simulation data are available for landing-touchdown-speed performance, the flight-data time histories indicate that the airplane typically touched down within 5 knots of the target-touchdown speed.

CONCLUDING REMARKS

An autoland research program has been conducted with a powered-lift STOL airplane, the Augmentor Wing Jet STOL Research Airplane (AWJSRA), flying into an MLS-equipped STOL port. This program has established navigation, guidance, and control laws suitable for flying steep approaches on the backside of the power-required curve to fully automatic touchdowns. This program has also provided information that will aid in establishing design specifications and certification criteria.

Three control systems were developed and tested in flight and in high-speed simulation. All of these systems were based on the concept that a powered-lift STOL airplane operates at low airspeeds that place the airplane on the backside of the power-required curve. The two-control system used the throttle to control engine rpm for regulating glide-slope path tracking and used the elevator to pitch the airplane for regulating airspeed. The three-control system used throttle complemented with direct-lift control chokes to regulate glide-slope path and used elevator to control airspeed. The four-control system also used throttle complemented with direct-lift control chokes for glide-slope tracking but airspeed was regulated with elevator for long-term speed corrections and nozzle vectoring for short-term speed regulation.

All three autoland control systems evaluated on the AWJSRA produced satisfactory glide-slope tracking performance but only the three- and four-control systems had the potential for producing touchdown performance that would permit operations into a STOL port as defined in reference 3. Specifically, the simulation data summary in table 2 indicates that all three control systems provided path-tracking capabilities that would satisfy the FAA glide-slope tracking requirement stated in AC 120-28B (ref. 23), for Category IIIa operations. The simulator data contained in tables 3 and 4 show the superior touchdown sink rate and range performance of the three- and four-control systems as compared with those of the two-control system. Data from tables 2, 3, and 4 indicate no significant difference between the glide-slope track and touchdown performance of the three- and four-control systems. This was because both systems used the autothrottle complemented with direct-lift-control chokes for path and sink-rate control. In spite of the use of nozzles for airspeed control, the speed-hold performance of the four-control system was no better than that of the three-control system. However, the flight-test program did provide evidence (see fig. 26) that a direct-drag device, such as the nozzles, may be beneficial in a horizontal wind-shear situation.

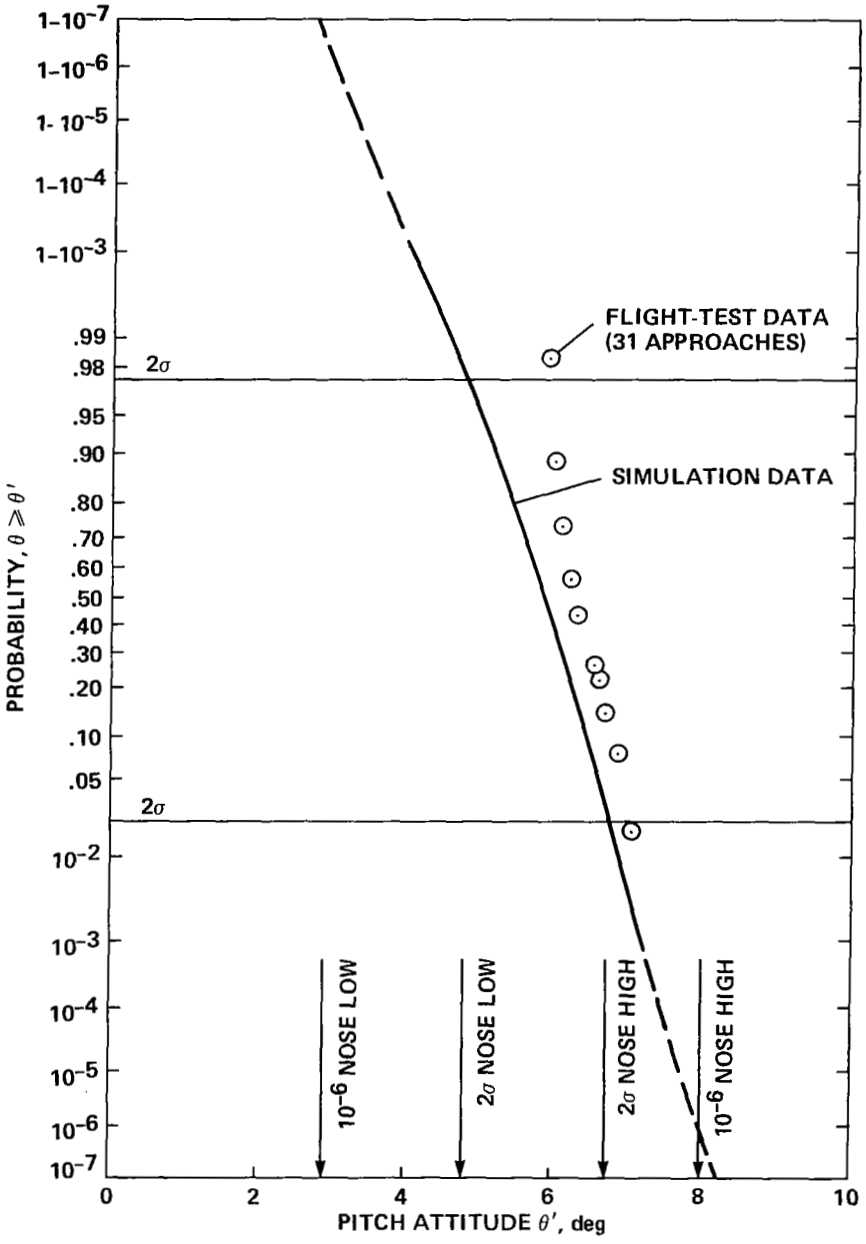

Figure 53.– Pitch attitude at touchdown of the four-control system.

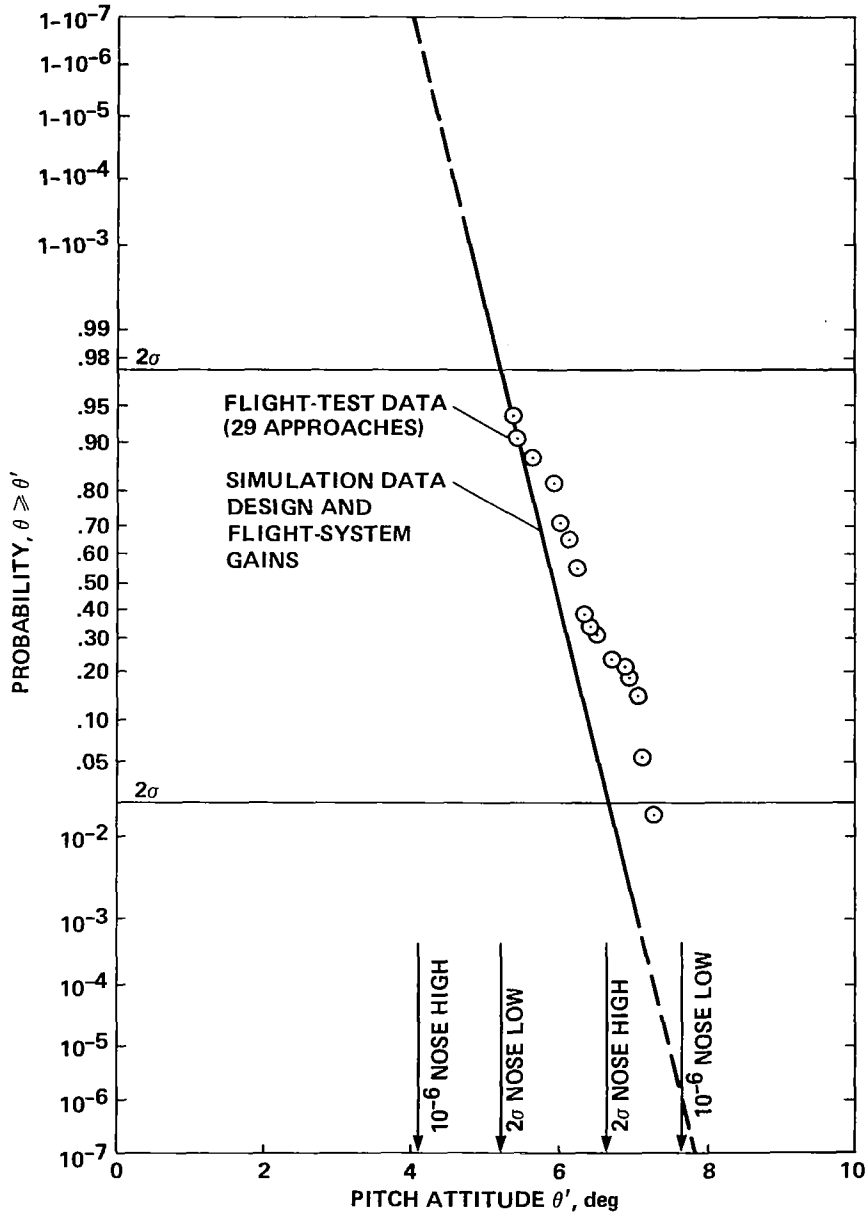

Figure 54.— Pitch attitude at touchdown of the three-control system.

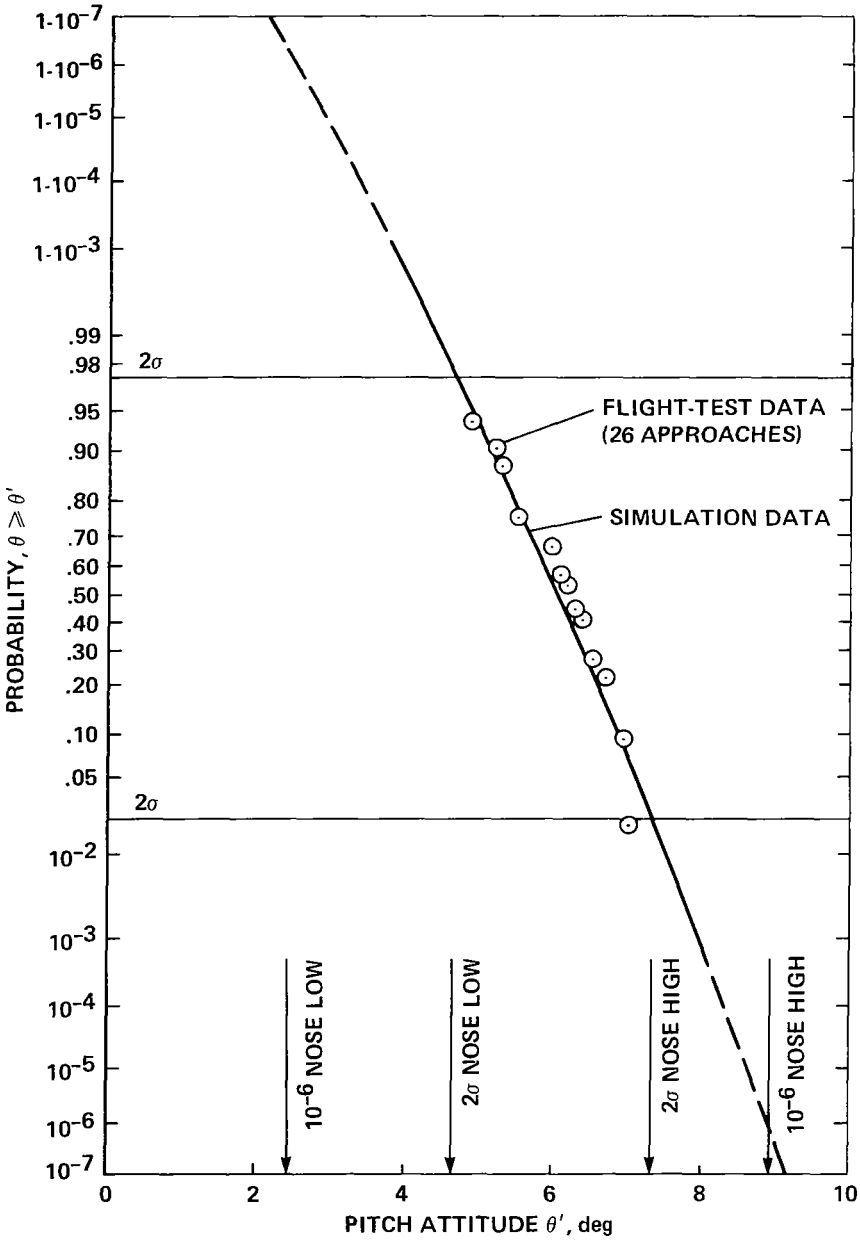

Figure 55.– Pitch attitude at touchdown of the two-control system.

For all three control systems evaluated on the AWJSRA, the autothrottle was the primary means for regulating glide-slope path tracking and for controlling sink rate during the flare. The autothrottle installed in the AWJSRA, when used alone as in the case of the two-control system, was only marginally capable of providing the path regulation and sink-rate control because of its slow response. Also, the fuel control used on the AWJSRA engines was intentionally designed to have a long time constant for power reductions to protect against a compressor stall resulting from an inadvertent large throttle decrease. The path control achievable with the autothrottle-engine response alone was adequate to fly the glide-slope in the presence of moderate turbulence but was marginal for the flare-maneuver requirement of precise touchdown sink-rate control. Improved touchdown sink-rate control was achieved for the three- and four-control systems on the AWJSRA by employing the DLC chokes to effectively increase the path-tracking responsiveness. The ±0.1-g authority of the DLC chokes was adequate for this application.

The use of raw MLS glide-slope deviation in the control law driving the autothrottle was considered in the planning stages of the research program. Raw MLS glideslope deviation might have been usable if the autothrottle alone had provided adequate path tracking and flare sink-rate control. However, with the introduction of the DLC chokes for achieving fast path response, smooth glide-slope deviation and deviation rate were required. These smooth signals were provided with a complementary filter which blended glide-slope deviation with vertical acceleration and another complementary filter which blended radio altitude and vertical acceleration. Satisfactory filter frequencies were 0.1 rad/sec for the glide-slope filter and 0.6 rad/sec for the radio-altitude filter.

Atmospheric conditions exceeding 20-knot headwinds, 15-knot crosswinds, and 10-knot tailwinds were encountered during the course of the flight testing of the AWJSRA autoland system. The few strong-wind events experienced during the flight testing were not sufficient in number to accurately define the performance differences between the three control systems. However, the winds encountered during flight testing did provide an indication that the autoland system for a powered-lift STOL airplane can probably cope with winds as strong as those used for autoland design studies for CTOL transports.

In summary, based on performance measures similar to those presently used for autoland certification of CTOL transports but adjusted for low approach airspeeds, an automatic landing system for a powered-lift STOL airplane operating into an MLS-equipped STOL port appears feasible. Improved path tracking and precise sink-rate control can be incorporated into future powered-lift STOL airplanes in at least two ways – by providing precise thrust control through a combination of engine controls (fuel controls, variable stators in the compressor, etc.) and a fast-acting autothrottle actuator or by incorporating a fast-acting DLC device in the wing. The choice of fast-acting engine controls may be unsatisfactory because of the complexity of reliably increasing the response of the engine or because protection against abrupt throttle reductions must be maintained. The DLC provides a reasonable control for introducing limited authority but fast-acting path regulation. The disadvantage of the DLC is that approach speeds must usually be increased to maintain safe-approach margins.

Ames Research Center
National Aeronautics and Space Administration
Moffett Field, California, March 25, 1983

APPENDIX A

OPERATING LIMITS AND NOMINAL SPEED, RPM, AND NOZZLE SETTINGS

The operating limits that apply to conventional jet transports also apply to the AWJSRA. These include maximum thrust limits, flap placard speed limits, minimum-approach airspeed limits, and maximum-operating airspeed limits. The powered-lift airplane has additional minimum thrust and maximum angle-of-attack limits imposed by the need to maintain powered lift.

A comprehensive study of how to provide adequate safe-approach margins (speed, angle of attack, and thrust limits) for powered-lift aircraft is described in references 5 and 37. However, when the approach margin criterion was selected for the AWJSRA autoland program, the results described in reference 37 were not yet available. The criterion used for the AWJSRA autoland program was based on a maneuver margin for determining the minimum speed, minimum rpm, and the nozzle setting used during autoland flight tests. Maneuver margin is a measure of the vertical acceleration that can be achieved by rotating the airplane in pitch to the stall angle of attack under the condition that engine rpm is held constant. The defining equation for the maneuver margin is:

$$\Delta n = \frac{L_{max} - L}{W} \qquad \text{(A1)}$$

where Δn is the maneuver margin in g, L_{max} is the maximum lift available for a constant thrust setting, L is the aerodynamic lift for equilibrium flight, and W is the aircraft weight. Values of both L_{max} and L came from the aircraft simulation model (in refs. 30 and 31). Unpublished corrections to reference 30, which are based on flight-test experience, were incorporated in the simulation.

The conventional power-off 1.3 V_{stall} criterion used for CTOL airplanes provides an excessive margin for a powered-lift STOL airplane for two reasons. First, the power-off stall speed for a powered-lift STOL airplane can result in an approach speed higher than is possible using powered lift. Second, a CTOL airplane makes short-term glidepath corrections primarily with elevator while a powered-lift STOL airplane primarily uses thrust for glidepath corrections. The high effectiveness of thrust for path corrections means that less reliance must be placed on elevator to provide protection from atmospheric disturbances or for performing the flare maneuver. The CTOL transport criterion of 1.3 V_{stall} can be interpreted as a maneuver margin of 0.69 g. Because thrust corrections are effective for a powered-lift STOL airplane, a maneuver margin of 0.4 g has been judged to be adequate for the AWJSRA autoland work.

The following guidelines were adopted for the AWJSRA autoland work to meet the criterion for the maneuver margin.

1. A nominal engine-thrust target value was established for the approach which was a function of aircraft weight. This nominal engine thrust had to be low enough to provide at least a 2% engine rpm increase for upward-path correction before an rpm limit was encountered. By choosing the approach airspeed and nozzle setting correctly, this target thrust could be achieved.

2. A reference approach airspeed, called the landing approach airspeed, LAS, was selected as a function of aircraft weight. LAS was chosen to provide a maneuver margin $\geqslant 0.4$ g for the nominal engine thrust and for a nozzle angle operating range between 60° and 100°.

3. A nominal nozzle setting of 80° was adopted for the autoland approaches. This setting provided two advantages. First, the nozzle angle provided an x-force (longitudinal) capability which was nearly independent of the z-force (vertical) and was, therefore, a useful speed-control device. Second, with a nominal value of 80°, more than ±20° of nozzle angle was available for trim-path correction capability. This trim-path correction capability provided an effective means of maintaining a constant nominal rpm setting for the approach. This was necessary because head or tailwinds caused the airplane to fly different aerodynamic flightpath angles for a fixed approach, glide-slope angle. The values used as a result of these three guidlines follow.

Engine Thrust

The nominal engine thrust target value was equivalent to the following nominal rpm for a standard day.

$$N_{H_{nom}}(W) = 93.0\% + 2\% \frac{W - W_{min}}{W_{max} - W_{min}} \qquad \text{(A2)}$$

where $N_{H_{nom}}(W)$ is the reference high-pressure stage rpm in percent, W_{min} is the aircraft operating weight with minimum fuel which is 17,236 kg (38,000 lb), and W_{max} is the aircraft operating weight with maximum fuel which is 21,772 kg (48,000 lb). For nonstandard day temperatures the nominal rpm varied by about 1% per 4.5° C (10° F) to maintain the target thrust value. Altitude variations were not considered since all flights were conducted near sea level. The resulting nominal rpm was compared with the maximum limit rpm values shown in figure A1. When the requirement of a 2%

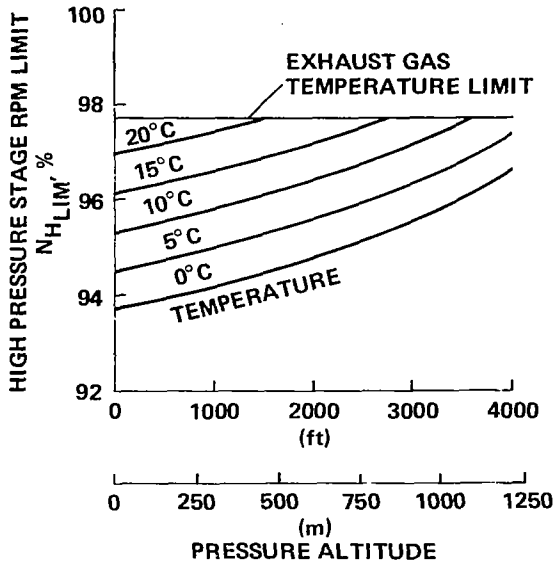

Figure A1.– RPM limits for nozzle deflections >30° as a result of thrust; thrust limit 2766 kg (6100 lb).

rpm authority between the maximum allowable rpm and the operating rpm was not met, the target thrust was lowered by increasing the approach airspeed and decreasing the nozzle angle setting.

Approach Airspeed

The nominal approach airspeed was given by:

$$LAS(W) = 63 \text{ knots} + 8 \text{ knots} \quad \frac{W - W_{min}}{W_{max} - W_{min}} \qquad \text{(A3)}$$

where $LAS(W)$ is the landing approach airspeed reference as a function of weight and the other symbols are defined in conjunction with equation (A2). The airspeed was increased by 2 knots for each percent of rpm reduction necessary to maintain the 2% rpm control authority.

Nozzle Angle

The nominal nozzle angle used as a function of different aerodynamic flightpath angles is shown in figure A2 for bank angles ranging from 0° to 30°. The nozzle angles shown in this figure were reduced by 5% for each percent of desired engine rpm reduction. By using the values of thrust, approach airspeed, and nozzle angle described above, the maneuver margin criterion of 0.4 g was maintained.

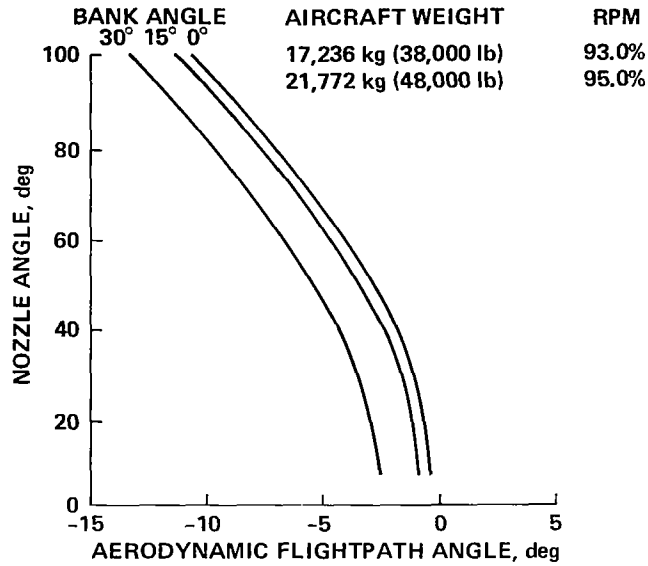

Figure A2.– Nozzle angle as a function of aerodynamic flightpath angle.

APPENDIX B

CLOSED-LOOP ENGINE-TRANSFER FUNCTION

This appendix describes a simple transfer function model for the autothrottle inner loop and indicates how the gains k_T, k_2, and k_3 in figure 13 were specified in terms of frequency and damping. When the engine was operating in the linear region needed for flying the glide slope, the relationship between the engine command (δT_1 and δT_2 in fig. 13) and the high-pressure rpm could be characterized as a single lag.

$$\frac{N_H}{\delta T_{i_c}} = \frac{0.72}{\tau_e s + 1} \tag{B1}$$

The steady-state gain from the throttle handle position to rpm was 0.72, N_H was the high-pressure stage rpm, δT_{i_c} was the ith engine command; and τ_e was the engine time constant primarily associated with the fuel-control unit. The AWJSRA fuel control had a different time constant for a power increase than for a power decrease. For purposes of closed-loop analysis, the engine time constant is assumed to be 1 sec. The values of the engine time constant were determined from flight records by a method described in reference 29.

A linear transfer function from throttle command (δT_c in fig. 13) to rpm, which applied when rpm was not limited, was derived from figure 13.

$$\frac{N_H}{\delta T_c} = \frac{0.72\, k_T}{\tau_e s^2 + (1 + \tau_e k_2 k_T)s + k_T(k_2 + k_3)} \tag{B2}$$

The symbols that appear in equation (B2) were defined in connection with the autothrottle-choke complement block diagram in figure 13. This transfer function can be written in a more general form.

$$\frac{N_H}{\delta T_c} = \frac{0.72\, \omega_n^2}{s^2 + 2\zeta\omega_n s + \omega_n^2} \tag{B3}$$

where ω_n is the closed-loop natural frequency, s is the Laplace operator, and ζ is the damping ratio. Any choice of ω_n and ζ could be established by appropriate selection of the parameters k_T, k_2, and k_3. By choosing $k_2 + k_3 = 1$, the closed-loop and open-loop steady-state gain remained 0.72. The coefficients in equations (B2) and (B3) were then related as follows for $\tau_e = 1$.

$$2\zeta\omega_n = 1 + k_2 k_T \tag{B4}$$

$$\omega_n^2 = k_T \tag{B5}$$

APPENDIX C

DERIVATION OF THE GLIDE-SLOPE CAPTURE CONTROL LAW

The glide-slope capture law for the AWJSRA autoland system made use of a circular arc to provide a constant, normal-acceleration capture maneuver. The geometry for deriving the control law is shown in figure C1. The symbols used in figure C1 are defined below.

e error between the glide slope and the circular capture arc

R slant range to touchdown

R_C slant range to touchdown at the beginning of glide-slope capture

R_T slant range to touchdown at the beginning of glide-slope track (end of glide-slope capture)

β glide-slope deviation angle, + when the airplane is below the glide slope

γ flightpath angle

γ_C flightpath angle at the beginning of the capture maneuver

γ_{GS} glide-slope reference, -7.5°

γ_{REF} target flightpath angle

Δh path error from the circular capture arc

ρ radius of curvature of the circular capture arc

The error between a point on the circular capture arc and the glide slope is approximately:

$$e = \left[\rho^2 + (R - R_T)^2\right]^{1/2} - \rho \qquad \text{(C1)}$$

With the aid of a binomial series expansion of the square root term, equation (C1) reduces to:

$$e \cong \frac{(R - R_T)^2}{2\rho} \qquad \text{(C2)}$$

The path error, Δh, is the difference between the glide-slope displacement, $R\beta$, and the error between the circular arc and the glide slope.

$$\Delta h = R\beta - \frac{(R - R_T)^2}{2\rho} \qquad \text{(C3)}$$

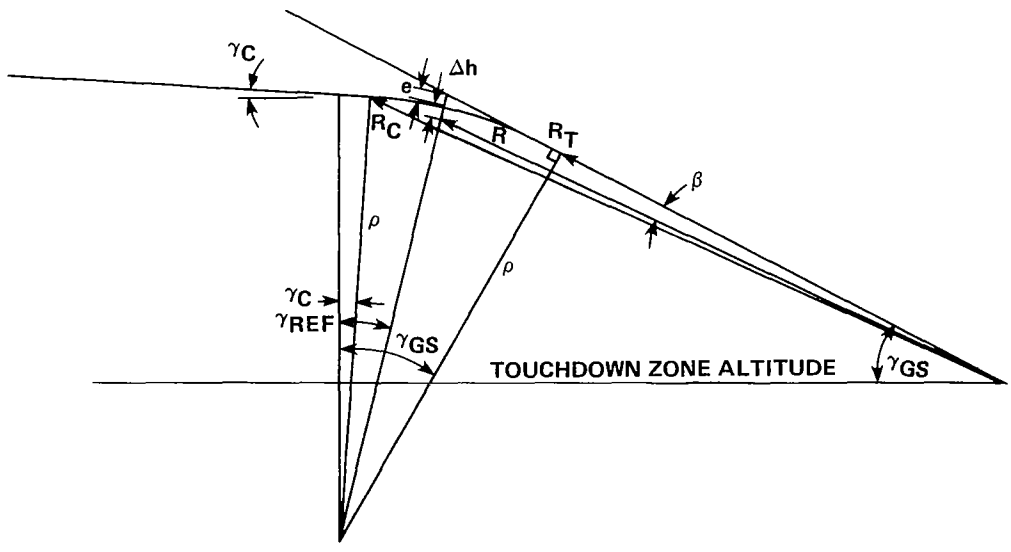

Figure C1.– Geometry of the glide-slope capture-control law.

The time to capture T_c is the distance traveled during the capture divided by the groundspeed. The landing approach airspeed was used for groundspeed in this equation.

$$T_c = \frac{\rho(\gamma_c - \gamma_{GS})}{V_g} \tag{C4}$$

Equation (C4) can be rearranged to provide an expression for the radius of curvature.

$$\rho = \frac{T_c V_g}{\gamma_c - \gamma_{GS}} \tag{C5}$$

Substituting the radius of curvature from equation (C5) into equation (C3) provides the following result for glide-slope capture path error.

$$\Delta h = R\beta - \frac{(\gamma_c - \gamma_{GS})(R - R_T)^2}{2T_c V_g} \tag{C6}$$

Equation (C6) shows that the path error of the glide-slope-capture control law is established by subtracting the term $(\gamma_c - \gamma_{GS})(R - R_T)^2/2T_c V_g$ from the estimated glide-slope error signal obtained from the glide-slope complementary filter in figure 8. The first differentiation of equation (C6) provides the path-deviation rate, $\Delta\dot{h}$, from the circular capture arc.

$$\Delta\dot{h} = R\dot{\beta} - \frac{(\gamma_c - \gamma_{GS})(R - R_T)}{T_c} \tag{C7}$$

Equation (C7) shows that the path-rate error of the glide-slope capture-control law is established by substituting the term $(\gamma_c - \gamma_{GS})(R - R_T)/T_c$ from the estimated glide-slope rate error signal shown in figure 8. As will be shown later, an expression for R_T is never specifically determined. Instead, the term $(R - R_T)$ is replaced by an estimated speed multiplied by the capture time. A value of 20 sec was adopted for T_c to assure that the glide-slope capture would be accomplished in sufficient time to ensure that the airplane would be established on the glide slope before descending through 152 m (500 ft) above the touchdown zone. Times < 20 sec produced very abrupt glide-slope capture maneuvers.

The flightpath angle reference, γ_{REF}, shifts from an initial value γ_c at the beginning of glide-slope capture to the glide-slope reference γ_{GS}, at the end of the capture. An expression for computing γ_{REF} uses $R - R_T$ as an approximation to the arc length of the circular capture path so that:

$$\gamma_{REF} = \gamma_{GS} + \frac{R - R_T}{\rho} \tag{C8}$$

Substituting ρ from equation (C5) into equation (C8) results in the following expression for γ_{REF}.

$$\gamma_{REF} = \gamma_{GS} + \frac{(\gamma_c - \gamma_{GS})(R - R_T)}{T_c V_g} \tag{C9}$$

The reference flightpath angle γ_{REF} is an input to the trim table in figure 7.

The capture of the glide slope began when a point on the circular capture arc matched the path deviation, $R\beta$. This point was reached when the right side of equation (C6) became negative as the airplane approached the glide slope. In equation form, capture began when:

$$R\beta - \frac{T_c V_g}{2}(\gamma_c - \gamma_{GS}) = 0 \tag{C10}$$

The left side of equation (C10) was derived from the right side of equation (C6) by noting that the arc length from the beginning to end of the capture, $R_c - R_T$, was $\cong T_c V_g$.

APPENDIX D

MEASURED WIND DATA

Wind data recorded during flight were derived from three sources: (1) airport control-tower reports, (2) a mast wind measurement near the STOL port touchdown zone, and (3) a postflight estimate of wind derived from air data and tracking radar.

The tower reported winds in the form of wind direction (relative to magnetic north) and magnitude (in knots). Winds were reported to the pilot as the airplane turned onto the final approach when the airplane was approximately 2 min away from touchdown. Wind magnitude was reported to the nearest knot except for speeds under 3 knots which were reported as "calm." In strong, gusty-wind conditions, both the mean value of the wind and the peak value of the gust were reported. Direction was reported to the nearest 10°. The control-tower reporting procedure is standard practice at all airports. These tower reports were only approximate estimates of actual conditions at touchdown and were used to provide preliminary labels for the approaches but were not otherwise considered in analyzing performance results.

The wind-data mast near the STOL port runway (fig. 5) was located 80 m (262 ft) short of the beginning of the marked touchdown zone, 73 m (240 ft) to the west of the runway centerline and 5.5 m (18 ft) above the touchdown zone altitude. Data from the mast were transmitted to the telemetry van and were added to a time-referenced, merge-data magnetic tape along with aircraft sensor and radar-tracking data. The mast instruments provided accurate wind speed and direction at one point in space near the end of the airplane approach path. The wind labels on the time histories in this report refer to mast wind data.

The postflight estimate of wind was established, as shown in figure D1, by forming the difference between airspeed from the aircraft data sensors and groundspeed derived from radar tracking. The radar data were available in the STOL port runway coordinate system described in figure 5. These data, sampled 4/sec, were smoothed using a second-order polynomial fit through 13 data points to make the estimate; six data points before the current data point, and six data points after the current data point. True airspeed, angle of attack, and sideslip data from the air data sensors were also smoothed using the polynomial-fit technique. The airspeed was resolved through the angle of attack and sideslip angle to form speed components in the airplane body axes. The airspeed components were then resolved through the bank, pitch, and yaw angles into the runway axes. The difference between the radar-derived groundspeed and airspeed was the wind estimate with components in the runway-coordinate system. To make the wind estimate compatible with standard wind-reporting practice, the wind components of the runway axes were also resolved into wind magnitude and direction.

The quality of the data from the postflight estimation method of determining wind magnitude and direction was limited by the quality of the airspeed signal, the accuracy of resolution of the angle of attack and the sideslip angle, the resolution of the Euler angles relating the airplane body axes to the runway axes, and the quality of the radar-tracking

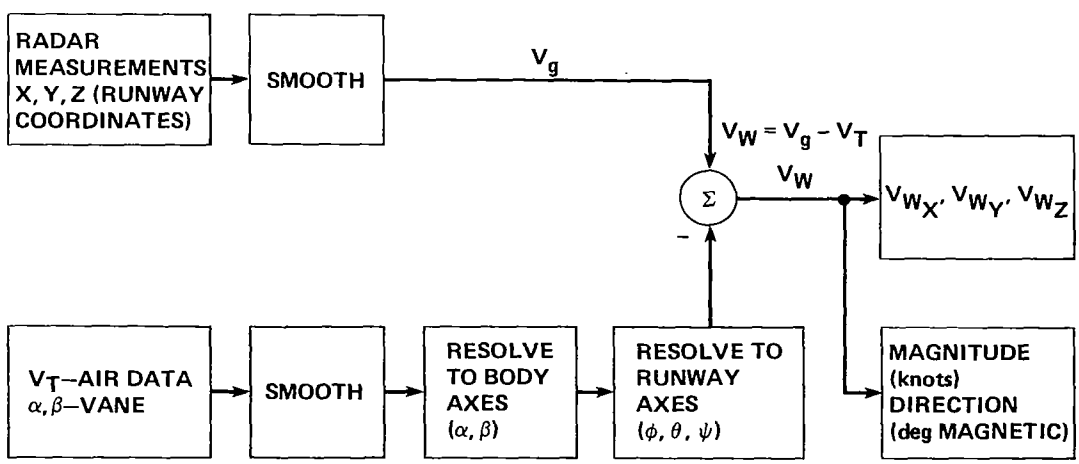

Figure D1.– Wind-determination procedure.

data. The radar-tracking data were reliable as long as the radar antenna automatically tracked a transponder antenna located on the right side of the airplane fuselage below the copilot's window. Because of multipath effects, the radar elevation antenna did not track accurately when the airplane was near touchdown. To overcome this problem, the radar operator monitored the antenna-tracking accuracy using a video camera which was mounted on and boresighted with the radar antenna. When the automatic elevation antenna track broke lock on the transponder antenna, the operator adjusted the antenna elevation slew rate in an attempt to keep the aircraft centered. This manual intervention introduced a potential source of error in the wind estimate. A sharp change in the postflight wind record, when the airplane was less than 60 m (200 ft) above the touchdown zone, could be a wind gust or it could be a slew rate adjustment of an elevation antenna.

The two biggest sources of error in the postflight wind estimation procedure appeared to be airspeed sensor noise and compass heading errors. The effects of angle of attack and sideslip angle errors could not be isolated from the airspeed sensor noise or for that matter, from radar-derived groundspeed errors. In the examples to follow, the airspeed error is assumed to have a magnitude of 2 knots and is depicted by a circle with a radius of 2 knots. The radar-derived groundspeed error is assumed to be 1 knot. The compass error is considered to be a bias ranging from 3° to 5°. The pilots attempted to align the compass just after the airplane began to track the runway centerline and this alignment accounts for much of the variation in heading from run to run.

Figures D2 and D3 show time histories of the wind magnitude and direction recorded from the wind mast located near the STOL port runway and determined postflight by

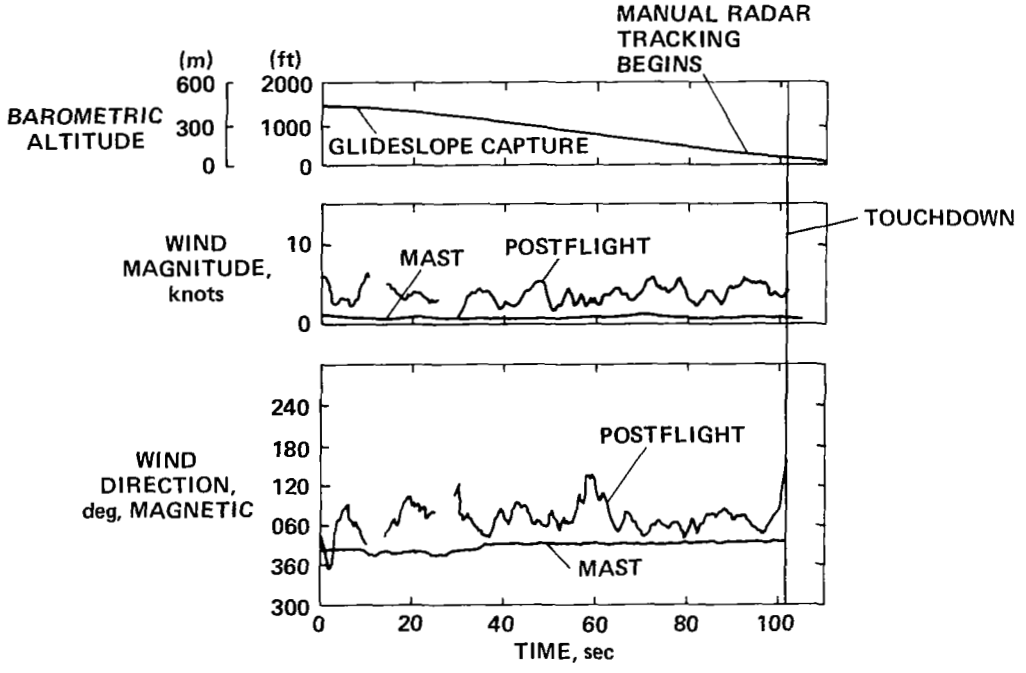

(a) Time history.

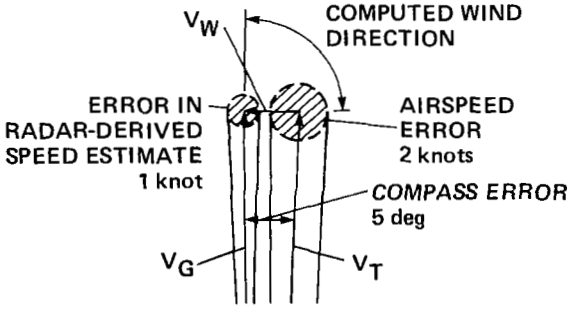

(b) Possible errors.

Figure D2.– Light wind.

forming the difference between the aircraft airspeed and radar groundspeed vectors. The altitude trace was included in the figures to relate the wind determination to the location of the airplane. The two data sources were most directly comparable at the time when the airplane passed the mast; 3 sec before touchdown in a calm-wind situation and not more than 5 sec before touchdown in a strong-wind situation.

Figure D2(a) shows the wind record for a light wind situation. The lower line is the output of the mast averaging filter. The upper line is the postflight wind estimate derived from aircraft sensor and radar data. The two wind-data sources show a discrepancy of 2 to 5 knots in magnitude and 20° to 50° in direction as the airplane passed the mast. The wind-vector diagram in figure D2(b) indicates that the disagreement between the records is probably caused by the compass and the airspeed errors influencing the postflight calculation of winds. The compass error was estimated from runway rollout data to be 3°. The wind vector, which is the difference between the airspeed and groundspeed vectors, could originate anywhere in the 2-knot-airspeed error circle and terminate any place in the 1-knot-groundspeed error circle. The postflight wind magnitude of 5 knots and the wind direction near 60° are probably mostly the result of the 3° compass error. The variations in wind direction and magnitude may represent higher-frequency turbulence or wind-measurement errors. Only more precise airspeed and heading measurements could separate high-frequency turbulence from measurement errors.

Figure D3(a) shows a time history of a strong and gusty wind from the northwest. Both the mast and the postflight data source show that the wind direction was 310° ±10°. The mast-derived wind magnitude was 20 knots ±10 knots. The

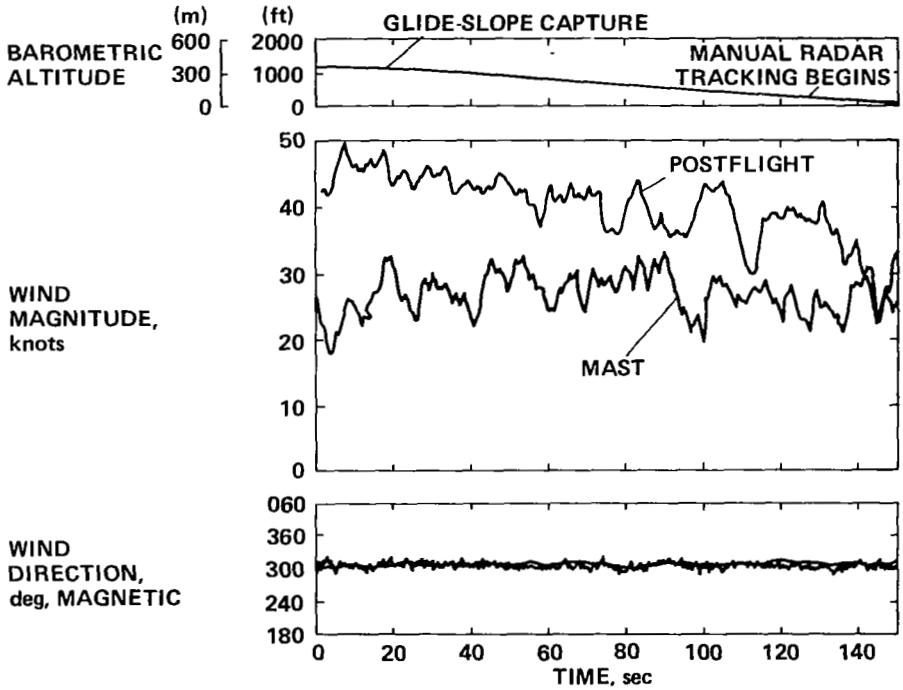

(a) Time history.

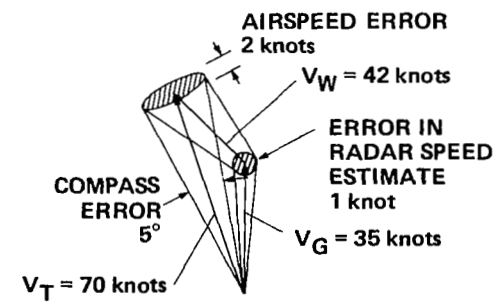

(b) Possible errors.

Figure D3.– Strong and gusting wind from the northwest.

postflight wind record shows a wind magnitude near 45 knots when the airplane was at an altitude of 300 m (1000 ft) decreasing to 25 knots at touchdown. The wind-vector diagram in figure D3(b) represents the situation 50 sec after the record began. Runway-rollout data indicate that the compass error was 5° during this approach. At 50 sec, the groundspeed was 35 knots and the airspeed was 70 knots. The calculated wind speed was 42 knots from 310° magnetic. The 2-knot airspeed-error circle, the 1-knot radar-derived, groundspeed error circle, and the 5° compass error are indicated. An examination of the resulting wind triangle shows that the wind-speed magnitude was probably accurate within 3 knots and was nearly independent of the compass error. The 5° compass error translated into a possible error in wind direction of 15°. The 3- to 5-knot variation in the postflight wind-magnitude record may be either high-frequency turbulence or measurement error but the 10- to 15-knot wind-speed variations probably represent actual wind gusts.

Figure D4 is a summary of the mast-measured wind conditions that were encountered during the AWJSRA autoland flight-test program. The wind direction in this figure was

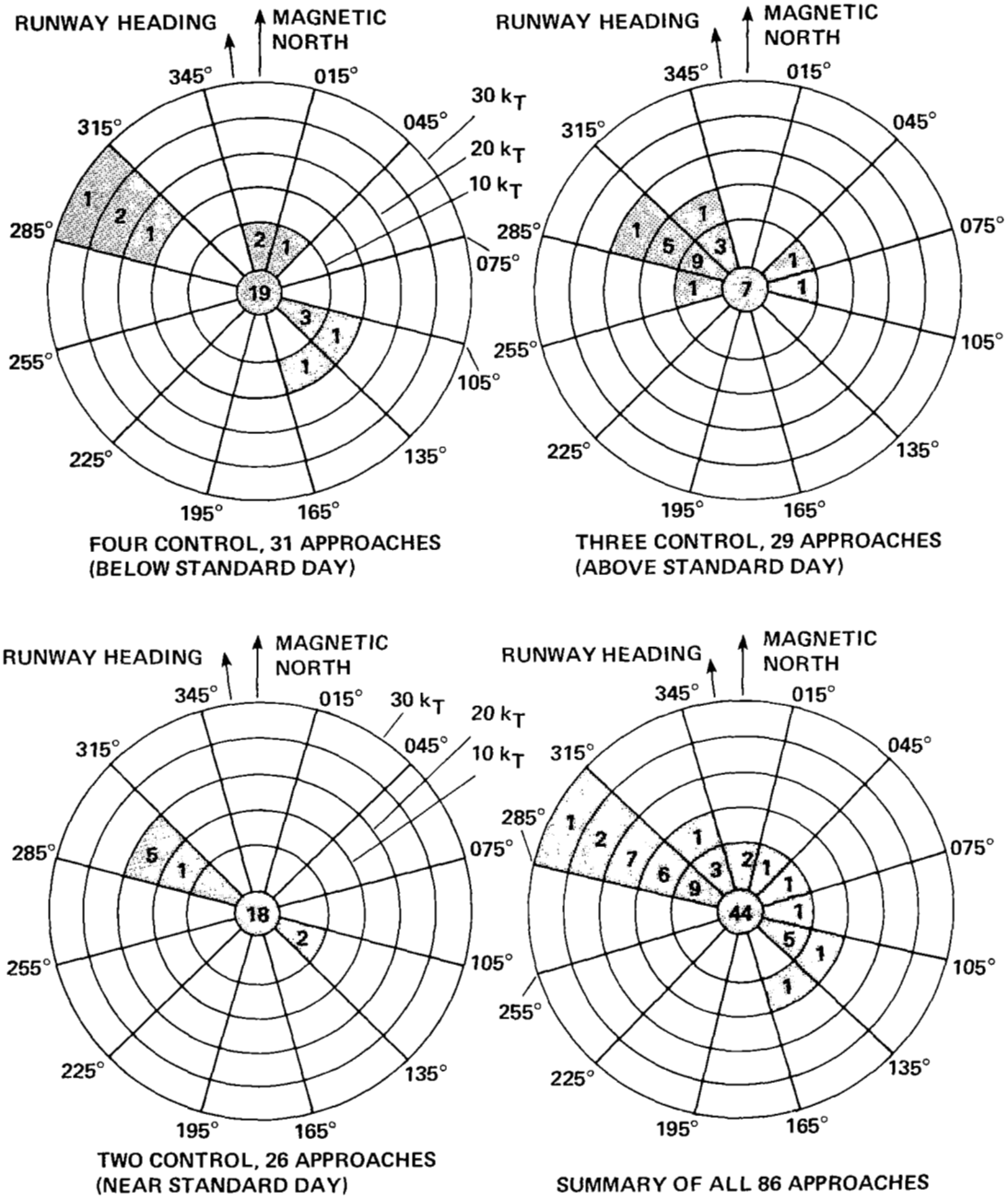

Figure D4.– Summary of mast-measured wind magnitude and direction at NALF Crows Landing during AWJSRA autoland flight-test approaches.

segregated into 30° increments. The wind magnitude was segregated into 5-knot speed intervals except for the 3-knot contour which outlines the calm condition. The numbers in the shaded areas represent the number of encounters with a specific wind magnitude and direction. In the majority of the approaches, the wind was calm as the airplane touched down. The four-control system encountered surface headwind components of 20 knots, crosswind components of 25 knots, and tailwind components of 12 knots. In AC 20-57A (ref. 22), the FAA requires a manufacturer to conduct simulation evaluations of an autoland system for CTOL transports in 25-knot headwinds, 15-knot crosswinds, and 10-knot tailwinds. The AWJSRA four-control autoland system operated successfully in wind conditions equivalent to the FAA requirement. The winds encountered with the three- and two-control systems were not as severe as those encountered with the four-control system but there were wind conditions adequate to demonstrate that the systems would probably perform adequately in windy conditions.

Some proposals on the operation of STOL airplanes into elevated STOL ports have suggested that it is not necessary to expect system operation in a tailwind because a tailwind places a severe penalty on the required landing and stopping distance. The experience gained in this program suggests that this may be an unreasonable assumption, particularly for a STOL port which has a precision approach available for only one runway direction, as was the case at the Crows Landing STOL port. Tailwind conditions exceeding 10 knots were encountered during one of the AWJSRA flights. During this particular flight, there was a high ceiling and light rain shower conditions. Typically, circuits from takeoff to landing were completed in 6 min with the last 2 min devoted to the precision approach and landing. The winds were calm when the airplane took off. By the time the airplane was in position for the first glide-slope capture, the wind had picked up to 130° at 12 knots. The wind was 150° at 12 knots during the second approach and from 130° at 7 knots on the third approach. All subsequent approaches were flown in calm conditions. This example shows that tailwinds can develop during the time needed to fly an approach. To avoid unacceptable operational procedures, an autoland system for a powered-lift STOL airplane must be capable of dealing with some level of tailwind and the existing 10-knot requirement for certification of CTOL transport autoland systems is reasonable.

APPENDIX E

STATISTICAL SUMMARIES OF GLIDE-SLOPE TRACK FLIGHT DATA

This appendix presents the flight-test glide-slope track performance for every approach of each of the control system variants tested that ended in an automatic landing. The mean and standard deviation of wind disturbances, error parameters, control activity, and acceleration components were computed as the airplane descended from 152 m (500 ft) to the flare-initiation height, 20 m (65 ft). These data provide specific information on how the three AWJSRA autoland systems performed in a variety of wind conditions.

Winds

Figure E1 is a summary of the wind magnitudes measured for each approach. The mean and standard deviations of the

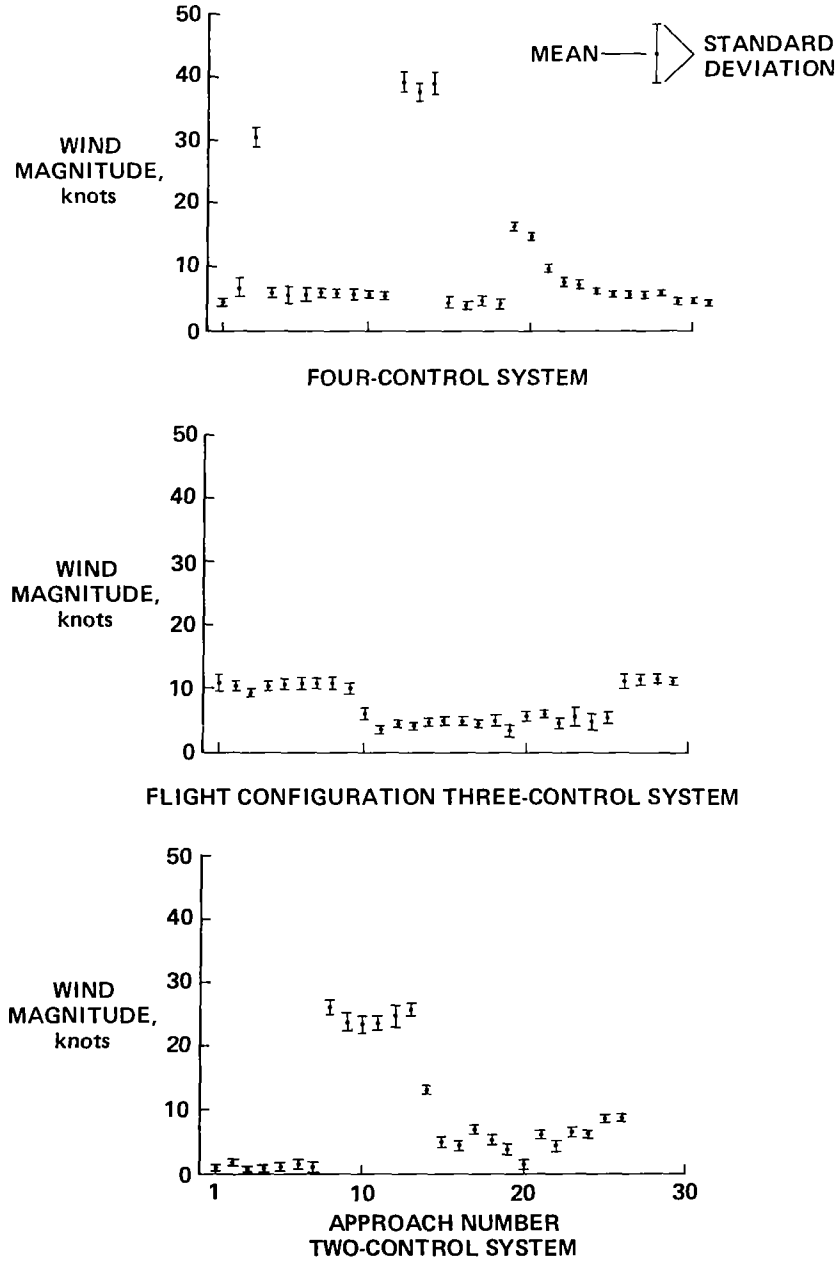

Figure E1.– Postflight-derived wind magnitude during descent from 152 m (500 ft) to 20 m (65 ft).

wind magnitude were calculated as the airplane descended from 152 m (500 ft) to 20 m (65 ft). This figure is useful for relating performance and control activity to the disturbance level for any specific approach.

Glide-Slope Error

Figure E2 shows the glide-slope error data for each of the control systems evaluated. Figure E2 suggests that the four-control system was markedly superior to either the flight configuration three-control system or the two-control system. Data on these three systems obtained from the high-speed simulation reported in reference 16 and summarized in table 2 in this report, show the glide-slope track performance of all three systems to be equivalent. Therefore, the difference in performance seen in figure E2 is apparently caused by the difference in the wind disturbances encountered in flight rather than by differences in control- system design.

The data from the flight configuration three-control system were accumulated during the late summer when temperatures were generally well above standard day and

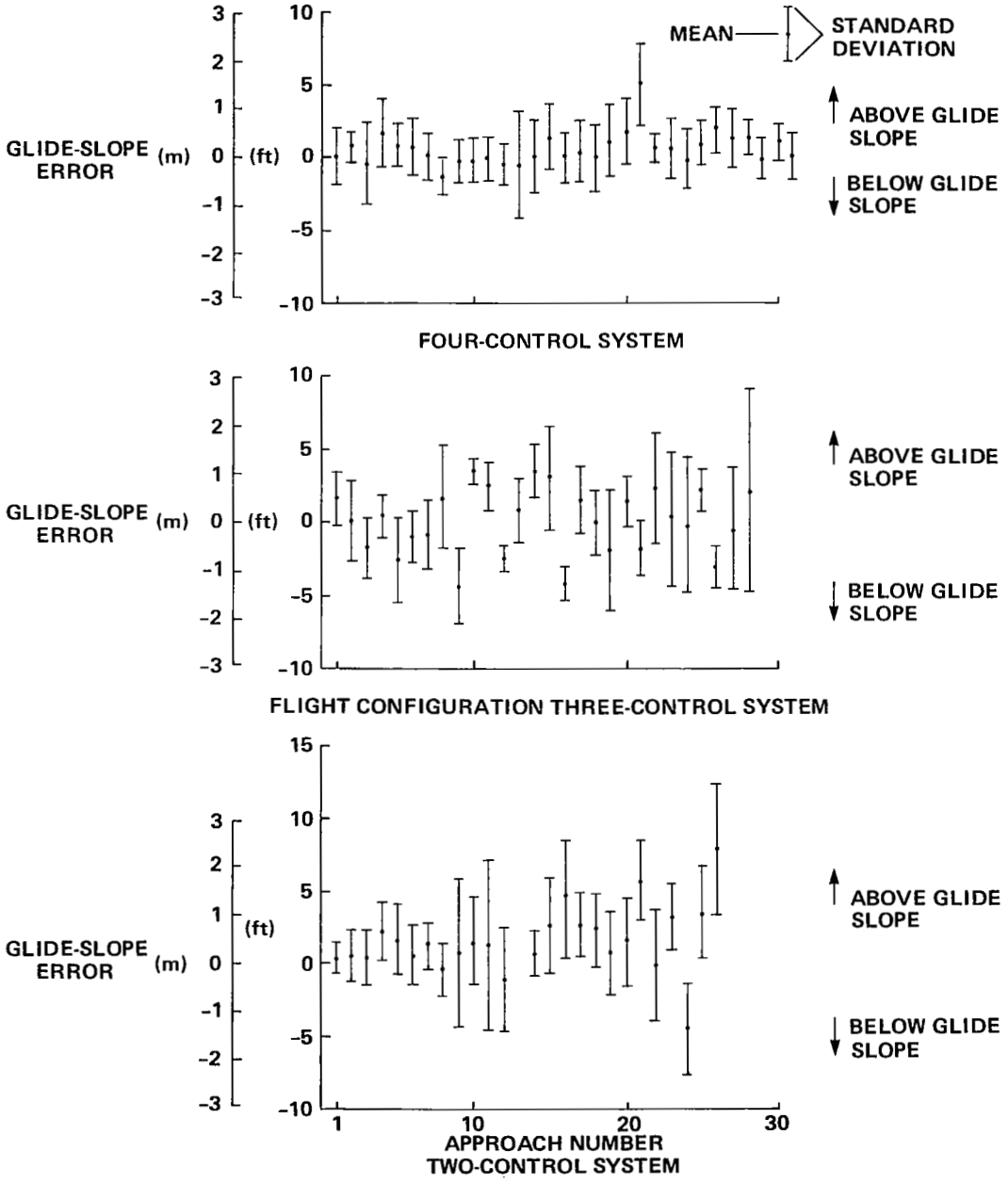

Figure E2.— Glide-slope track performance from 152 m (500 ft) to 20 m (65 ft).

thermal turbulence was present along with light winds. The data from the four-control and two-control systems were accumulated in winter conditions with near-standard day temperatures and either strong or very calm winds. The randomness that appears in the data of the two-control system is clearly the result of wind disturbances. In particular, the randomness seen in the glide-slope error data for the last six approaches was the result of the airplane being stabilized late in the approach as it descended into a temperature inversion. Wind magnitudes at altitudes above 152 m (500 ft) were between 15 and 20 knots but dropped to calm just before the flare maneuver was initiated. An example of the winds recorded on that flight was presented in figure 25(a) in this report.

The glide-slope performance of all three systems can be regarded as satisfactory from the point of view of meeting a requirement like the FAA glide-slope track requirement, ±35 μA or ±3.7 m (12 ft), for a CTOL transport operating on an ILS.

RPM and Choke Activity

Figure E3 summarizes the rpm activity as the airplane tracked the glide-slope. The mean value of the rpm varied

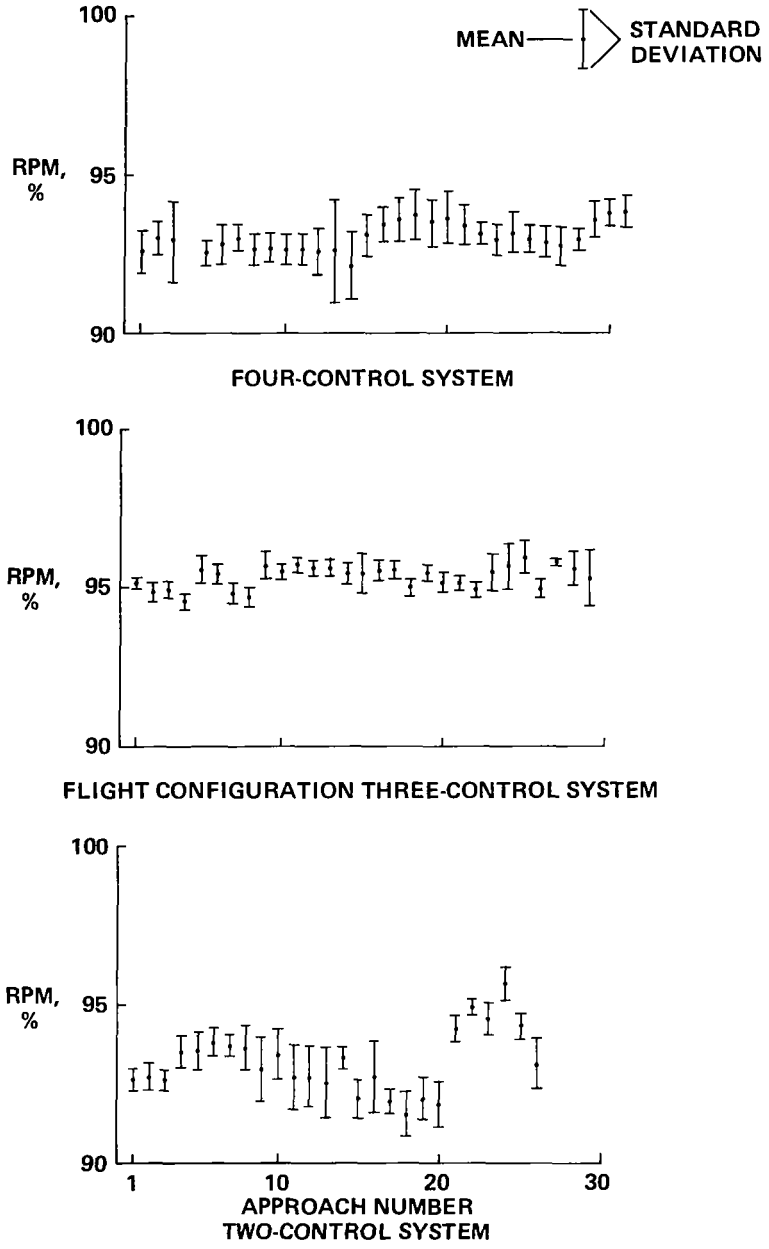

Figure E3.– RPM activity during glide-slope track from 152 m (500 ft) to 20 m (65 ft).

because of aircraft weight and the particular trim value of the nozzle. The significant part of this figure is the variation in the standard deviation from approach to approach. The larger values of standard deviation generally correlate to the stronger wind conditions shown in figure E1. The standard deviation was considerably smaller for the flight configuration three-control system than for either the four- or the two-control system. This reduced standard deviation indicates that the rpm was essentially inactive for the flight configuration three-control-system approaches.

Figure E4 shows the choke activity for the four-control and flight configuration three-control systems. The two-control system did not use the chokes. Figures E3 and E4 show that both rpm and chokes were actively operating to reduce path errors for the four-control system. These figures also show that for the flight configuration three-control system the major burden-of-path control was assumed by the chokes rather than rpm. The four-control system exhibits much more reserve capability in the chokes to counter large disturbances than does the flight configuration three-control system. Note that the glide-slope errors of the four-control system in figure E2 for approaches 3, 12, 13, and 14, where winds were strong, were essentially the same as when the winds were light. The standard deviations of the choke activity for the flight configuration three-control system were considerably higher than for the four-control system. This is attributable to the generally higher thermal-turbulence level encountered by the three-control system and to the total reliance on chokes for path control.

Airspeed

Figure E5 shows the airspeed error during the approaches. The four-control system produced good tracking performance in terms of the mean and the standard deviations. A comparison of wind data in figure E1 with airspeed error data in figure E5 clearly shows the correlation between strong winds and the larger associated speed error standard deviation.

Airspeed performance was somewhat degraded with the two-control system as compared with either the four-control or flight configuration three-control systems. The difference was more likely caused by the wind disturbances than by design differences in the control system.

Nozzle, Pitch Attitude, and Elevator

Because the mean value of the nozzle data was unreliable due to calibration problems in the data system, the nozzle data are not shown. Standard deviations for the four-control system ranged from 3° for light winds to 20° for strong winds and were 0° for the three- and two-control systems. The nonzero standard deviation for the four-control system was caused by the use of nozzles for speed control.

Figure E6 shows the pitch activity during the approaches and figure E7 shows the associated elevator activity. The standard deviation of the pitch attitude did not exceed 1° for either the four-control system or the flight configuration

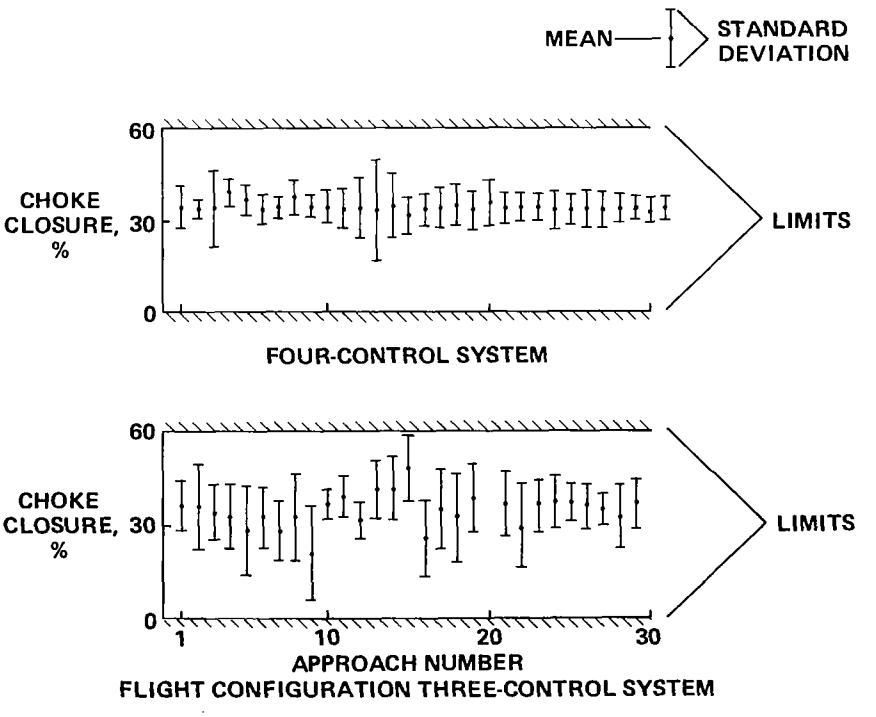

Figure E4.– Choke activity during glide-slope track from 152 m (500 ft) to 20 m (65 ft).

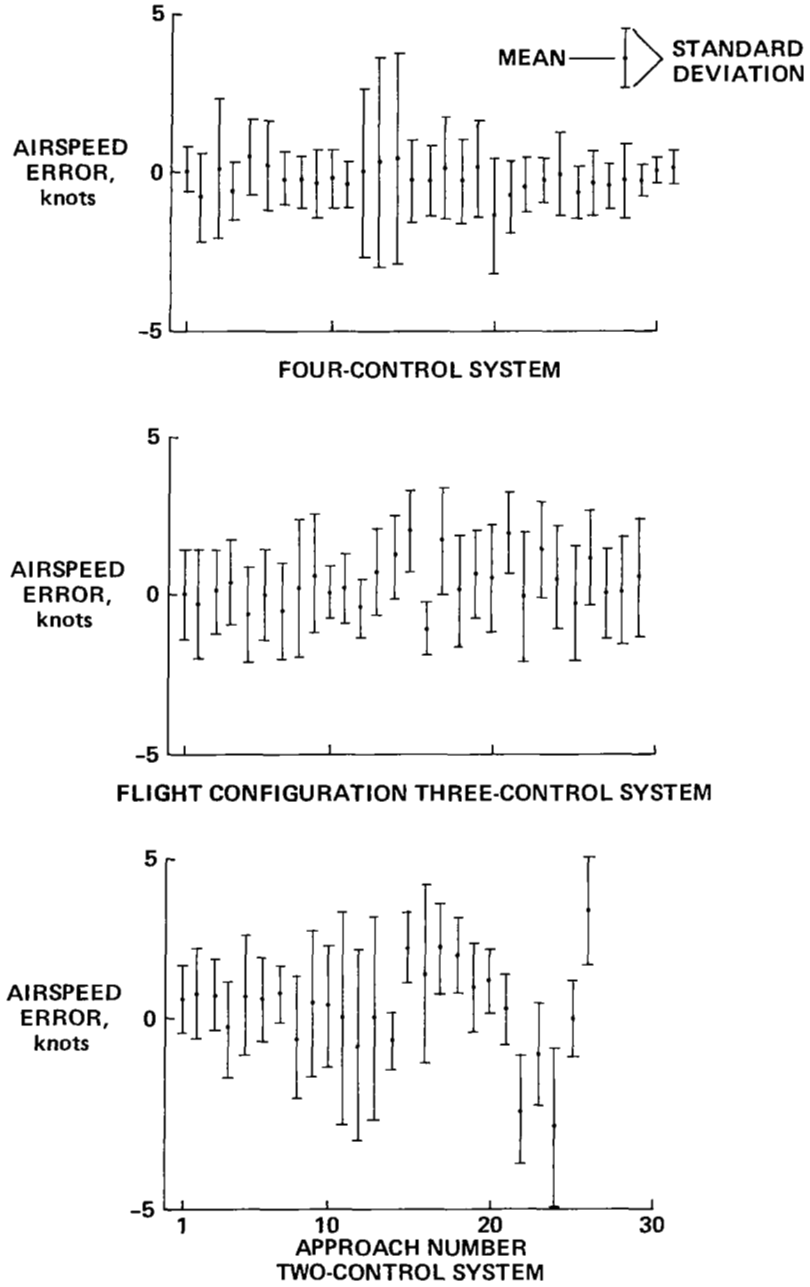

Figure E5.– Airspeed errors during glide-slope track from 152 m (500 ft) to 20 m (65 ft).

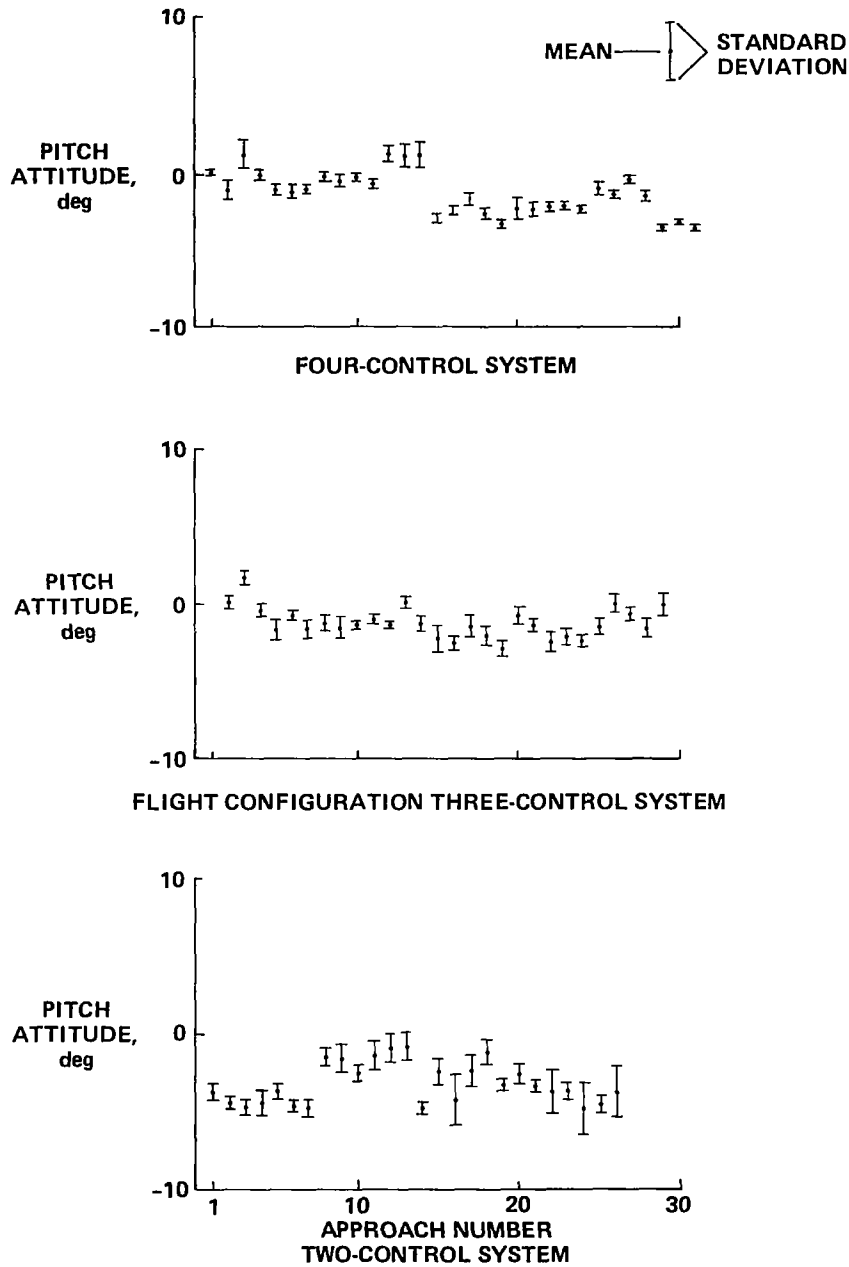

Figure E6.– Pitch activity during glide-slope track from 152 m (500 ft) to 20 m (65 ft).

three-control system. Higher pitch activity was evident for the two-control system but the standard deviation did not exceed 2°. The elevator activity shown in figure E7 was approximately the same for all of the control systems.

Longitudinal and Normal Acceleration

The longitudinal-acceleration data recorded during glide-slope tracking are shown in figure E8. Three factors affecting the longitudinal acceleration are apparent in this figure. First, the longitudinal-acceleration indications vary as the sine of the attitude angle. A comparison of longitudinal acceleration data in figure E8 with pitch attitude data in figure E6, indicates that the mean value of longitudinal acceleration was primarily related to the mean value of the pitch attitude data. The second factor influencing the longitudinal acceleration was the turbulence, which is assumed to be related to the wind magnitude shown in figure E1. The most prominent examples of the influence of winds on longitudinal acceleration are provided by approaches 3, 12, 13, and 14 flown with

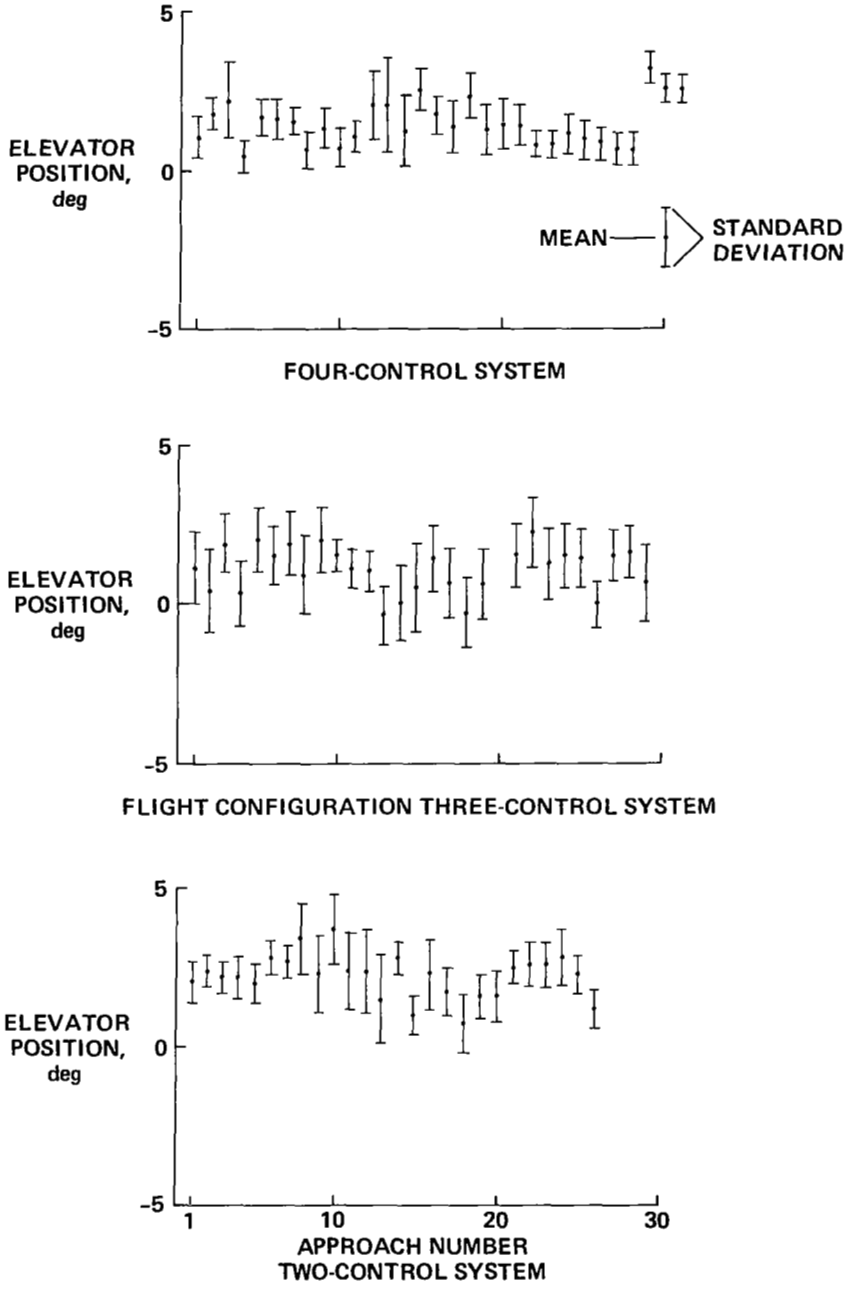

Figure E7.– Elevator activity during glide-slope track from 152 m (500 ft) to 20 m (65 ft).

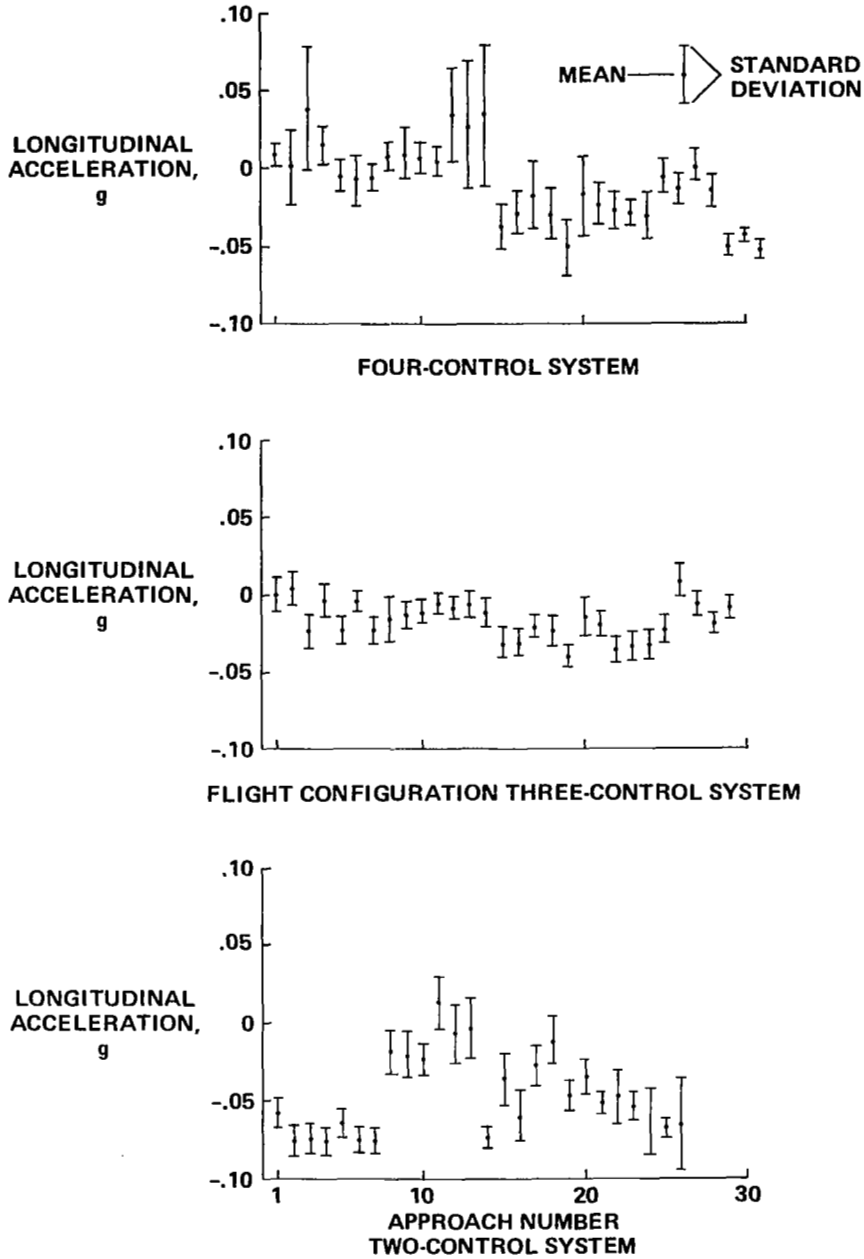

Figure E8.– Longitudinal acceleration during glide-slope track from 152 m (500 ft) to 20 m (65 ft).

the four-control system. Figure E1 shows that on those approaches, the recorded wind magnitude was more than 18 knots. Figure E8 shows that on those same approaches, the standard deviation of the longitudinal acceleration was on the order of 0.4 g. The third factor influencing the longitudinal acceleration was the design of the control system. Specifically, the four-control system used nozzles for speed control. As indicated in the wind model summary (fig. 21) in this report, 30% of the four-control-system approaches were flown in winds recorded by the wind mast as greater than 3 knots. On the other hand, 60% of the flight configuration three-control-system approaches were flown in winds greater than 3 knots. On the basis of wind magnitude alone, the standard deviation of the longitudinal acceleration associated with the flight configuration three-control system should have been greater than the standard deviation experienced with the four-control system. Figure E8 shows that the actual trend was just the opposite. This difference is probably attributable to the increased nozzle activity produced by the four-control system. This evaluation is in

agreement with the pilot comments that the nozzle activity could definitely be sensed when the four-control system was in operation.

Figure E9 shows the mean and standard deviations of the normal-acceleration signal recorded during glide-slope track from 152 m (500 ft) to 20 m (65 ft). Since the airplane was stabilized on the glide slope prior to flare initiation, the mean value of the normal acceleration should have been zero. Figure E9 shows that an accelerometer bias was present for all of the approaches. This bias was approximately the same for the four- and two-control systems. These data were recorded over the calendar period from November 1979 through February 1980. The flight configuration three-control-system data were recorded earlier during July and August of 1979. One of the flight configuration three-control-system approaches, approach 20, was initiated from a low altitude near 244 m (800 ft) above the touchdown zone. The airplane was not completely stabilized on the glide slope until just before flare entry and this lack of stabilization shows up in the normal acceleration summary as a shift in the mean.

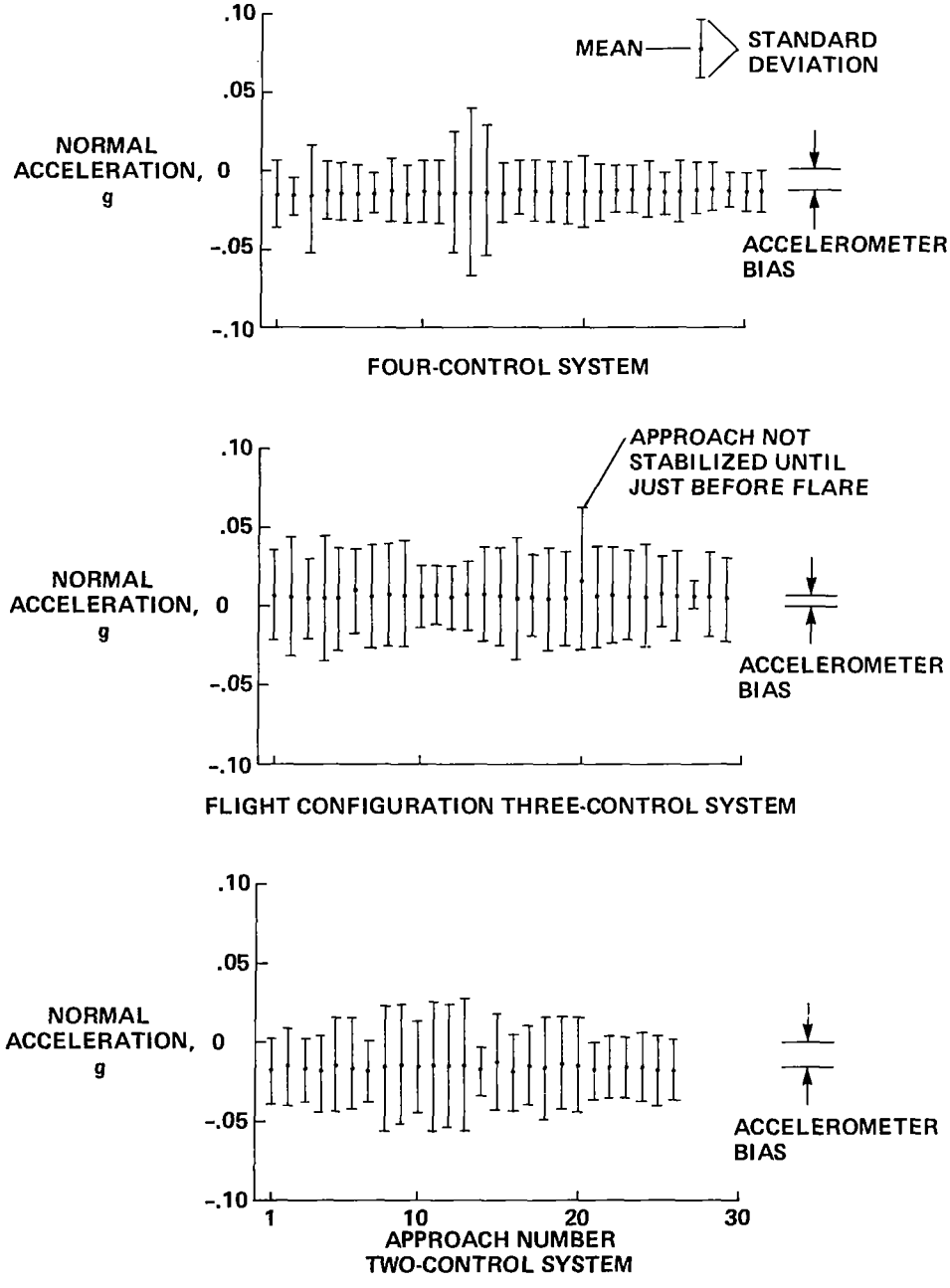

Figure E9.– Normal acceleration during glide-slope track from 152 m (500 ft) to 20 m (65 ft).

Both the four-control and flight configuration three-control systems provided excellent glide-slope track stabilization as evidenced by the essentially constant values of the normal acceleration bias. The two-control system provided less precise glide-slope tracking as evidenced by some variation in the mean value. The standard deviation of the normal acceleration was affected by the winds and the precision of the control system. The four approaches flown with the four-control system in strong winds, approaches 3, 12, 13, and 14, are associated with the large values of standard deviation between 0.04 and 0.05 g. The remainder of the four-control system approaches exhibited values near 0.02 g. Standard deviation values between 0.03 and 0.04 g reflect the light to moderate turbulence present for the flight configuration three-control-system approaches. The standard deviation values of normal acceleration for the two-control system between 0.02 and 0.04 g reflect the looser glide-slope track performance because these approaches were flown in the same generally light wind conditions encountered by the four-control system.

Research into the effects of acceleration on ride comfort of passengers was reported in reference 35. This reference provides a boundary of acceptable passenger ride in terms of a combination of normal and lateral acceleration. Figure E9 shows that the standard deviations of the normal acceleration were <0.05 g. The standard deviations of the lateral acceleration were generally <0.03 g. These acceleration levels fall well within the region associated with acceptable passenger ride as defined in reference 35.

REFERENCES

1. Ransone, R. K.; Lowe, W. S.; Kolk, F. W.; and Marks, M. D.: Inter-Metropolitan STOL Evaluation Plan, American Airlines Development Engineering Report No. 48/McDonnell Douglas Report G995, March 10, 1969.
2. American Airlines: Inter-Metropolitan STOL Evaluation (Phase 10), Final Report, American Airlines Development Engineering Report No. 50, January 1970.
3. Federal Aviation Administration: Planning and Design Criterion for Metropolitan STOL Ports. FAA, AC 150/5300-8, November 1970.
4. Federal Aviation Administration: Tentative Airworthiness Standards for Verticraft/Powered Lift Transport Category Aircraft. Flight Standards Service, Department of Transportation, Part XX, July 1968.
5. Scott, Barry C.; Hynes, Charles S.; Martin, Paul W.; and Bryder, Ralph B.: Progress Towards Development of Civil Airworthiness Criteria for Powered-Lift Aircraft. NASA TM X-73124, 1976.
6. Spangler, Roman M., Jr.: Simulated Ground-Level STOL Runway/Aircraft Evaluation. FAA-RD-73-110, Federal Aviation Administration, September 1973.
7. Rosewarne, H. P.; and Spruston, D. D.: The Canadian STOL Demonstration – The Data Collection, the Findings and Their Applications. ICAS Paper 76-53, October 1976.
8. Anon.: Simultaneous Instrument Approach Plan Readied, Aviation Week and Space Technology, vol. 116, no. 23, June 7, 1982, p. 31.
9. Stevens, V. C.; Riddle, D. W.; Martin, J. L.; and Innis, R. C.: Powered-Lift STOL Aircraft Shipboard Operations; A Comparison of Simulation, Land-Based and Sea Trial Results for the QSRA. AIAA Paper 81-2480, Las Vegas, Nev., November 11–13, 1981.
10. Grgurich, J.; and Bradbury, P.: STOLAND Final Report, NASA CR-137972, 1976.
11. Hindson, W. S.; Hardy, G. H.; and Innis, R. C.: Flight-Test Evaluation of STOL Control and Flight Director Concepts in a Powered-Lift Aircraft Flying Curved Decelerating Approaches. NASA TP 1641, 1981.
12. Cicolani, Luigi S.; Sridhar, B.; and Meyer, George: Configuration Management and Automatic Control of an Augmentor Wing Aircraft With Vectored Thrust. NASA TP 1222, 1979.
13. Neuman, F.; and Hardy, G. H.: Flight Investigation of a Four-Dimensional Terminal Area Guidance System for STOL Aircraft. NASA TM 81271, 1981.
14. Erzberger, Heinz; and McLean, John D.: Fuel-Conservative Guidance System for Powered-Lift Aircraft. NASA TM 78595, 1979, and AIAA Guidance and Control Conference Paper 79-1709, Boulder, Colorado, August 6–8, 1979.
15. Gevaert, G.; and Feinreich, B: The Development of Advanced Automatic Flare and Decrab Control Laws for Powered Lift Short Haul Aircraft Using a Microwave Landing System. NASA CR-151948, 1977.
16. Feinreich, B.; and Gevaert, G.: Development and Evaluation of Automatic Landing Control Laws for Powered Lift STOL Aircraft. NASA CR-152399, 1981.
17. Shah, N. M.; Gevaert, G.; and Lykken, L. O.: The Effect of Aircraft Environment on Category III Autoland Performance and Safety. AIAA Paper 72-811, Danvers, Mass., 1972.
18. Mineck, D. W.; Derr, R. E.; Lykken, L. O.; and Hall, J. C.: Avionic Flight Control System for the Lockheed L-1011 TriStar. Prepared for the SAE Aerospace Control and Guidance Systems Committee Meeting No. 30, San Diego, Calif., Sept. 27–29, 1972.
19. Lambergts, A. A.; and Creedon, J. F.: Development and Flight Evaluation of Automatic Flare Laws with Improved Touchdown Dispersion. Paper 80-1757, AIAA Guidance and Control Conference, Danvers, Mass., August 11–13, 1980.
20. Franklin, J. A.; and Innis, R. C.: Flight-Path and Airspeed Control During Landing Approach for Powered-Lift Aircraft. NASA TN D-7791, 1974.
21. Franklin, J. A.; Innis, R. C.; Hardy, G. H.; and Stephenson, J. D.: Design Criteria for Flightpath and Airspeed Control for the Approach and Landing of STOL Aircraft. NASA TP 1911, 1982.
22. Anon.: Automatic Landing Systems (ALS). FAA Advisory Circular, AC 20-57A, Federal Aviation Administration, 12 Jan. 1971.
23. Anon.: Criteria for Approval of Category IIIa Landing Weather Minima. FAA AC 120-28B, Federal Aviation Administration, Dec. 1, 1977.
24. Ashleman, R. H.; and Skavdahl, H.: The Development of an Augmentor Wing Jet STOL Research Airplane (Modified C-8A), Volume I – Summary. NASA CR-114503, 1972.
25. Warner, D. N.; and Moran, F. J.: Flight-Test Evaluation Errors in the Modils and TACAN Navigation Aids at NALF Crows Landing. NASA TM 78584, 1979.
26. Anon.: Airman's Information Manual – Basic Flight Information and ATC Procedures. U.S. Department of Transportation, Federal Aviation Administration, January 21, 1982.

27. Anon.: Microwave Landing System (MLS) Signal Format and System Level Functional Requirements. Federal Aviation Administration, FAA-ER-700-08 Amendment 1, August 22, 1975.
28. Neuman, F.; and Warner, D. N., Jr.: A STOL Terminal Area Navigation System. NASA TM X-62348, 1974.
29. De Hoff, R. L.; Reed, W. B., and Trankle, T. L.: Identifition of Spey Engine Dynamics in the Augmentor Wing Jet STOL Research Aircraft from Flight Data. NASA CR-152054, 1977.
30. Cleveland, W. B.; Vomaske, R. F.; and Sinclair, S. R. M.: Augmentor Wing Jet STOL Research Aircraft Digital Simulation Model. NASA TM X-62,149, 1972.
31. Rumsey, P. C.; and Spitzer, R. E.: Simulator Model Specification for the Augmentor Wing Jet STOL Research Aircraft. NASA CR-114434, 1971.
32. Warner, D. N., Jr.: MLS Vertical Guidance and Navigation of a STOL Airplane Landing on an Elevated STOLport. NASA TM 81338, 1981.
33. Heffley, R. K.; Stapleford, R. L.; Rumold, R. C.; Lehman, J. M.; Scott, B. C.; and Hynes, C. S.: A STOL Airworthiness Investigation Using a Simulation of an Augmentor Wing Transport, Volume II – Simulation Data and Analysis, and NASA TM X-62,396, 1974.
34. Barr, N. M.; Gangaas, D.; and Schaeffer, D. R.: Wind Models for Flight Simulator Certification of Landing and Approach Guidance and Control Systems. FAA-RD-74-206, 1974.
35. Holloway, R. B.; and Brumaghim, S. H.: Tests and Analysis Applicable to Passenger Ride Quality of Large Transport Aircraft. Symposium on Vehicle Ride Quality, NASA TM X-2620, 1972, pp. 91-113.
36. Watson, D. M.; Hardy, G. H.; Moran, J. F.; and Warner, D. N., Jr.: A Method for Determining Landing Runway Length for a STOL Aircraft. NASA CP 2107, Part 1, 1980 Aircraft Safety and Operating Problems, November 5-7, 1980, pp. 127-144.
37. Hynes, C. S.; and Scott, B. C.: Tentative Civil Airworthiness Flight Criteria for Powered-Lift Transports. NASA SP-416, Aircraft Safety and Operating Problems Conference, October 18-20, 1976, pp. 165-178.

1. Report No.	2. Government Accession No.	3. Recipient's Catalog No.
NASA TP-2128		

4. Title and Subtitle	5. Report Date
FLIGHT-TEST OF THE GLIDE-SLOPE TRACK AND FLARE-CONTROL LAWS FOR AN AUTOMATIC LANDING SYSTEM FOR A POWERED-LIFT STOL AIRPLANE	December 1983
	6. Performing Organization Code
7. Author(s)	8. Performing Organization Report No.
DeLamar M. Watson, Gordon H. Hardy, and David N. Warner, Jr.	A-9199
	10. Work Unit No.
9. Performing Organization Name and Address	T-3848
NASA Ames Research Center Moffett Field, California	11. Contract or Grant No.
	13. Type of Report and Period Covered
12. Sponsoring Agency Name and Address	Technical Paper
National Aeronautics and Space Administration Washington, D.C. 20546	14. Sponsoring Agency Code 532-02-11

15. Supplementary Notes

Point of Contact: D. M. Watson, Ames Research Center, M/S 211-2, Moffett Field, CA 94035
(415) 965-5826 and FTS 448-5826.

16. Abstract

An automatic landing system was developed for the Augmentor Wing Jet STOL Research Airplane to establish the feasibility and examine the operating characteristics of a powered-lift STOL transport flying a steep, microwave-landing system (MLS) glide slope to automatically land on a STOL port. The flight test results in this report address the longitudinal aspects of automatic powered-lift STOL airplane operation including glide-slope tracking on the backside of the power curve, flare, and touchdown. Three different auto-land control laws were evaluated to demonstrate the tradeoff between control complexity and the resulting performance. The flight test and simulation methodology used in developing conventional jet-transport systems was applied to the powered-lift STOL airplane. The results obtained from this research program suggest that an automatic landing system for a powered-lift STOL airplane operating into an MLS-equipped STOL port is feasible. However, the airplane must be provided with a means of rapidly regulating lift to satisfactorily provide the glide-slope tracking and control of touchdown sink rate needed for automatic landings.

17. Key Words (Suggested by Author(s))	18. Distribution Statement
Automatic landing system Powered-lift STOL STOL Microwave landing system (MLS)	Unclassified - Unlimited Subject Category: 08

19. Security Classif. (of this report)	20. Security Classif. (of this page)	21. No. of Pages	22. Price*
Unclassified	Unclassified	89	A05

*For sale by the National Technical Information Service, Springfield, Virginia 22161

NASA-Langley, 1983

National Aeronautics and Space Administration

Washington, D.C.
20546

Official Business
Penalty for Private Use, $300

THIRD-CLASS BULK RATE

Postage and Fees Paid
National Aeronautics and Space Administration
NASA-451

U.S.MAIL

/ 1 1U,A, 831201 S00903DS
DEPT OF THE AIR FORCE
AF WEAPONS LABORATORY
ATTN: TECHNICAL LIBRARY (SUL)
KIRTLAND AFB NM 87117

S

NASA

POSTMASTER: If Undeliverable (Section 158 Postal Manual) Do Not Return